Bulletin of Romanian Chemical Engineering Society

1^{2015}

Bulletin of Romanian Chemical Engineering Society

Contents

NITROBENZENE HYDROGENATION BY CATALYSTS BASED ON RUTHENIUM

Dorin BOMBOS[1][*], Carmen ARGESANU[2], Rami DOUKEH[1], Mihaela BOMBOS[3], Gabriel VASILIEVICI[3]

[1] Petroleum-Gas University of Ploiesti, 39 Bucuresti street, 100680, Ploiesti, Romania
[2] National College "Nichita Stanescu", 3 Nalbei street, 100085, Ploiesti, Romania
[3] National Research Institute for Chemistry and Petrochemistry, ICECHIM, 202 Spl. Independentei, 060021, Bucharest, Romania

Abstract
Nitrobenzene hydrogenation process was developed by catalysts based on ruthenium, such as Ru/HZSM5 and Ru-Cu-Ni /activated carbon. Experiments were performed in a fixed bed reactor at 10-40 bar pressure range, 45-75 ^0C temperature range, 0.2-0.6 h^{-1} weight hourly space velocities of nitrobenzene and the molar ratio hydrogen/nitrobenzene of 10. The acid strength distribution of the catalysts was performed by thermodesorption of diethylamine. The activity of Ru-Cu-Ni /activated carbon catalyst was higher than for Ru/HZSM5 catalyst and the aniline selectivity is higher for Ru/HZSM5 catalyst. The nitrobenzene conversion increases with the increase of temperature and decreases with increasing of weight hourly space velocities. The variation of nitrobenzene conversion with the pressure, on studied pressure range, varies with a maximum for both catalysts studied.

Key words: catalysts, hydrogenation, activated carbon, nitrobenzene, acid strength, ruthenium

1. Introduction

Hydrogenation of nitrobenzene is achieved with the formation of various compounds such as aniline, N-fenilhidroxilamina, diphenylamine, diphenylhydrazine, azobenzene, nitrociclohexan. Aniline is an important industrial product used for the synthesis of dyes, pigments, plastics, pharmaceuticals, production of explosives, in agricultural products [1]. The production of this kind of substance has been approached by three different procedures:

(i) by stoichiometric reduction of the corresponding aromatic nitro compounds using iron, zinc or a metal sulfide such as Na_2S [1]. However, this

---

[*] Corresponding author; E-mail address: dbombos@upg-ploiesti.ro (Dorin Bombos)

method displays low selectivity for nitro group, and the major disadvantages are toxicity, odor of most reducing agents, sulfur containing organic side products and formation of elemental sulfur [2];

(ii) catalytic hydrogenation of nitro compounds by transfer hydrogenation processes [3, 4] or

(iii) using H_2 over supported noble metal catalysts.

Thus, the utilization of catalysts is an important tool for the hydrogenation process. The role of catalysis in the development of clean chemical production with limited hazardous and toxic by-products is now well-established as using catalytic reduction with molecular hydrogen, because it is a clean production process, high atom economy, cheap operations, easy product separation and can offer high selectivity to the desired product with a significantly lower environmental impact [5]. So, to obtain the aromatic amines various catalysts have been used [6-12]. The high exothermicity of the hydrogenation process of nitrobenzene in liquid phase, correlated with the effects of support acidity on catalytic performance hydrogenation of nitrobenzene, justified concerns for studying this process. Recently, a great deal attention has been attracted to design application of activated carbon catalysts because they often possess interesting physical properties like a large surface area, a suitable porosity and can be used at high temperature and pressure reaction conditions. Cu and Ni have been reported to be used widely in hydrogenation process of nitrobenzene and they are used in the preparation of catalysts because of their low price. Ru is favorable catalysts in industries because of its high activity. In order to compare the influence of the catalyst acidity, we have tested two different supports, activated carbon and a zeolite (HZSM5).

2. Experimental

The raw materials used in experiments were: nitrobenzene of analytical grade (Merck), n-heptane of analytical grade (Merck), copper (II) nitrate trihydrate puriss. p.a. (Sigma-Aldrich), nickel (II) nitrate hexahydrate puriss. p.a. (Sigma-Aldrich), ruthenium chloride trihydrate technical (Sigma-Aldrich), granular activated charcoal, (Merck), HZSM-5 zeolite, nickel (II) nitrate hexahydrate and electrolytic hydrogen purity from Linde Company.

Catalysts used, 1% Ru-5%Cu-8%Ni /activated carbon and 0.5%Ru /H-ZSM 5-γ Al_2O_3, where prepared by impregnation method. Thus, the deposition of Ru was performed by incipient wetness method with an aqueous solution of ruthenium chloride trihydrate and the deposition of Cu and Ni by the pore filling method with aqueous solution of nitrates. Chemical composition of the catalysts used in the experimental program was determined by atomic absorption spectroscopy. Acid strength distribution of catalysts was determined by

3

thermodesorption of diethylamine in the temperature range 20-700°C. Thermal analyzes were performed on a DuPont Instruments' Thermal Analyst 2000/2100" coupled with a module "951 Thermogravimetric Analizer".

The experimental program was performed in a continuous fixed bed catalytic reactor. The temperature was regulated with an automatic system coupled with two fixed thermocouples, placed in the reactor jacket. A metallic jacket for the mobile thermocouple was also placed in the axis of the reactor, the sheath in which was axially placed in the central zone of the catalyst bed, in order to measure the reaction temperature. The process was carried out in isothermal conditions.

Reaction conditions for catalysts were:
- pressure: 10 – 40 bar;
- temperature: 45 -75 ^{0}C;
- weight hourly space velocity of nitrobenzene: 0.2 – 0.6 h^{-1};
- molar ratio hydrogen/ nitrobenzene: 10/1.

Nitrobenzene was redistilled and diluted with heptane, the total content of nitrobenzene in the reaction mixture being 50% by volume. The composition of the reaction mixture was analyzed using a gas chromatograph equipped with capillary column with a length of 30 m and having a diameter of 0.250 mm, the fixed phase being polyethylene glycol (PEG).

3. Results and discussions

Fig. 1 shows the distribution of acidity center of 0.5%Ru /H-ZSM 5-γ Al$_2$O$_3$ catalyst (A - concentration of centers with weak acidity, B - concentration of centers with medium acidity, C - concentration of centers with high acidity). In Fig. 1 could be observed a higher content in weak acidic centers (0.34 meq./g) and medium strength (0.35 meq./g) and a lower concentration of strong acid centers over two times smaller than the weak acid centers (0.17 meq./g).
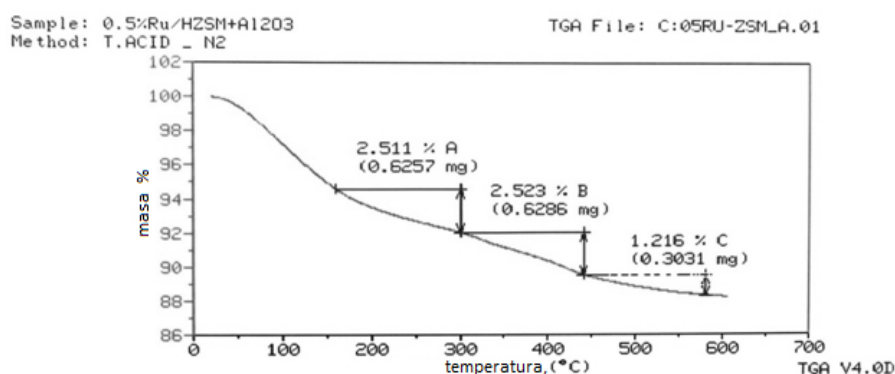
Fig. 1. Acid strength distribution of 0.5%Ru /H-ZSM 5-γ Al$_2$O$_3$ catalyst

Fig. 2 shows the distribution of acidity center of 1% Ru-5%Cu-8%Ni /activated carbon catalyst. It could be observed a higher content in weak acidic centers (1.0 meq./g) and a lower concentration of medium strength strong acid centers of two times smaller than the weak acid centers (0.51 meq./g respectively 0.53 meq./g).
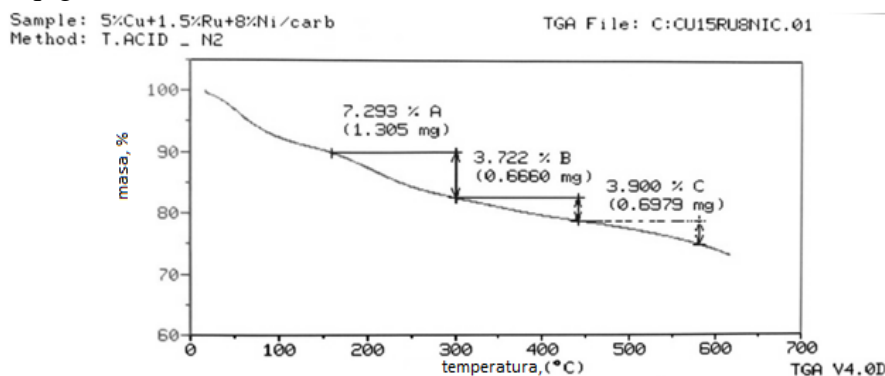
Fig. 2. Acid strength distribution of 1%Ru-5%Cu -8%Ni/granular activated charcoal catalyst

The major compound identified at nitrobenzene hydrogenation was aniline, other compounds being diphenylamine, diphenylhydrazine, azobenzene and nitrocyclohexane. The influence of weight hourly space velocities on the conversion of nitrobenzene is shown in Fig. 3. For both catalysts the conversion of nitrobenzene decreased with weight hourly space velocities. It could be observed that in the case of Ru /H-ZSM 5-γ Al$_2$O$_3$ catalyst were obtained greater conversions than in the case of Ru - Cu - Ni/charcoal activated catalyst, for the range of the weight hourly space velocities variation studied.
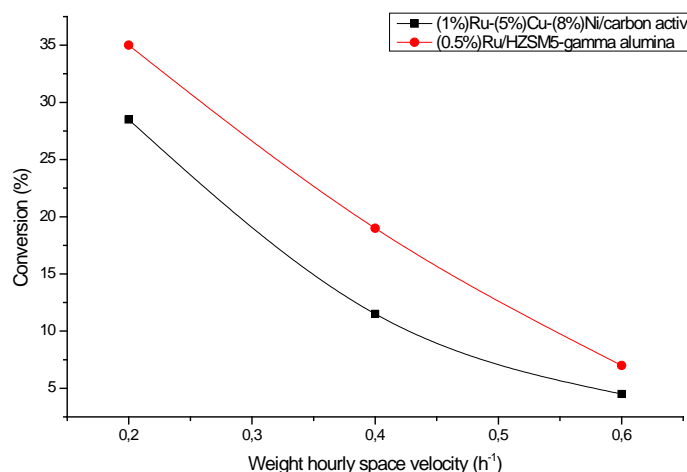
Fig. 3. Influence of weight hourly space velocities on the conversion of nitrobenzene at 25 atm. and 45 ^{0}C

The influence of weight hourly space velocities on the yield in total aromatic compounds and on the yield in aniline is shown in Figs. 4 and 5. Both total aromatic compounds yield and aniline yield have higher values for Ru / H-ZSM 5 catalyst. For the catalyst Ru / H-ZSM 5, the variation curves of total aromatic compounds yield and of aniline yield are similar to the variation curve of nitrobenzene conversion. Aniline yield variation with weight hourly space velocities arises with a maximum.
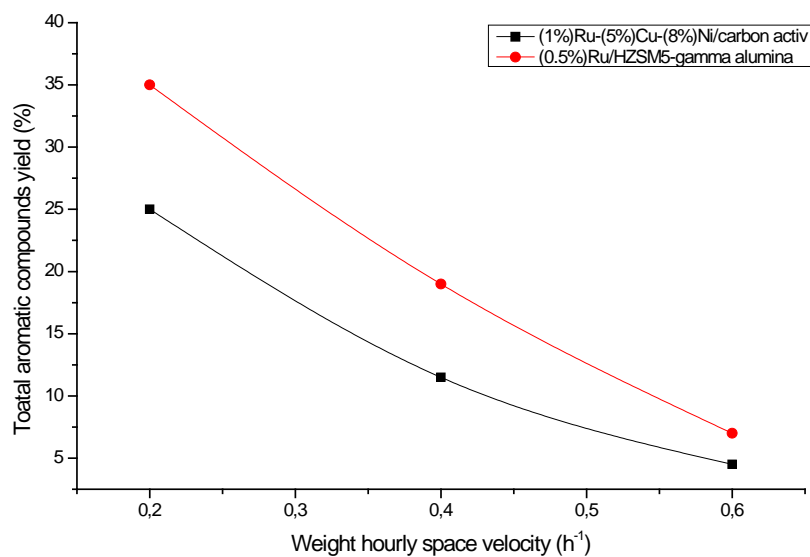
Fig. 4. Influence of weight hourly space velocities on the yield in total aromatic compounds at 25 atm. and 45 ^{0}C
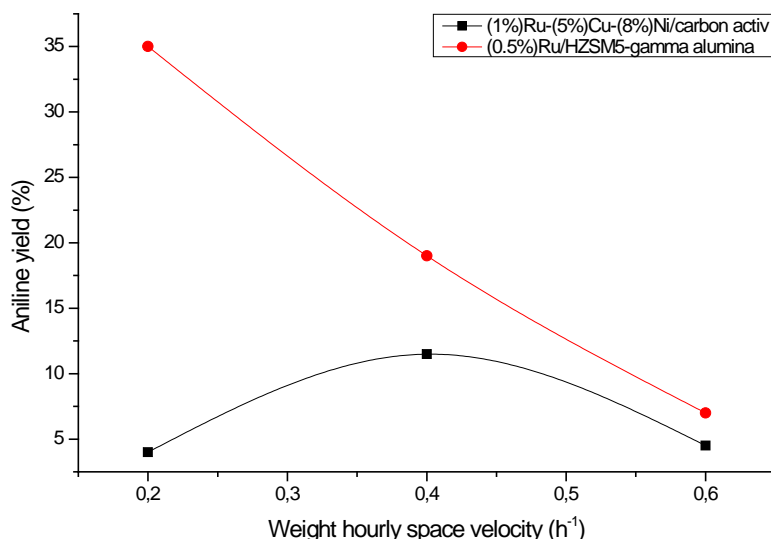
Fig. 5. Influence of weight hourly space velocities on the yield in aniline at 25 atm. and 45 ^{0}C

Variation of nitrobenzene conversion with temperature is shown in Fig. 6. Conversion of nitrobenzene is much higher for Ru-Cu-Ni/carbon catalyst towards Ru/HZSM5-γ Al$_2$O$_3$ catalyst. The nitrobenzene conversion increases with the increase of temperature for both catalysts, but conversion slope variation with temperature has a much higher value for Ru- Cu- Ni/carbon catalyst than for Ru/HZSM5 catalyst.
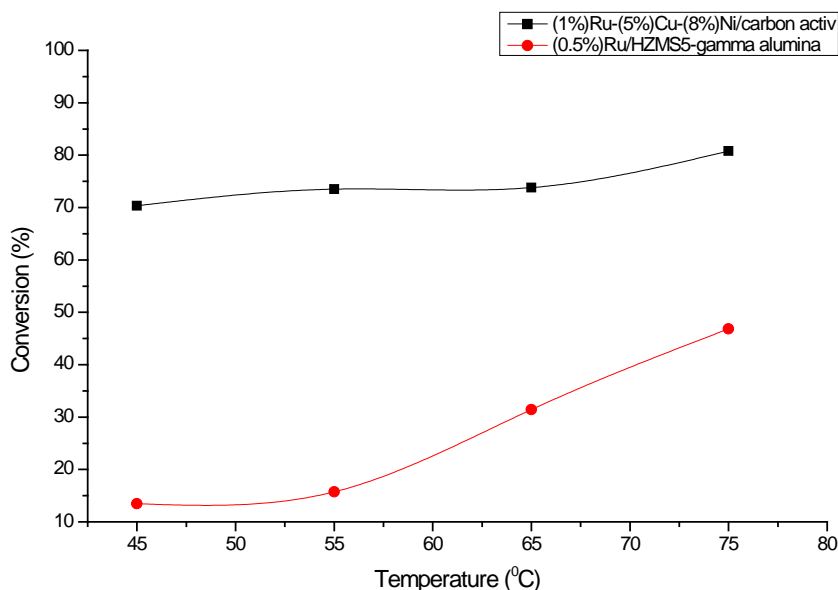
Fig.6. Variation of nitrobenzene conversion with temperature at 25 atm and 0.2 h^{-1} space velocity of nitrobenzene

The influence of temperature on the yield in total aromatic compounds and on the yield in aniline is shown in Figs. 7 and 8. Total aromatic compounds yield and aniline yield have lower values for Ru / H-ZSM 5 catalyst. For the both catalyst variation curves of total aromatic compounds yield and of aniline yield are similar to the variation curve of nitrobenzene conversion.

Variation of nitrobenzene conversion with pressure is shown in Fig. 9. Conversion of nitrobenzene for both catalysts has a variation with maximum, the slope of variation being higher in the case of Ru/HZSM5 catalyst. This behavior at high pressure is probably due to catalyst sintering generated by the increase of reaction speed, favored by the increasing of nitrobenzene fraction in liquid phase. For the both catalysts variation curves of total aromatic compounds yield and of aniline yield are similar to the variation curve of nitrobenzene conversion (Figs. 10 and 11).
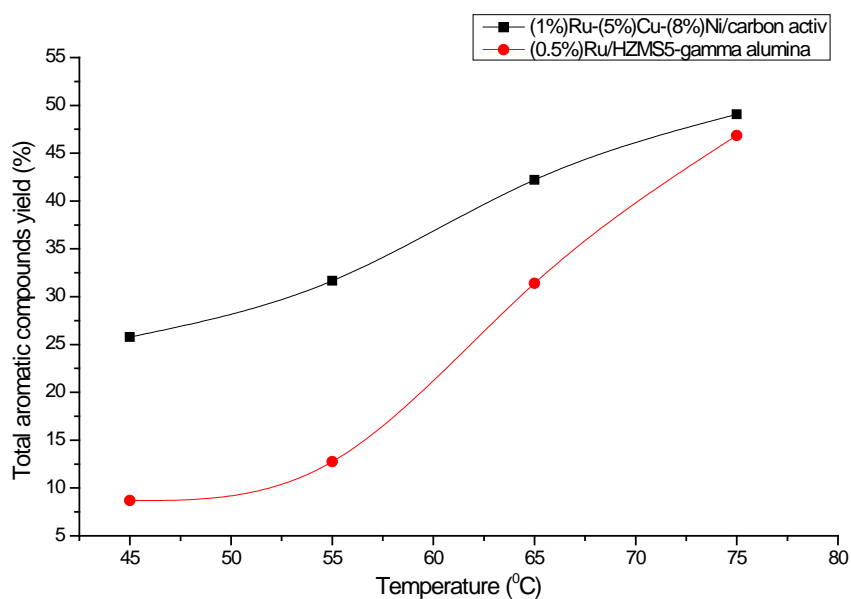
Fig. 7. Variation of yield in total aromatics derivatives with temperature
at 25 atm and 0.2 h^{-1} space velocity of nitrobenzene
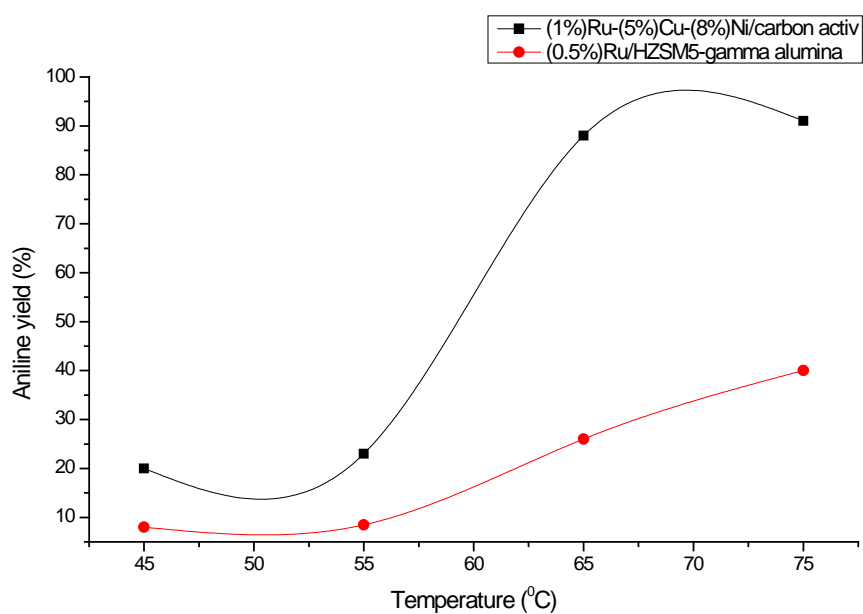
Fig. 8. Variation of yield in aniline with temperature
at 25 atm and 0.2 h^{-1} space velocity of nitrobenzene

8
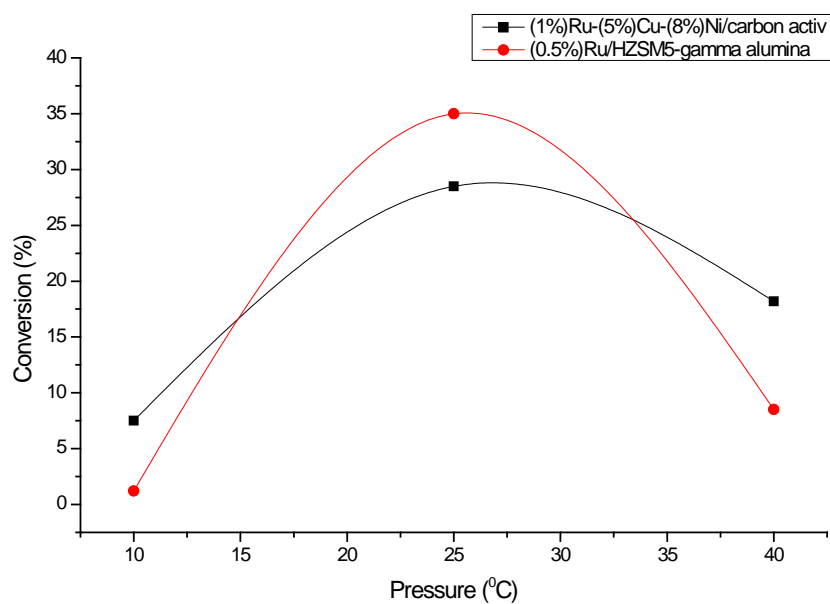
Fig.9. Variation of nitrobenzene conversion with pressure at 45°C and 0.2 h^{-1} space velocity of nitrobenzene
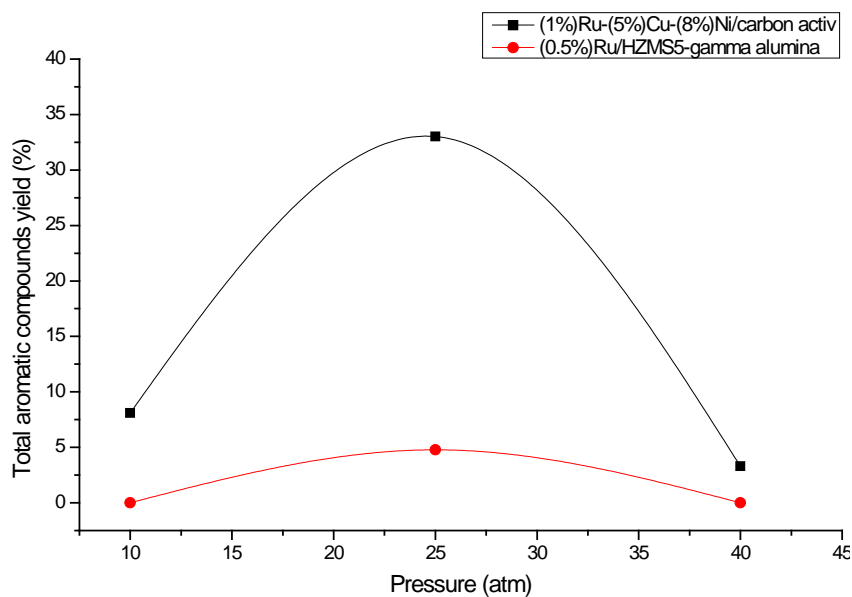
Fig. 10. Variation of yield in total aromatics derivatives with pressure at 45°C and 0.2 h^{-1} space velocity of nitrobenzene
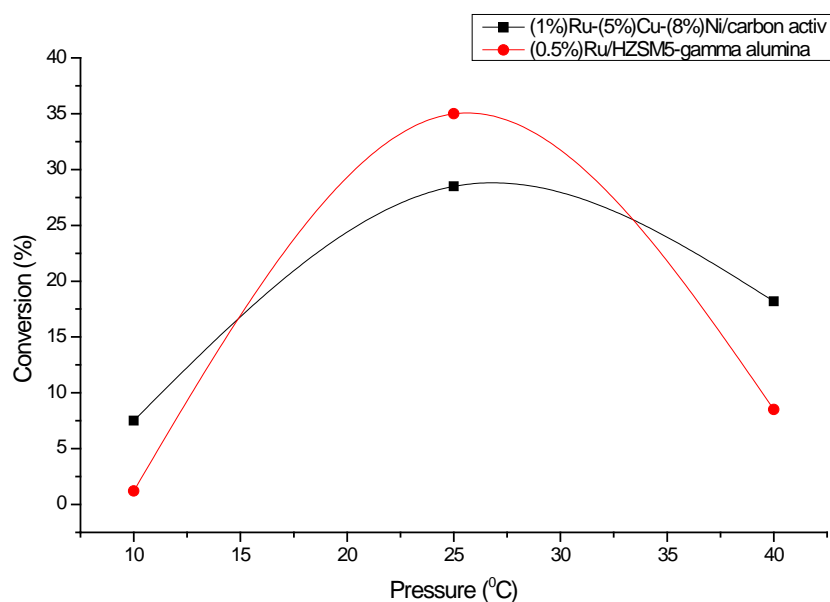
Fig. 11. Variation of yield in aniline with pressure
at 45°C and 0.2 h^{-1} space velocity of nitrobenzene

4. Conclusions

Study of the hydrogenation process of nitrobenzene on a monometallic catalyst (Ru / HZSM5) and one three-metallic Ru-Cu-Ni / granular activated carbon was performed. Distribution of strength acid pores of catalysts was determined by thermal desorption of diethylamine in the temperature range 20-700^{0}C.

Testing of the prepared catalyst was carried out in a single reactor tube with co-current, downward flow of reagent. For all catalysts tested the temperature rise favors the increasing of the nitrobenzene conversion and yield in total aromatic compounds and in aniline.

The best yield in total aromatic compounds and in aniline was obtained in the case of Ru-Cu-Ni / charcoal catalyst. Variation of nitrobenzene conversion and yield in aniline and in total aromatic compounds with pressure shows a maximum at 25 atm.

REFERENCES

[1] Camposa C., Torresa C., Oportusa M., Pe˜nab M.A., Fierrob J.L.G., Reyesa P., *Catalysis Today,* 213, (2013), 93– 100.
[2] Nomura K., *Journal of Molecular Catalysis A: Chemical,* 130, (1998), 1–28.
[3] Auer S.M., Grunwaldt J.-D., Köppel R.A., Baiker A., *Journal of Molecular Catalysis A: Chemical* 139, (1999), 305–313.

[4] Wilkinson H.S., Tanoury G.J., Wald S.A., Senanayake C.H., *Tetrahedron Letters,* 41, (2001), 167–170.

[5] Radl S., Koynov A., Tryggvason G., Khinast J.G., *Chemical Engineering Science,* 63, (2008), 3279–3291.

[6] Wang Sh., He B., Wang Y., Zhao X., *Catalysis Communications*, 24, (2012), 109–113.

[7] Turáková M., Salmi T., Eränen K., Wärnå J., Murzin D. Yu., Králik M., *Applied Catalysis A: General*, 499 (2015) 66–76.

[8] Liu Y., Fang Y., Lu X., Wei Z., Li X., *Chemical Engineering Journal,* 229, (2013), 105–110.

[9] Rodriguez Ph., Simescu-Lazar Fl., Meille V., Bah Th., Pallier S., Fournel I., *Applied Catalysis A: General,* 427– 428, (2012), 66– 72.

[10] Argesanu C., Bombos D., Matei V., Juganaru T., Bombos M., Vasilievici G., *Revista de Chimie*, 65, (11), (2014), 1391-1394.

[11] Garda, K.H., Slepcevich, C.M., *Ind. Eng. Chem.*, **32**, (1960), 417.

[12] Amon, B., Redlingshofer, H., Klemm, E., Dieterich, E., Emig, G., *Chem. Eng. Process,* 38, (1999), 395.

CRITICAL VARIETY UNDER PARAMETRIC UNCERTAINTY FOR THE BENZENE OXIDATION INDUSTRIAL CATALYTIC REACTOR

Constantin MUSCALU[1] and Gheorghe MARIA

University Politehnica of Bucharest, Department of Chemical and Biochemical Engineering, 1-7 Polizu street, Bucharest, Romania

Abstract
The need for safety in daily activities is one of the main concerns of the contemporary society. Therefore operational safety in industrial activities has become a standard and not just a concept. This standard is provided by OSHA in USA and by SEVESO Directives in European Union. The safe operation of equipment / plants prevents major accidents and irreversible environmental pollution which is a major concern nowadays. Safe operation is viewed with a high responsibility by all involved parties, from the process researchers/ plant designers to workers involved in the plant operation. Maximizing the profit by increasing the productivity and reducing the risk are both common criteria used to optimise the plant operation by using engineering evaluation tools, and mathematical modelling procedures applied to the system analysed in order to obtain satisfactory trade-off results. Safe operation of highly thermally sensitive industrial catalytic reactors remains a major engineering issue when highly exothermic reactions are conducted under randomly fluctuating operating variables, and especially when the set-point is located in a close vicinity of the runaway boundaries from the market pressure to increase the reactor productivity.

Key words: runaway boundaries; confidence region; catalytic reactor; maleic anhydride production

1. Introduction

The need for safety in daily activities is one of the main concerns of the contemporary society. Therefore operational safety in industrial activities has become a standard and not just a concept. This standard is provided by OSHA in USA and by SEVESO Directives in European Union. The safe operation of equipment / plants prevents major accidents and irreversible environmental pollution which is a major concern nowadays.

Safe operation is viewed with a high responsibility by all involved parties, from the process researchers/ plant designers to workers involved in the plant operation. Maximizing the profit by increasing the productivity and reducing the risk are both common criteria used to optimise the plant operation by using

---

[1] Corresponding author; E-mail address: c_muscalu@chim.upb.ro (Constantin Muscalu)

engineering evaluation tools, and mathematical modelling procedures applied to the system analysed in order to obtain satisfactory trade-off results.

Safe operation of highly thermally sensitive industrial catalytic reactors remains a major engineering issue when highly exothermic reactions are conducted under randomly fluctuating operating variables, and especially when the set-point is located in a close vicinity of the runaway boundaries from the market pressure to increase the reactor productivity [1-4].

This study is aiming to derive the runaway boundaries and their associated region of confidence in the operating variable space for such a risky fixed-bed catalytic reactor by applying a very effective Morbidelli & Varma generalized criterion [1]. Chemical reactor's technological constraints and runaway boundaries of the operating conditions are important for risk assessment, reactor optimal operation, and over-design avoidance. The aim of this paper is to point-out the higher accuracy of risk assessment when using extended kinetic model in evaluating the runaway boundaries for an industrial fixed-bed multi-tubular catalytic reactor. A concrete example is provided for the exothermic benzene oxidation to maleic anhydride in vapour-phase. The Morbidelli-Varma sensitivity criterion has been used, proving the biased predictions generated with the extended kinetic model under the same nominal set of reaction conditions. To illustrate the parametric sensitivity analysis, the case of gaseous phase catalytic oxidation of benzene to maleic anhydride was considered [5]. The oxidation reaction is complex, with successive and parallel reactions, involving a relative large number of intermediate products. For a more accurate evaluation of the reactor critical operating conditions a complex reaction kinetic model from literature was used (Fig. 1, and [5]).
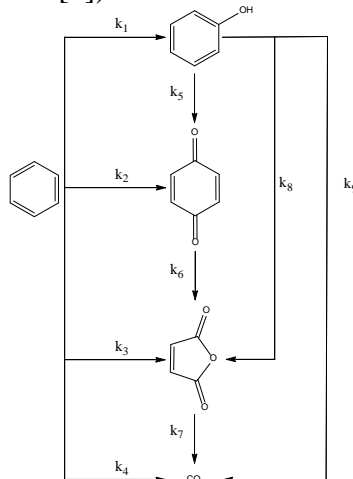
Fig.1. Chemical reactions involved in the oxidation of benzene [6]

The extended description of the reactor model and the kinetic constants for benzene oxidation was done by Muscalu and Maria in 2014 [5].

2. Results and discussions

Thermal and risk analysis of the reactor begins by determining the operating variables which have a strongly influence to the process performance (final conversion of the reactants) and the maximum temperature rise in the reactor (thermal spot value). Simulating the reactor behaviour under nominal operating conditions (Table 1), but every time perturbing one of the operating variables (within his min-max range), it is possible to point out the reactor sensitivity to various operating parameters and rank their individual influence [5].

Table 1.

Industrial catalytic reactor and process characteristics

Catalyst density (bulk) [4]	$\rho_c = 1260 \ \text{kg/m}^3$		
Catalyst particle average diameter (similar to [4])	$d_p = 0.005 \ m$		
Total pore volume [6]	$V_{TP} = 0.4 \ \text{m}^3_{void}/\text{m}^3_{bulk}$		
Fixed-bed void fraction	$\varepsilon = 0.48$		
Tortuosity	$\tau = 2.01$		
Pipe inner diameter	$d_t = 24 \ mm$		
Reactor length	$L = 4 \ m$		
Operating conditions:	Minimum	Nominal	Maximum
Inlet total pressure	$p_0 = 1,6 \ atm$	$p_0 = 3 \ atm$	$p_0 = 4 \ atm$
Inlet gas temperature	$T_0 = 305 \ ^oC$	$T_0 = 385 \ ^oC$	$T_0 = 405 \ ^oC$
Benzene inlet molar fraction	$y_{B,0} = 0.007$	$y_{B,0} = 0.014$	$y_{B,0} = 0.018$
Cooling agent average temperature	$T_a = 300 \ ^oC$	$T_a = 380 \ ^oC$	$T_a = 400 \ ^oC$
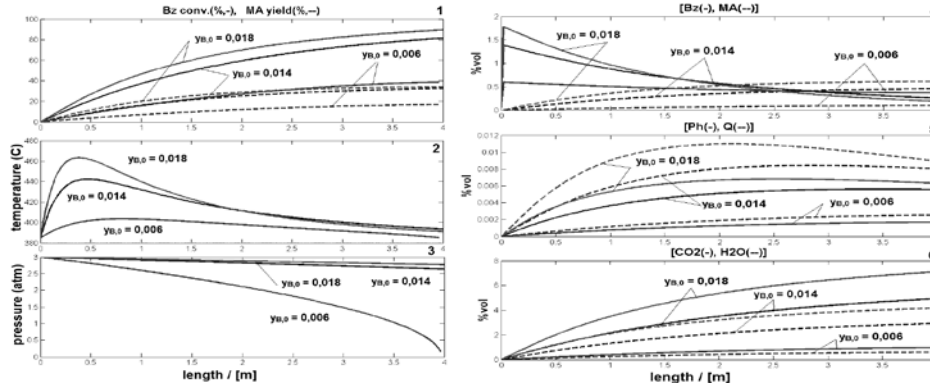
Fig. 2. Axial profiles of temperature (2), benzene conversion (%) and yield in maleic anhydride (%) (1), total pressure (3) and molar fractions of the species (4 – 6) for different values of feed benzene molar fraction ($y_{B,0}$) (adapted from Muscalu and Maria [5])

In order to analyze the influence of the operating parameters uncertainty, the running parameters considered as fluctuating randomly around the nominal values ("set-point" with a fluctuation considered to be normally distributed), on the critical operating conditions assessment accuracy for a fixed bed multi-tubular catalytic reactor, the Morbidelli-Varma sensitivity criterion has been used. Sensitivity functions time/reactor length dependent $s(y;\phi)_z = \partial y(z)/\partial \phi$ are evaluated by considering the following state variables: inlet temperature, feed pressure, benzene inlet molar fraction and cooling agent temperature. Absolute sensitivity can be calculated by integrating the differential equations of sensitivity with the reactor model [1, 2]. Model Jacobian and local sensitivities $\partial y(z)/\partial \phi$ were numerically evaluated by using the finite differences method, with an important computational effort. Based on evaluation of the sensitivity functions $S(T;\phi)_z$, (index z denoting their dependence on reactor length) application of the generalized MV criterion identifies the critical operating conditions by determining the maximum absolute value of maximum temperature sensitivity with respect of a reference parameter ϕ, $T_O \, | S(T_{\max};\phi)|$, before the temperature maximum with respect of reactor length appears.

The resulting values for the sensitivity functions $u_{j,c}(\phi_j) = max \left| s(T_{max};\phi_j) \right|$. For the case of $\phi_j = y_{Bo}$ (**i.e.** feed benzene molar fraction) and various control variables T_O, P_O and T_a [5], the resulted dependences are represented in Fig. 3 (left) for different values of the control variable u_j. The graphical representation of the positions of the $S(T_{\max};y_{Bo})$ -vs y_{Bo} maximum, with respect to the reference variable u_j, leads to set the runaway boundaries in every parametric

plane $y_{B0,c}$ -vs.- u_j , as represented in Fig. 3 (standard deviations are indicated for every control variable / operating parameter in the figure caption, leading to a corresponding 68% confidence interval of the risk curves in the parametric planes according to the normal distribution of the control variable fluctuations).
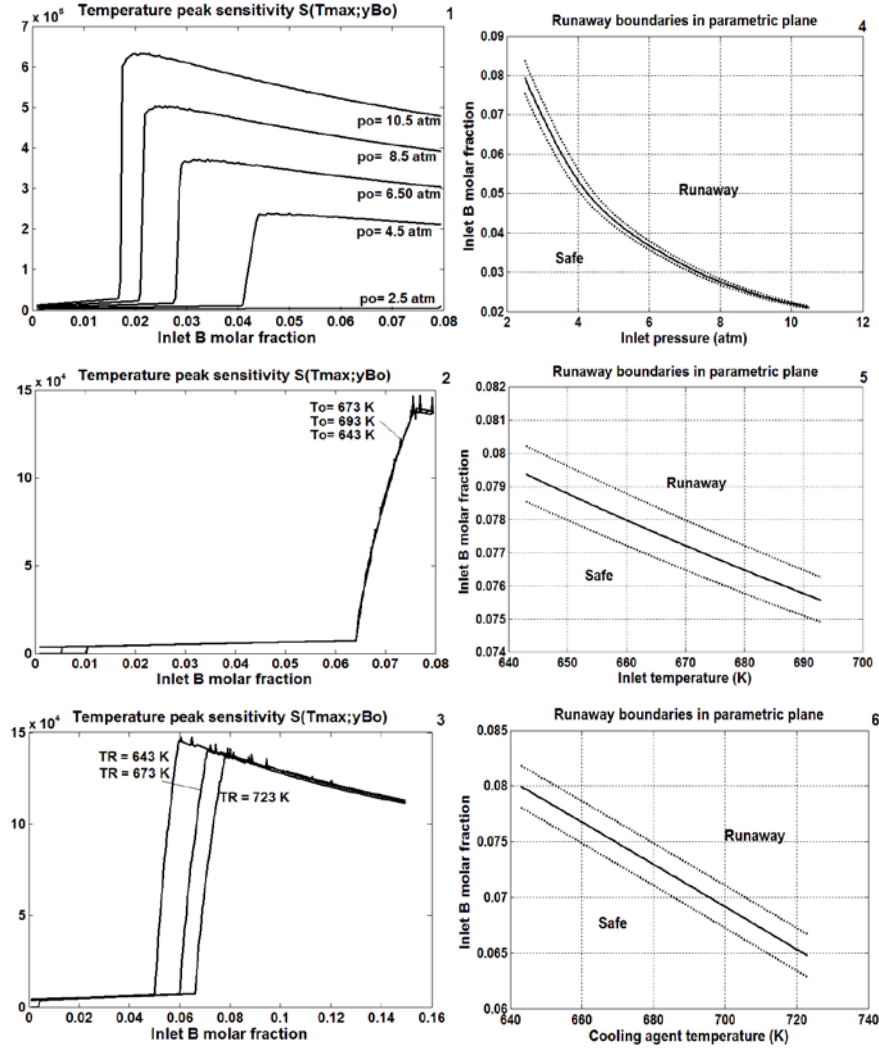
Fig. 3. (Left: 1-3) Sensitivity of the temperature maximum in the fixed-bed reactor vs. the inlet benzene molar fraction $S\left(T_{\max};y_{Bo}\right)$ for different operating parameters ($\phi_j = p_0$, $\phi_j = T_0$, and $\phi_j = T_a$). (Right) Runaway boundaries (¯) in the parametric plane [y_{B0} vs. P_o] (up-4), [y_{B0} vs. T_0] (centre-5), [y_{B0} vs. T_a] (down-6) and its confidence band for parametric deviations $\phi_j \pm \delta\phi_j$ with $\delta p_o = 0.2$ atm (---), $\delta T_0 = 10$ K (---), $\delta T_a = 10$ K (---).Notation "B" on axes denotes benzene. (adapted from Muscalu and Maria [5]).

16

3. Conclusions

From the above results we can conclude that by increasing the severity of the operating conditions, which leads to increased reactor productivity, more restrictive runway boundaries in the parametric plane are obtained. This conclusion has a high practical importance for the determination of the nominal operating point taking into account not only the optimization of the economic objective (productivity), but also the safety objective which can lead to an acceptable compromise.

Another aspect investigated is related to uncertainty in assessing the safety limits of the operating region associated with random operating variable, ϕ_j, fluctuations around the nominal operating point on a given interval, $\phi_j \pm \partial\phi_j$. Such parameters uncertainty is generally linked to the performance of the reactor control systems. By repeated application of the MV criterion, taking as values lower and upper limits of the parameters, lower and upper limits of critical operating conditions can be calculated. Even if being more computational and requiring extensive information on the process, the present study proves the advantages of using of a model-based and a more sophisticated sensitivity criterion (such as the robust z- MV) to determine the runaway boundaries and their confidence in the parametric space, with accounting for parameter random fluctuations around the set point.

REFERENCES

[1] Varma, A., Morbidelli, M., Wu, H., 1999, *Parametric sensitivity in chemical systems*, Cambridge University Press: Cambridge (MS).
[2] Maria, G., 2007, *Chemical Process Quantitative Risk Analysis and Modelling of Accident Consequences*, Printech Publ., Bucharest (in Romanian).
[3] Maria, G., Stefan, D.N., Variability of the risk operating limits with the catalyst properties in a fixed-bed vapour-phase catalytic reactor for nitrobenzene hydrogenation, *Jl. Loss Prevention in the Process Industries*, 23, (2010),112–126.
[4] Maria, G., Dan, A., Setting optimal operating conditions for a catalytic reactor for butane oxidation using parametric sensitivity analysis and failure probability indices, *Jl. Loss Prevention in the Process Industries*, 25, (2012), 1033-1043.
[5] Muscalu, C., Maria G., Critical variety under parametric uncertainty for the benzene oxidation industrial catalytic reactor, *Environmental Engineering and Management Journal,* 2014, (in press).
[6] Lupuşor, G., Merica, E., Gorea, C., Bucea-Gorduza, V., 1981, *Synthesis of aromatic intermediates engineering*, 1, Ed. Tehnica, Bucharest, (1977); 2, Ed. Tehnica, Bucharest, (in Romanian).

Dr. Gheorghe Maria received his MSc (1979), and PhD (1987) in Chemical Engineering from University Politehnica of Bucharest - UPB (Romania). Currently he is a Professor with the Dept. of Chemical & Biochemical Engineering of UPB. Over his career he was employed as a plant chemical engineer (1979-1982) in Bucharest, research engineer with Chem. & Biochem. Energetics Institute Bucharest (1982-1990), lecturer with UPB (1991), Res. and Asstn. Professor with ETH Zürich (1992-1996, Chemical Eng. Dept.), Assoc. Professor with UPB (1997-1998), and full Professor with UPB (from 1999). He (co-)authored more than 133 papers in international ISI quoted journals (h-index = 15, more than 700 citations), 7 teaching books (in Romanian), ca. 70 papers in intl. conference proceedings, and others papers in national journals and conferences. He completed a large number of stages abroad working in the framework of intl. projects at ETH Zürich (Aug.-Oct., 1997), Univ. des Saarlandes (June-Sept., 1999), Univ. of Porto (Nov.-Dec., 2000), TU Erlangen (June-Sept., 2000)

Texas A&M University (2002-2003), TU Braunschweig (July 2006), TU Hamburg (June-Aug., 2009), Tianjin Inst. of Ind. Biotechnology of Chinese Academy (July-Aug., 2010). His research interest includes (bio)chemical reactor and kinetic modelling, statistical estimation, process identification and optimization, bioengineering and bioinformatics, risk analysis, modelling metabolic processes and genetic regulatory networks in living cells, drug release kinetics. Supplementary information is available on his ResearcGate page, and

https://sites.google.com/site/gheorghemariasite/

Chem. Eng. Constantin Muscalu received his BSc (2011) as valedictorian of the faculty, and MSc (2013) in Chemical & Biochemical Engineering from University Politehnica of Bucharest (Romania), being currently a PhD student candiadate with the Dept. of Chemical & Biochemical Engineering and a Process Safety Consultant at Siemens SRL. He co-authored 4 papers in national and international journals. Supplementary information is available on his page on ResearcGate page.

CONTROLLABILITY OF BIOETHANOL DEHYDRATION PROCESS USING A PRESSURE-DRIVEN DYNAMIC MODEL

Iulian PĂTRAŞCU, Costin Sorin BÎLDEA[*]

University "Politehnica" of Bucharest, Faculty of Applied Chemistry and Materials, Department of Chemical and Biochemical Engineering, 1-7 Polizu street, Bucharest, 011061, Romania

Abstract

The paper considers the dynamic simulation and control of an optimally-designed bioethanol dehydration plant. The plant consists of three distillation steps implemented in pre-concentration, extractive and recovery columns. The pressure-driven dynamic simulation implemented in AspenDynamics takes into account the hydraulic equipment such as pumps and valves, being more realistic compared to a flow-driven simulation. The control structure includes conventional level, temperature, pressure, concentration and ratio loops. The excellent performance of the control system is proved for disturbances in the feed flow rate (± 20%) and feed composition (8 – 12% wt. ethanol).

Key words: bioethanol, dehydration, process design, dynamics, process control, pressure-driven simulation

1. Introduction

Followed by biodiesel, bioethanol is the most produced type of biofuel. Bioethanol is produced by fermentation of raw materials containing sugar, starch or cellulose. The concentration of ethanol in the fermentation broth is rather low, below 15% (wt.). Additionally, ethanol and water form a minimum-boiling azeotrope (95.63% wt. ethanol). Therefore, dehydration of ethanol to the purity level required by the car engines is a costly step.

The typical process for ethanol dehydration involves a pre-concentration step, where a near-azeotrope ethanol-water mixture is obtained, followed by breaking the ethanol-water azeotrope by means of extractive distillation using ethylene glycol as a mass-separating agent. Kiss and Ignat [1] discuss the optimal design of a bioethanol dehydration plant, showing that the optimal concentration of pre-concentrated ethanol is 91% (wt.). Dynamics and control is as important as economic optimization. Kiss, Ignat and Bîldea [2] developed a flow-driven Aspen

Dynamics simulation of the ethanol dehydration plant, which was used to prove the controllability of the optimal design. Although *flow-driven* simulation can be used for a quick assessment of the plant controllability, *pressure-driven* simulation is needed when a more realistic dynamic model is required. However, pressure-driven dynamic simulation is more challenging as it involves more detailed modelling of the pressure changes across the plant by means of the pumps, compressors, valves, and other hydraulic elements. Therefore, the goal of this work is to develop a pressure-driven dynamic simulation of the bioethanol dehydration plant and to use this model for a controllability study.

This paper is organized as follows. In section 2 is described the bioethanol purification plant, giving detailed unit sizing and stream report. Then, the development of a pressure-driven dynamic simulation is presented, including details regarding the control structure, controller tuning, design of pumps and valves. The next section shows results of dynamic simulation, proving that the optimal bioethanol dehydration plant is controllable even when large disturbances in feed rate or feed composition are present. The paper ends with conclusions.

2. Process description

Ignat and Kiss [1] describe plant for bioethanol dehydration by extractive distillation (Fig. 1). For reader's convenience, we repeat here the main results [1].
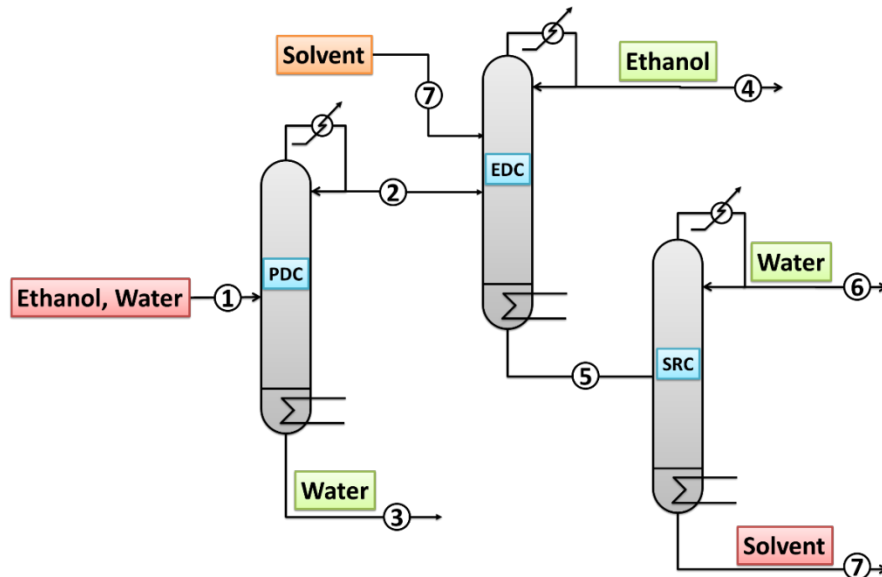
Fig. 1. Bioethanol purification plant

20

The ethanol dehydration is based on extractive distillation using ethylene glycol as solvent. The plant contains three distillation steps. First, the pre-concentration column (PDC) takes the initial 10% wt. ethanol-water mixture and concentrates it to 91% (wt.). The bottom product of PDC is 99.99% (wt.) pure water. Secondly, the extractive distillation column (EDC) takes the 91% wt. ethanol mixture and dehydrates it to 99.8% wt. using ethylene glycol for breaking the azeotrope. Finally, the last column (SRC) recovers the solvent, which is recycled to EDC.

A steady-state simulation was developed in Aspen Plus [3], based on the design parameters provided by reference [1]. The NRTL model [4] was used to represent the non-ideality of the liquid phase, all the binary interaction parameters being available in the Aspen Plus database. Table 1 presents a summary of plant mass balance together with the main characteristics of each column.

Table 1.

Stream report and unit sizing

	COLUMNS									
	PDC			EDC				SRC		
	IN	OUT		IN		OUT		IN	OUT	
STREAMS	1	2	3	7	2	4	5	5	6	7
Temp., °C	25	77.9	106.9	25	78.3	78	156.8	157.1	99.6	201
Pressure bar	1.18	1	1.29	1.03	1.1	1	1.16	1.07	1	1.15
Mass Flow kg/hr	125000	13735	111265	20798	13735	12525	22008	22008	1215	20793
Ethanol kg/hr	12500	12499	1.19	trace	12499	12498	0.773	0.773	0.773	trace
Water kg/hr	112500	1236	111264	4.7	1236.3	22.0	1219	1219	1214	4.77
Ethylene Glycol kg/hr				20793		4.955	20788	20788	0.018	20788
Number of stages	30			17				16		
Feed stage	19			4		11		8		
Diameter [m]	2.89			1.4				0.89		
Reflux ratio	1.31			0.24				0.45		
Condenser duty [kW/hr]	-8653			-3686				-1106		
Reboiler duty [kW/hr]	20425			5738				1793		

Temperature and composition profiles along the pre-concentration (PDC), extractive distillation (EDC) and solvent recovery (SRC) columns are presented in Figs. 2-4, respectively.
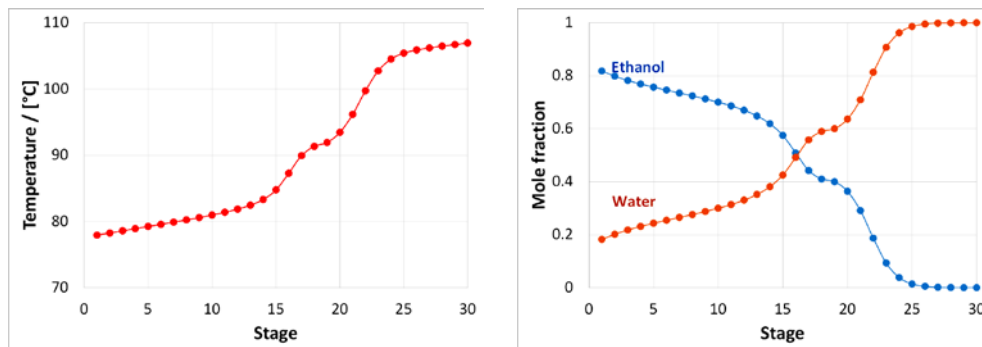
Fig. 2. Temperature and composition profiles along the pre-concentration column (PDC)
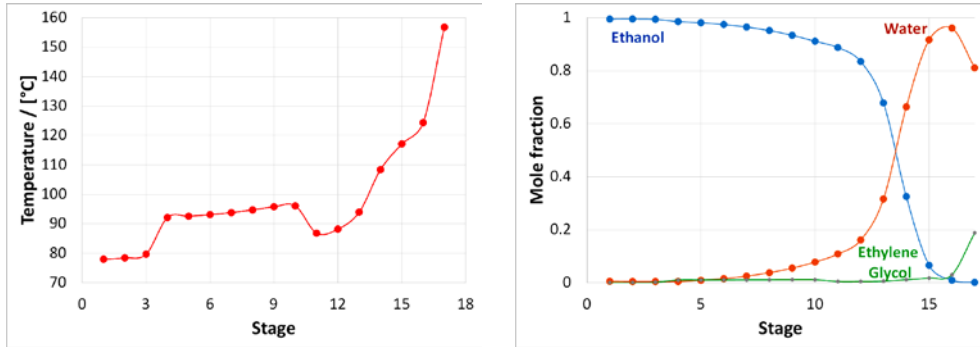
Fig. 3. Temperature and composition profiles along the extractive distillation column (EDC)
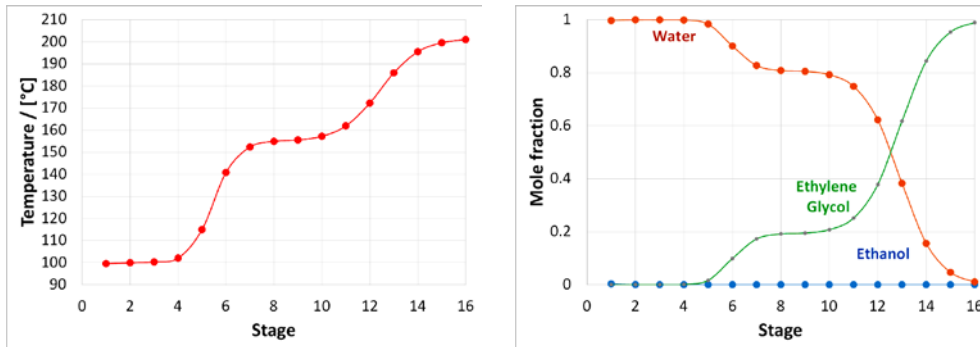
Fig. 4. Temperature and composition profiles along the solvent recovery column (SRC)

3. Dynamics and control

The complete flowsheet, including the control loops, is presented in Fig. 5. The control of each distillation column is standard: the pressure is controlled by condenser duty; the sump and reflux drum levels are controlled by valve opening on the bottoms and distillate lines, respectively; one temperature in the stripping section is controlled by the reboiler duty. In the PDC, the reflux rate is kept constant. In the EDC and SRC, the mass reflux is used to control one temperature in the rectifying section. The trays used for temperature control were chosen as the most "sensitive" trays of the columns temperature profile [5]. The mass fraction of water in the ethanol product is measured by a concentration analyzer and kept at its setpoint by changing the EDC solvent / feed ratio. The level in the solvent buffer tank is controlled by the solvent makeup.
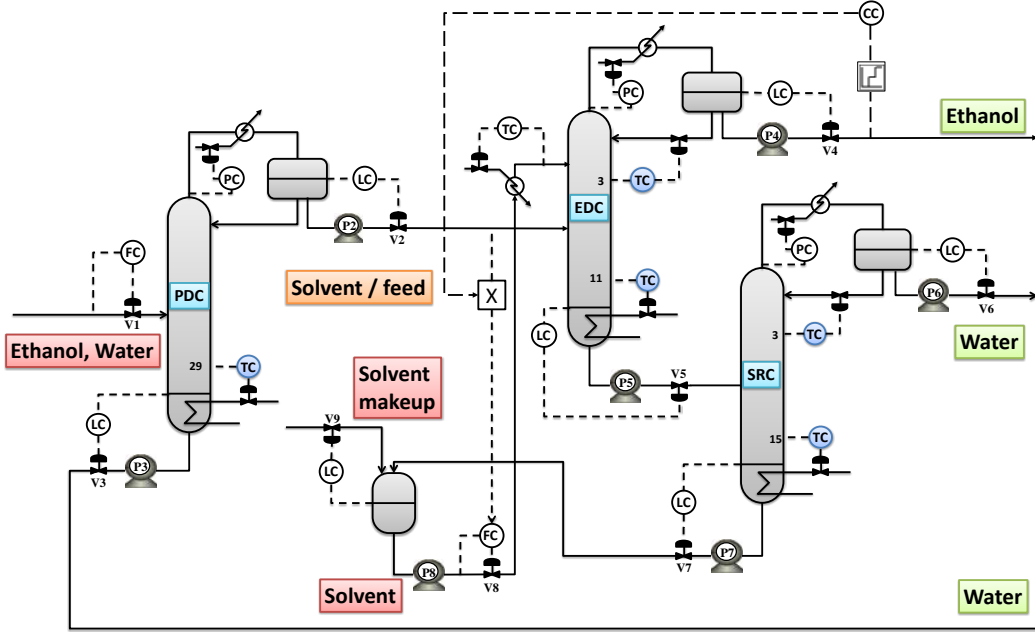
Fig. 5. Bioethanol purification plant dynamic control structure

A pressure-driven dynamic simulation was developed using Aspen Dynamics. All vessels were sized based on 10 minutes residence time. The column diameter was obtained using the "tray sizing" facility offered by Aspen Plus.

Pressure-driven simulation requires specification of hydraulic elements, like the flow rate across a valve. In *pressure-driven* simulation, the flow rate F_{mass} is calculated based on the pressure difference between the upstream and downstream ΔP, fluid density ρ, valve opening x and valve characteristics $C_{0,max}$ and $f(x)$, as shown by equation (1). Therefore, one has to provide the valve characteristics $C_{0,max}$ and $f(x)$ and to include in the simulation the pumps necessary to achieve the required pressure difference ΔP. In contrast, in a *flow-driven* dynamic simulation, the flow rates are specified, assuming that they can be achieved by means of suitable pumps, valves and flow controllers. Compared to flow-driven simulation method, the pressure-driven mode is more realistic because it is closer to the real physical process.

$$F_{mass} = C_{0.max} \cdot f(x) \cdot \sqrt{\frac{\rho * \Delta P}{2}} \qquad (1)$$

A key factor to process control is the ability to change various flow rates as response to disturbances affecting the process. It should be noted that the control engineer wants high pressure drop across the valves, because this increases the range of flow rates which can be achieved by opening or closing the valve [6]. In contrast, the chemical engineer wants a small pressure drop across the valves, because this requires less pumping power. Therefore, a compromise has to be found. Table 2 presents the characteristics of the pumps (maximum flow rate F_{max} and maximum head H_{max}) and valves (valve coefficient $C_{0,max}$ and pressure drop ΔP at 50% opening and nominal process conditions).

Table 2.

Pumps and valves characteristics

FLOW CONTROLER		PUMP			VALVE		
			F_{max}	H_{max}		$C_{0,max}$	ΔP
			$[m^3/h]$	$[m]$		$[m^{1.5} kg^{0.5}/h \cdot bar^{0.5}]$	bar
PDC	FEED				V1	5804.107	3.7
	DISTILLATE	P2	18.316	67.993	V2	641.119	5.1
	BOTTOM	P3	122.147	55.972	V3	4663.615	5.0
EDC	DISTILLATE	P4	17.050	69.437	V4	584.656	5.0
	BOTTOM	P5	22.323	51.703	V5	878.980	5.1
SRC	DISTILLATE	P6	1.328	66.620	V6	46.504	7.0
	BOTTOM	P7	22.027	63.194	V7	781.634	6.0
SOLVENT FEED		P8	22.041	21.613	V8	1364.498	2.0
SOLVENT MAKEUP					V9	0.171	6.0

All the controllers are PI type. Controller tuning was achieved by the following procedure. For each control loop, appropriate ranges of the process variable PV and controller output OP where chosen around the nominal values, based on the accepted variation of PV from its setpoint and the maximum change of the manipulated variable OP. Then the controller gain was set to 1 %/%. The reset time was set equal to an estimated value of the process time constant. The tuning of ethanol concentration controller (denoted by CC in Fig. 5) was achieved by finding the stability limit using the ATV procedure [6] and using the Tyreus-Luyben settings [6]. Details of the control loops are presented in Table 3.

The performance of the control system with respect to feed rate disturbances is presented in Fig. 6. The simulation starts from steady state. The feed flow rate is increased from 125,000 kg/h to 150,000 kg/h in two steps at time $t = 6$ h and $t = 14.5$ h. Then, the flow rate is decreased to 100,000 kg/h in several steps (at time $t = 24, 34, 43$ and 49 h) and then (at time $t = 54$ h) brought back to the initial value. The product flow rates (water and ethanol) change accordingly to the feed. Moreover, the flow rate of solvent to the EDC column is adjusted to

match the flow rate of ethanol-water mixture fed to the EDC column. Despite the large disturbances, the product purities remain high, close to the nominal values.

Table 3.

Controller tuning

Controller		PV, value & range	OP, value & range	Kc, %/%	Ti, min
MIXER					
	LC	Level = 1.65 m	valve opening = 50%	1	10
		1 … 3.31m	0 … 100 %		
ETHANOL CONCENTRATION PRODUCT					
	CC	Water % wt. = 1518.607 ppm	solvent/feed = 1.514214		
		0 … 3037.21 ppm	0 … 3		
COOLER					
	TC	Temperature = 25 °C	cooler Duty = -9.83 GJ/h	1	20
		23 … 26 °C	(-19.66… 0 GJ/h)		
ETHANOL - WATER (FEED)					
	FC	F1 feed flow = 125000 kg/h	valve opening = 50%	1	1
		93750 … 156250 kg/h	0 … 100 %		
SOLVENT (FEED)					
	FC	F2 feed flow = 20797 kg/h	valve opening = 50%	1	1
		0 … 60000 kg/h	0 … 100 %		
PDC					
	PC	Pressure = 1 bar	condenser duty = -31.15 GJ/h	20	12
		0 … 2 bar	(-62.30 … 0) GJ/h		
	LC	reflux drum level = 2.06 m	valve opening = 50	1	20
		0 … 4.12 m	0 … 100 %		
	LC	Sump level = 3.1 m	valve opening = 50	1	20
		0 … 6.3 m	0 … 100 %		
	TC	stage 29 temperature = 106.7 °C	reboiler duty = 73.53 GJ/h	1	20
		105 … 108 °C	0 … 147.06 GJ/h		
EDC					
	PC	Pressure = 1 bar	condenser duty = -13.27 GJ/h	20	12
		0 … 2 bar	(-26.52 … 0) GJ/h		
	LC	reflux drum level = 1.6365m	valve opening = 50	1	20
		0 … 3.27 m	0 … 100 %		
	LC	Sump level = 1.89 m	valve opening = 50	1	20
		0 … 3.79 m	0 … 100 %		
	TC	Stage 3 temperature = 79.7 °C	reflux = 3004 kg/h	1	20
		78 … 81 °C	0 … 6009 kg/h		
	TC	stage 16 temperature = 123 °C	reboiler duty = 20.63 GJ/h	1	20
		122 … 125 °C	0 … 41.27 GJ/h		
SRC					
	PC	Pressure = 1 bar	condenser duty = -3.98 GJ/h	20	12
		0 … 2 bar	(-7.96 … 0) GJ/h		
	LC	reflux drum level = 0.7352 m	valve opening = 50	1	20
		0 … 1.47 m	0 … 100 %		
	LC	Sump level = 1.83 m	valve opening = 50	1	20
		0 … 3.66 m	0 … 100 %		
	TC	Stage 15 temperature = 199.50 °C	reboiler duty = 6.47 GJ/h	1	20
		198 … 201 °C	0 … 12.95 GJ/h		
	TC	Stage 3 temperature = 100.25 °C	reflux = 549.06 kg/h	1	20
		99 … 102 °C	0 … 1098.13 kg/h		
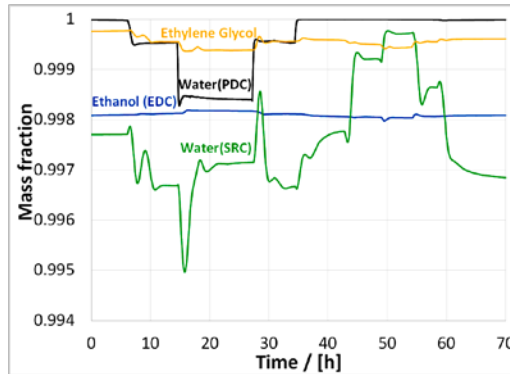
Fig. 6. Dynamic simulation results – change of the feed flow rate

The performance of the control system with respect to feed composition disturbances is presented in Fig. 7. As the ethanol concentration is changed from 10% wt. to 12% wt. or 8% wt., the purity of the ethanol product exceeds 99.8% wt. specification. The purity of water product also remains high.
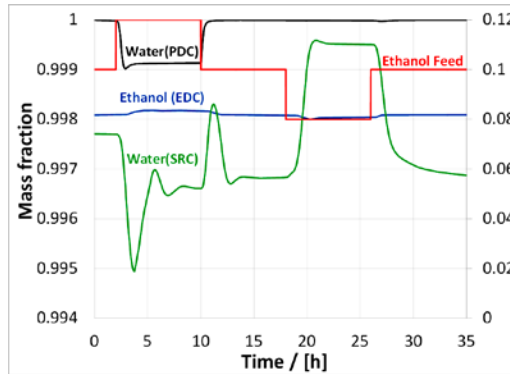
Fig. 7. Dynamic simulation results – change of the feed composition

4. Conclusions

Ethanol dehydration can be achieved by a sequence of three distillation columns: pre-concentration to near azeotropic composition, breaking the ethanol – water azeotrope by extractive distillation and solvent recovery. The pressure-driven dynamic simulation developed in this work provides a realistic and reliable model of the plant behavior. The optimally-designed plant investigated in this work shows excellent controllability properties: the product purities are kept on-spec despite large disturbance in feed flow rate and composition.

REFERENCES

[1] Kiss A. A., Ignat R. M., *Optimal Economic Design of an Extractive Distillation Process for Bioethanol Dehydration*, Energy Technology, 1(2-3), (2013), 166-170.

[2] Kiss A. A., Ignat R. M., Bildea C. S., *Optimal Extractive Distillation Process for Bioethanol Dehydration*, Computer Aided Chemical Engineering, 33, (2014), 1333–1338.

[3] Stanley I. Sandler, Using Aspen Plus in Thermodynamics Instruction: A Step-by-Step Guide.

[4] Poling B. E., Prausnitz J. M., O'Connell J. P., *The Properties of Gases and Liquids*, McGraw-Hill, New York, 2004.

[5] Luyben W. L., D*istillation Design and Control Using Aspen^{TM} Simulation*, John Wiley & Sons, Hoboken, 2006.

[6] Luyben W. L., Luyben M. L., *Essentials of Process Control*, McGraw-Hill, New York, 1998.

Kinetic analysis of the native *E. coli* strain cultivation in a fed-batch bioreactor

Alina TANASE, Valentina GOGULANCEA, Gabriela ISOPENCU[1], Vasile LAVRIC

University "Politehnica" of Bucharest, Faculty of Applied Chemistry and Materials Science, Department of Chemical and Biochemical Engineering, 1-3 Polizu street, Bucharest, 011061, Romania

Abstract
The development of technologies of recombinant protein over the past decades has favored the use of E. coli as a host for heterologous protein expression, due to its structural simplicity and ease way of cultivation. In order to achieve a better control of the process and expected efficiency, the understanding of bacterial dynamic's growth is of major importance. The present paper proposes and tests several models for the growth kinetics of E. coli BL21 (DE3) strain in a fed-batch experimental set-up. We investigate in this paper the suitability of unstructured and unsegregated Monod based kinetic models, taking into account substrate and biomass inhibition effects. The model's parameters (affinity constant, specific growth rate, inhibition constants) are determined by regression analysis using our own experimental data. The results of the modeling study can offer valuable information upon the dynamics of E.coli population, for extreme conditions such as wash-out or starvation.

Key words: *E. coli*, Monod model, genetic algorithms

1. Introduction

Monod's growth model (1941, 1949, 1950) was proposed as a microbial growth kinetics, namely, the relationship between the specific growth rate (μ) of a microbial population and the substrate concentration (S), is an indispensable tool in all fields of microbiology, be it physiology, genetics, ecology, or biotechnology. Therefore it is an important part of the basic knowledge of microbiology [1]. Monod's growth model (1949) was proposed as an empirical model to describe microbial growth, including the effect of nutrient concentration, and is based on observations of the growth of *E. coli* at various glucose concentrations, assuming that glucose is the limiting substrate [2]. The model relates the specific growth rate to the substrate concentration by the Monod equation (1):

---

[1] Corresponding author; E-mail address: g_isopencu@chim.upb.ro (Gabriela Isopencu)

$$\mu = \mu_{max} \cdot \frac{S}{K_S + S} \tag{1}$$

where: μ - specific growth rate (h^{-1}), μ_{max} - maximum specific growth rate (h^{-1}), K_S - the affinity constant (g/L) and S - the concentration of growth-limiting substrate (g/L) [2].

Bacterial growth could experience several types of inhibition which may include: the substrate inhibition, at high concentration, the product inhibition, which may have two levels – a concentration from which growth is hindered and another, higher concentration, which might be lethal and even enzymatic poisoning. When several substrates are used simultaneously with no limitation of concentration, the kinetics of growth become more complicated [3], e.g., when the substrate concentration is the cause of inhibition, growth can no longer be unlimited. The following equations are able to describe various types of substrate inhibition (eq. 2 – 3) [4]:

$$\mu = \mu_{max} \cdot \frac{S}{K_S + S} \cdot \frac{K_i}{K_i + S} \tag{2}$$

$$\mu = \mu_{max} \cdot \frac{S}{K_S + S + \frac{S^2}{K_i}} \tag{3}$$

where K_i is the inhibition constant.

The product concentration can also have a detrimental impact on the cellular development, as the model proposed by Levenspiel (1980) [4]. This model introduces, compared to the Monod model, new parameters, such as the product concentration (P) (g/L) and the critical product concentration at which the rate is null (P*) (g/L) [4]:

$$\mu = \mu_{max} \cdot \left(1 - \frac{P}{P^*}\right)^n \cdot \frac{S}{K_S + S} \tag{4}$$

According to Monod model, the growth curve (Fig. 1) comprises, in a discontinuous culture: a lag phase, an accelerated growth phase, a logarithmic or exponential growth phase, a retardation phase, a stationary phase, an accelerated death phase and a logarithmic death phase. The duration of phases of microorganisms growth curves stages depends upon the temperature, pH, dissolved oxygen and culture aeration [6].

Using a fed-batch bioreactor, the growth phases will become more complicated, since the substrate is added at given intervals. A culture could, at that moments, exit the stationary phase a regain the exponential phase, for example.
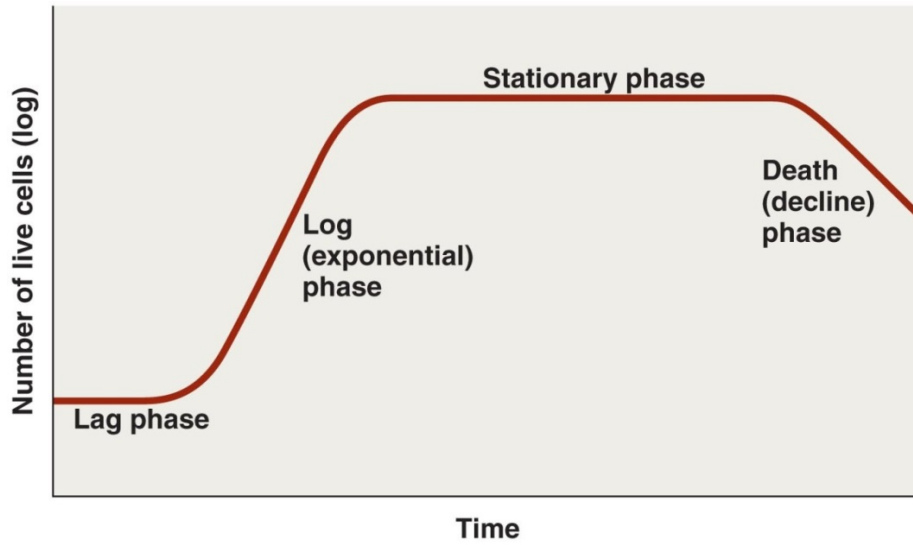
Fig. 1. Growth phases in a batch process [2]

The fed-batch bioreactors, introduced for baker's yeast production in the beginning of the last century and for antibiotics in the 1950–1960s [5], are now commonly used in industrial fermentations, for example, for the production of several enzymes, microbial cells, etc. [6]. The reason for this diversity of use is related to the theoretical analysis of many fermentation processes, which revealed the extended or exponentially fed-batch cultures to be optimal, particularly in terms of productivity [6].

Fed-batch operation often begins with an exponential feed phase of a limiting substrate, most commonly the carbon/energy source, until the limit for cooling capacity or adequate oxygen transfer is reached [5].

Characteristic equations, in pseudo - steady state and isothermal regime, are the mass balance equations for biomass and substrate, applied to the entire volume of the bioreactor [7].

Considering the yields for conversion being constant, the biomass concentration can be expressed depending on the concentration of substrate in the following equation:

$$X = (S_0 - S) \cdot Y_{XS} + X_0 \tag{5}$$

The total time for the batch bioprocess is obtained from the mass balance of the participants at the fermentation process, applied to the all reaction volume:

$$\frac{dX}{dt} = v_{RX} = \mu \cdot X \tag{6}$$

In bioprocess without product inhibition, the expression of total time of batch is given by the relationship:

$$t = \frac{1}{\mu_{max}} \cdot \left(1 + \frac{K_S}{S_0 + Y_{SX} \cdot X_0}\right) \cdot ln\left(\frac{X}{X_0}\right) + \frac{K_S}{(S_0 + Y_{SX} \cdot X_0) \cdot \mu_{max}} \cdot ln\left(\frac{S_0}{S}\right) \quad (7)$$

When the product inhibition interferes, for n=1 (eq. 4) and $K_S \ll S$, the duration of batch depends of critical product concentration:

$$t = \frac{1}{\mu_{max} \cdot Y_{PX}[X_0 + Y_{XP} \cdot (P^* - P_0)]} \cdot ln\left(\frac{P^* - P_0}{P^* - P}\right) \cdot \frac{X}{X_0} \quad (8)$$

where: X represents the concentrations of cells or biomass (g/L), X_0 is the concentration of biomass in inoculum (g/L), S_0 is the substrate concentration in the feed stream (g/L), P_0 is the product concentration in the feed stream (g/L), v_{RX} is the biomass growth rate (kg/m³h), t is the duration of the batch (h) and Y_{SX} represents the conversion yield of the substrate in biomass (kg/kg), Y_{PX} represents the conversion yield of the product obtained from biomass (kg/kg) [7].

At the time a volume of substrate (ΔV) is added, the initial concentrations of biomass and substrate should be recalculated, to take into account the dilution effect.

To determine the parameters of the bacterial kinetic of growth, the regression techniques are used. Amongst them, the most used optimization method is the genetic algorithms (GAs) technique.

GAs technique uses stochastic search algorithms based on the principles of natural (genetics) selection, able to find solutions to real world problems. The aim of GAs is evolving towards an optimal solution by letting a set of random solutions undergo a sequence of probabilistic transformations governed by a selection scheme biased towards high-quality solutions. A GAs technique emulates the biological evolutionary model to solve optimization problems. It contains a set of individual elements represented as binary strings (population) and a set of defined biological operators on the population [8].

The objective of the present work was to find a suitable model for the growth kinetics of *E. coli* BL21 (DE3) strain, in a fed-batch reactor using an experimental setup, and the GAs technique for the regression to find the model's parameters.

2. Material and methods

The experimental setup for the *E. coli* growth in fed-batch cultivation, which will be considered for the kinetics studies, was presented in a previous work [9].

2.1.Modeling setup

The growth rate, μ, was calculated using the curve of cell concentration in time, obtained by flow - cytometer measurements. The substrate concentrations, S, at different stages of growth, were determined using the dosing method of glucose (source of carbon in bacterial growth) with o-toluidine dosing kit, and the results of the colorimetric reaction were measured with a UV-visible spectrometer at 600 nm wave length.

3. Results and discussions

In this paper we tested a simple Monod model, as the product does not limit the development of the cells, there is only one substrate and multiplication of bacteria is done through binary fission. We have adopted the linear form for the equation of model (1), Lineweaver-Burk:

$$\frac{1}{\mu} = \frac{K_S}{\mu_{max}} \cdot \frac{1}{S} + \frac{1}{\mu_{max}} \tag{9}$$

As mentioned above, the growth rate was calculated using the curve of cell concentration (Fig. 2), which reveals the growth curve. Knowing the phases of the growth curve we can calculate the growth rate.

Integrating the equation (6) and applying known data, we have obtained that the growth rate is 0.2 h^{-1}.
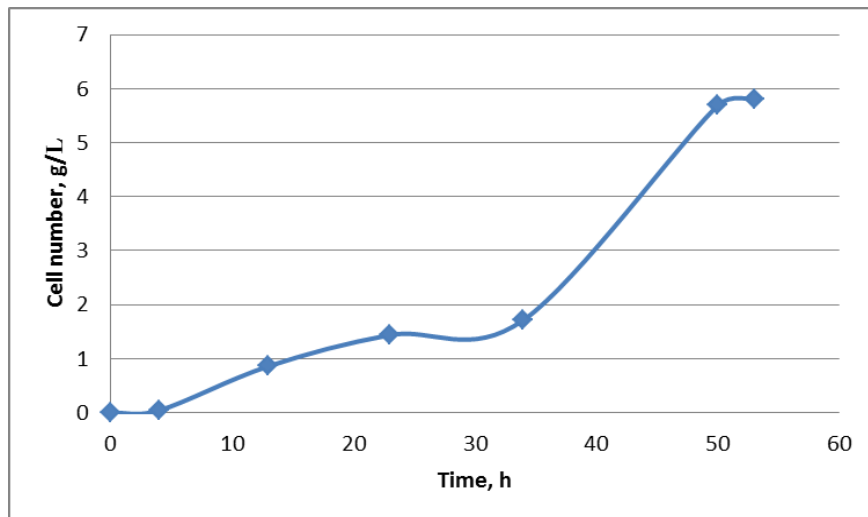
Fig. 2. The curve of cell concentration in time

According to the Monod model, the kinetic constants μ_{max} and K_S define the rate of microbial growth. To determine the kinetic parameters corresponding to the Monod model, describing the growth and multiplication of *E. coli* in the fed-batch bioreactor, genetic algorithms (GAs) will be used for regression.

In the order to identify the kinetic parameters, the final form of the Monod model equation was used, i.e. equation (9), and implemented in the Matlab environment.

For *E. coli* strains, it has been observed that during cultivation in a fed-batch culture, although the culture was already in steady state with respect to the biomass concentration, the residual substrate concentration decreased, implying that the affinity for the substrate decreased. The substrate initial concentration was 239.85 g/L and Fig. 3 shows it decreases function of time. As shown in Fig. 3, after almost 10 hours of activity, substrate concentration starts to decrease, while in Fig. 2 notice that the number of cells begins to grow. This trend is noticeable for both the experimental data and the data from the Monod equation.
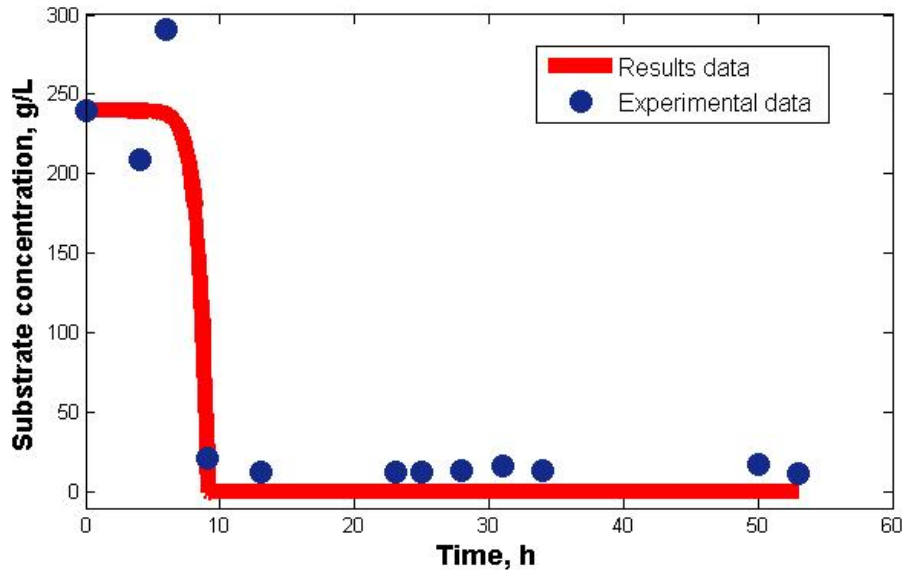
Fig. 3. Substrate concentration function of time

Typical values of μ_{max} and K_S for *E. coli* at the optimum growth temperature (37^0 C), reported in the literature, are 0.8 h^{-1} and 0.0008 g/L, as shown in Table 1. After the software solves the equation and generates the graph (Fig. 3), the kinetic constants are displayed as well. Therefore, for the *E. coli* studied culture the maximum specific growth rate is 1.493 h^{-1} and the affinity constant is 0.007674 g/L (Table 1).

Kinetic constant values

Constants Values	K_S, g/L	μ_{max}, h^{-1}
Initial	0.0008	0.8
Result	0.007674	1.493

4. Conclusions

Experimentally it was observed that as microbial cells proceed through their cellular cycle, the changes in their internal states lead to different values for the growth rates corresponding to population members of different ages, sizes etc.

Because the Monod's model is very usual, we have been used it to model the growth of *E. coli* in fed-batch reactor and we found that the parameter K_S can be estimated for one value of µmax. We can summarize the biological significance of parameters as follows. The growth of a microbial population is characterized by parameters μ_{max} and K_S. The interpretation of μ_{max} is straightforward. When the lag time, which is required to transform substrate into biomass is short, the growth is fast in the presence of an excess of substrate. The biological significance of parameter K_S is sometimes interpreted as a reflection of an intrinsic affinity of bacteria for the substrate.

A point that must be underlined is that parameter estimates are almost always reported without an indication of their confidence regions. As a consequence, it is not possible to say whether the differences between parameter values are significant or not.

Notations

Symbol	Name	Unit of measure
μ	The specific growth rate	h^{-1}
μ_{max}	The maximum specific growth rate	h^{-1}
K_S	The affinity constant	g/L
S	The concentration of growth-limiting substrate	g/L
K_i	The inhibitionconstant	g/L
P	Product concentration	g/L
P^*	Product concentration at which the rate is null	g/L
X	The concentrations of cells or biomass	g/L
X_0	The concentration of biomass in supply	g/L
t	The duration of the charge	h
S_0	The substrate concentration in	g/L

	supply	
Y_{XS}	The conversion yield of the substrate in biomass	kg/kg
v_{RX}	The biomass growth rate	kg/m^3h
v_{RS}	The consumption rate of the substrate	kg/m^3h

REFERENCES

[1] Lobry J.R., Flandrois J.P., Carret G., Pave A., Monod's bacterial growth model revisited, *Bulletin of mathematical biology*, 54, (1992), 117-122.

[2] Blanch H., Clark D., *Biochemical engineering*, University of California at Berkeley, California, 1997.

[3] Aiba S., Humphrey A., Milis N., *Biochemical engineering second edition*, Academic Press, New York and London, 1973.

[4] Nielsen J., Villadsen J., Liden G., *Bioreaction engineering principles*, Second edition, Kluwer Academic/Plenum Publishers, New York, 2003

[5] Mcneil B., Harvey L.M., *Fermentation, a practical approach*, IRL Press, Tokyo, 1990.

[6] Sandon A.M. et. all, Limiting factors in *Escherichia coli* fed-batch production of recombinant proteins, *Biotechnology and bioengineering*, 81, (2003), 158-166.

[7] Mihail R., Lavric V., Muntean O., Ingineria proceselor biochimice, *Polytechnic Institute of Bucharest*, lithography IPB., 1988.

[8] Sarkar D., Modak J., Optimisation of fed-batch bioreactors using genetic algorithms, *Chemical Engineering Science*, 58, (2003), 2283-2296.

[9] Isopencu G., Tanase A., Josceanu A.M. and Lavric V., Influence of the operating parameters on the *E. coli* BL21(DE3) growth in fed-batch bioreactor, *Revista de Chimie,* 65 (12), (2014), 1511-1516.

RHEOLOGY OF SOME SELECTED ROMANIAN HONEY

Anicuța STOICA-GUZUN, Loredana Mihaela DOBRE, Marta STROESCU, Tănase DOBRE

University "Politehnica" of Bucharest, Faculty of Applied Chemistry and Materials Science, Department of Chemical and Biochemical Engineering, 1-7, Polizu street, Bucharest, 011061, Romania

Abstract
The rheological properties of eight sorts of Romanian honey were studied at different temperatures in the range of 20-50^{0}C. Arrhenius model was used to determine the effect of temperature on the samples viscosity. Because in honey processing for different reasons (packaging, avoid granulation, destructions of yeast) honey is heated at different temperatures, the rheological study was done for heated and unheated honey samples. In order to verify if Romanian honey presents or not thixotropy, steady shear rheology of each sample was carried out using hysteresis loop tests. Thixotropic behaviour was observed especially for honey not thermally processed. This thixotropic behaviour diminishes after preheating the honey. Cluster analysis was applied in order to demonstrate the possibility of honey classification from its thixotropic behaviour point of view.

Key words: Romanian honey, rheology, Arrhenius model, activation energy, thixotropy

1. Introduction

Bee honey is a natural product with a high nutritional value used in food and medicine for its prophylactic value and antibacterial properties, especially in burn treatment [1]. Viscosity is considered one of the most important physical properties of honey, being very important for all the processing operations. It depends on several factors, the more important of which being water content, temperature and chemical composition, as well as the presence of crystals and colloids in the product. Most honey varieties are characterized as having Newtonian behaviour for a large temperature spectrum [2, 3]. However, there are some reports in the literature, for non-Newtonian behaviour, especially for crystallized honey [4-7].

Romanian honey wasn't yet rheological characterized. The physico-chemical properties like moisture, colour, sugar content, total flavonoids, antioxidant activity and nutraceutical properties of some Romanian honey varieties were already reported [8-11].

The aim of this paper is to present rheological behaviour of Romanian selected honey and to demonstrate that thixotropic behaviour can be observed especially for honey not thermally processed and with high glucose content. This thixotropic

behaviour diminishes after preheating the honey and can even disappear at temperatures higher than 45°C. Cluster analysis was also used in order to classify honey according to its thixotropic behaviour.

2. **Experimental**

Materials
Several types of Romanian honey were studied, namely acacia honey (*Robinia pseudoacacia*) (S1-S4), lime honey (*Tilia sp.*) (T1-T2), coriander honey (*Coriandrum sativum*) (C1-C2), peppermint honey (*Menta Piperita*) (PM), rape honey (*Brassica napus ssp. oleifera*) (R1-R2), sun-flowers honey (*Helianthus annuus*) (SF), polyflower honey (P) and honeydew (mountain multi-flora) (M). The samples were either liquid or crystallized. Those which were crystallized were used after preheating. The liquid samples were divided into two parts: one was rheologically tested in its raw state (unheated) and the other was analysed after the heating process, in order to compare the results. The samples were obtained directly from local stores of the beekeepers. The samples were from 2013-2014 production and were stored at 10 ºC in dark conditions during the experimental period.

Heat treatment
All the samples which were thermally processed, even they were liquid or crystallized ones, were heated at 50 ºC for 1 h in a water bath in order to dissolve crystals, and then kept in a 25 ºC room temperature for 48 h to remove air bubbles from preheated honey samples [12]. For liquid samples, humidity was measured before and after preheating, while for the crystallized samples it was measured only after preheating.

Water content
Water content of the samples was measured with a digital ABBE refractometer. For the samples which were in liquid state, the viscosity was measured initially at the original moisture content, both for unheated and heated honey. For crystallized honey, the viscosity was measured after preheating, when the samples was liquid state. The refractive index values were converted to moisture contents using equation 1:

$$w\% = 608.277 - 395.743 \cdot n_D \tag{1}$$

where w% is the percentage of water content and n_D is the refractive index of honey at 20 ºC [13].

Rheological properties
The rheological testing of honey samples was conducted on a BOHLIN CVO 100 Rheometer, (Bohlin Instruments, Gloucestershire, UK), with a geometry of parallel plates PP20 (20 mm diameter) and with a 0.150 mm gap in all

experiments. Temperature was controlled by a Peltier element. The temperature range was selected from 20 to 50 °C. Steady shear rheology of each sample was carried out using hysteresis loop tests at shear rate range of 0.1–1000 s^{-1} by two cycles, increasing and decreasing the values of shear rate, in order to investigate the thixotropic behaviour of the samples. Each time, a new sample was used for rheological measurement. All rheological measurements were carried out in duplicate. Hysteresis area between instantaneous viscosity and shear rate was calculated using Bohlin Software CVO100 for thixotropic analysis. Because there are high differences between thixotropic areas of different studied samples, a relative thixotropic area was used in order to compare thixotropic behaviour of the investigated samples. This relative thixotropic area was calculated with formula 2:

$$S_R(\%) = 100 \cdot \frac{S_{th}}{S_{up}} \tag{2}$$

where S_{th} is the thixotropic area and S_{up} is the area enclosed by up curve in the shear rate range considered [14].

Statistical analysis

In order to distinguish between different classes of unifloral honeys, various authors have used statistical techniques like: principal component analyses (PCA), discriminant analysis (DA), cluster analysis and other techniques [3, 11, 15-17]. Cluster analysis, which is an exploratory data analysis, seeks to group objects of similar kinds into respective categories. The different objects are sorted in such a way that the degree of association between two objects is maximal if they belong to the same group and minimal otherwise. This technique was applied in this paper for heated and unheated samples of honey using the thixotropic relative area at different temperatures as a dependent variable. Cluster analysis was performed with STATISTICA 10 (Trail version) from StatSoft Inc. applying the joining or tree cluster method, using Euclidean distances as a taxonometric measure.

3. **Results and discussions**

The flow behaviour of many sorts of honey can be well described by the Newtonian law of viscosity. Steady shear rheological data obtained from the studied honey samples were fitted to the Newtonian model for unheated and heated honey samples. The viscosity coefficient was estimated by employing linear regression of shear stress / shear-rate data. The Arrhenius model was used to determine the effect of temperature on the viscosity of the samples:

$$\mu = \mu_0 \cdot \exp\left(E_a / R_g T\right) \tag{3}$$

where μ is the viscosity of the sample (Pa.s), μ_0 is a constant (Pa.s), E_a is the activation energy (J/mol), R_g is gas constant (8.314 J/mol.K) and T is temperature (K). The values obtained for moisture content (w), activation energy (E_a), constant

of the Arrhenius equation (μ_0) and viscosity at 20ºC for the unheated samples are presented in Table 1, while those for preheated samples are presented in Table 2.

Table 1

Moisture content, activation energy (E_a), constant of the Arrhenius equation (μ_0) and viscosity at 20ºC for the unheated honey samples*

| Sample designation	Moisture content w (g/100g)	η (Pa.s) at 20°C	E_a (kJ/mol)	μ_0 (Pa.s)	R^2
S1	15.7 ± 0.03	33.9±0.05	90.87	2.14E-15	1
S2	16.4 ± 0.01	31.6±0.09	79.43	2.18E-13	0.994
S3	16.3 ± 0.05	30.0±0.47	85.82	1.34E-14	0.994
S4	16.5 ± 0.04	27.0±0.14	79.61	1.59E-13	0.997
T1	15.4 ± 0.08	35.0±0.08	92.06	1.30E-15	0.999
C1	18.4 ± 0.04	14.3±0.14	67.70	1.44E-11	0.968
PF	16.3 ± 0.03	22.0±0.12	82.96	5.93E-14	0.968
PM	17.6 ± 0.08	20.1±0.03	68.63	1.45E-11	0.956
R1	17.8 ± 0.21	22.1±0.22	66.24	4.04E-11	0.970
M	17.4 ± 0.09	20.1±0.05	71.52	3.07E-12	0.986
SF	16.9 ± 0.04	24.4±0.41	76.04	8.64E-13	0.998

* All the samples were fluid

Table 2

Moisture content, activation energy (E_a), constant of the Arrhenius equation (μ_0) and viscosity at 20ºC for the preheated honey samples

Sample designation	Moisture content w (g/100g)	η (Pa.s) at 20°C	E_a (kJ/mol)	μ_0 (Pa.s)	R^2
S1	15.7 ± 0.03	34.0±0.07	89.90	3.834E-15	0.991
S2	16.4 ± 0.01	28.0±0.02	79.56	1.870E-13	0.998
S3	16.3 ± 0.05	27.6±0.04	82.31	5.308E-14	0.996
S4	16.5 ± 0.04	25.0±0.10	78.86	2.013E-13	0.997
T1	15.4 ± 0.08	36.0±0.05	90.60	2.422E-15	0.999
T2*	16.7 ± 0.21	25.2±0.17	76.54	5.711E-13	0.998
T3*	16.9 ± 0.17	16.5±0.08	75.44	5.749E-12	0.997
C1	18.4 ± 0.04	14.1±0.07	62.73	1.046E-10	0.980
C2*	16.5 ± 0.17	24.8±0.30	77.30	4.579E-13	0.991
PF	16.3 ± 0.03	30.3±0.11	78.30	4.007E-13	0.975
PM	17.6 ± 0.08	22.0±0.02	67.53	2.452E-11	0.968
R1	17.8 ± 0.21	24.0±0.07	65.48	5.218E-11	0.995
R2*	18.2 ± 0.38	8.1±0.04	70.78	2.062E-12	0.998
M	17.4 ± 0.09	19.3±0.16	67.99	1.266E-11	0.980
SF	16.9 ± 0.04	22.4±0.12	73.10	2.213E-12	0.980

* Samples initially crystallized

In order to appreciate qualitatively the existence of thixotropy, in Figs. 1 and 2 there are presented flow curves for different types of heated or unheated honey samples. In Fig. 1a there are presented flow curves for acacia honey only at two temperatures, 30 and 45 °C, before and after heating. It is obvious that this type of honey has not a thixotropic behaviour. The same assumptions are valid also for coriander honey (Fig. 1b).
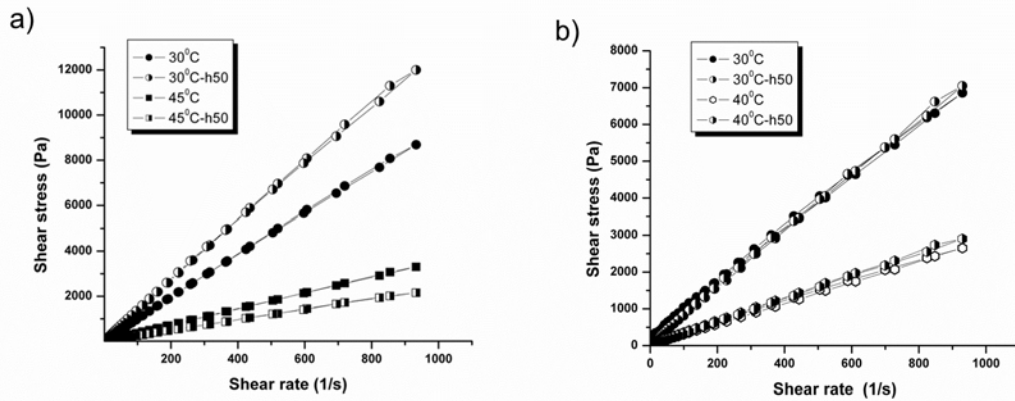
Fig. 1. Flow curves for heated and unheated acacia honey a) and b) coriander honey
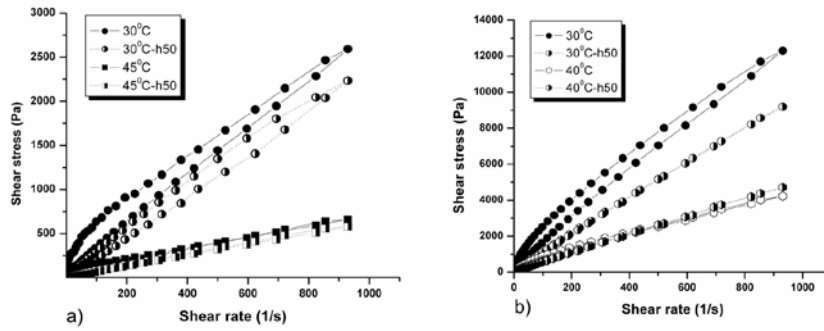
F**ig. 2.** Flow curves for heated and unheated: a) peppermint honey samples (PM) and b) oil seed rape honey (R1)

For peppermint honey and oil seed rape honey, the flow curves presented in Fig. 2a and 2b, respectively, present at low temperatures a thixotropic behaviour which is attenuated and even disappears at high temperatures. Analysis of samples thixotropic behaviour was done using relative thixotropic area calculated with

equation 2. The obtained data for three temperatures 30, 40 and 45ºC are presented in Table 3.

Thixotropic relative aria for three temperatures, for all honey samples

Sample name	Thermal processing	Thixotropic relative area		
		30°C	40°C	45°C
S1	Unheated	0.90	1.29	2.44
S2		1.05	2.51	2.13
S3		0.54	0.82	0.30
S4		0.68	0.83	1.34
T1		0.30	0.15	0.28
C1		1.92	2.26	2.50
PF		6.96	6.69	4.29
PM		11.08	6.76	5.29
R1		9.54	4.99	2.93
M		0.69	0.60	0.43
SF		11.78	7.70	4.92
S1	Heated	0.17	0.27	0.21
S2		1.54	1.73	1.93
S3		1.38	0.66	0.81
S4		0.42	1.26	1.45
T1		0.65	2.74	3.02
T2		2.51	3.15	2.58
T3		2.63	2.55	1.90
C1		1.96	0.88	1.04
C2		2.86	4.58	5.94
PF		1.52	0.81	0.35
PM		8.22	0.54	1.18
R1		0.62	0.35	0.73
R2		7.56	5.74	0.86
M		0.33	0.15	0.12
SF		6.24	3.54	3.30

The dendrograms obtained for the heated and unheated honey samples are presented in Fig. 3a and 3b. In Fig. 3a the dendrogram for unheated samples contains two clusters. The first cluster is formed of the samples which present large thixotropic relative area (R1, SF, PM, PF), while the second contains samples which have no thixotropic behaviour, in accordance with data from Table 3 for unheated samples.

Tree diagram from Fig. 3b, for heated samples honey, shows also two distinct groups, but the members are different from the groups of unheated samples. In cluster 1, which contains honey which exhibits thixotropic behaviour, two

samples (R1 and PF) have disappeared and are now classified in the second cluster. This one contains samples which have no thixotropic behaviour, which is in accordance with the greatest values of thixotropic relative area from Table 3.
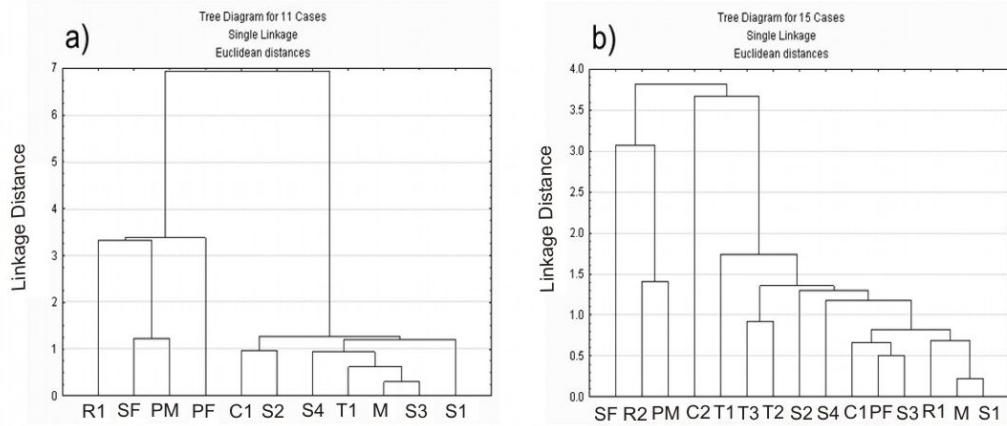
Fig. 3. Cluster tree for: a) unheated honey samples and b) heated honey samples.

So, from this simple cluster analysis, one can confirm that thixotropic behaviour is more pronounced for unheated honey and diminishes or even disappears after heating the samples. Knowing that we have two clusters in both cases (heated and unheated honey samples), K-means clustering method was also applied for heated and unheated honey using STATISTICA 10 (Trial version) from StatSoft Inc. The results containing cluster number, members of each cluster and distances from each cluster centres are presented in Table 4.

Table 4

Statistic data of cluster analysis

Unheated honey			Heated honey		
Cluster number	Members	Distances	Cluster number	Members	Distances
1	PF	1.664	1	C2	2.644
	PM	0.909		PM	1.492
	R1	1.226		R2	1.519
	SF	1.349		SF	0.672
2	S1	0.634	2	S1	1.066
	S2	0.883		S2	0.470
	S3	0.675		S3	0.477
	S4	0.242		S4	0.487
	T1	0.928		T1	1.338
	C1	1.086		T2	1.484
	M	0.6412		T3	1.121
				C1	0.504
				PF	0.634
				R1	0.740
				M	1.093

The honey samples which exhibit thixotropic behaviour are not from honey varieties which are considered superior honey, like acacia, lime or coriander honey and which maintain their liquid aspect for long periods of time.

The others, like peppermint honey (PM), rape honey ((R1-R2) and sun-flowers honey (SF) can crystallize very easily, because of the large amount of glucose in their composition. As it is already known, the honey glucose content is the main cause for honey crystallization. If the ratio F/G (fructose/glucose) is less than 1.11, honey crystallizes quickly [6]. From honey composition reported for Romania and other European countries, some available data are presented as examples. For acacia honey, the ratio between fructose and glucose varies from 1.335 to 1.646. For lime honey, the same ratio varies in the range 1.06 to 1.250 [9, 18]. So, these sorts of honey in which fructose exceeds glucose in the sugar composition don't crystallize fast and for the investigated Romanian samples we didn't observe thixotropic behaviour. The others, which form the second group, are honey samples in which the glucose content is comparable or even larger than the fructose content, which means that they can crystallize very fast. Reported data for sunflower honey reveals ratio between F/G of 1.09 and 1.11, and for rape honey between 0.95 and 1.047 [6, 9, 18]. So, even in liquid state, it is still possible that these types of honey have very small crystals which can contribute to the thixotropic rheological behaviour. Our optical observations of acacia honey versus rape and peppermint honey support these assumptions (images not presented).

These results are in agreement with those obtained by Smanalieva and Senge (2009) for rape and sunflower honey [6]. The aforementioned authors have studied crystallized honey and in this case they have observed non-Newtonian behaviour of all investigated unifloral honey.

4. **Conclusions**

The rheological properties of eight sorts of Romanian honey were analysed using heated and unheated samples. The Newtonian model describes well the flow behaviour of studied samples. The Arrhenius model was used to determine activation energy for the studied samples. Our research showed that the unheated honey with high glucose content exhibits thixotropic behaviour. When honey is heated this behaviour diminishes and even disappear. Cluster analysis allows us to classify honey depending of its thixotropic behaviour.

REFERENCES

[1] Visavadia B.G., Honeysett J., Danford M.H., Manuka honey dressing: An effective treatment for chronic wound infections. *British Journal of Oral and Maxillofacial Surgery,* 46, (2008), 55−56.

[2] Juszczak L., Fortuna T., Rheology of selected Polish honeys, *Journal of Food Engineering,* 75, (2006), 43–49.

[3] Wei Z., Wang J., Wang Y., Classification of monofloral honeys from different floral origins and geographical origins based on rheometer. *Journal of Food Engineering*, 96, (2010), 469–479.

[4] Bhandari, B., D'Arcy, B., Kelly, C., Rheology and crystallization kinetics of honey: Present status. *International Journal of Food Properties,* 2, (1999), 217–226.

[5] Gómez-Díaz, D., Navaza, J. M., Quintáns-Riveiro L.C., Rheological behaviour of Galician honeys. *European Food Research Technology,* 222, (2006), 439–442.

[6] Smanalieva, J., Senge, B., Analytical and rheological investigations into selected unifloral German honey. *European Food Research Technology*, 229, (2009), 107–113.

[7] Witczak, M., Juszczak, C., Gatłkowska, D., Non-Newtonian behaviour of heather honey. *Journal of Food Engineering,* 104, (2011), 532–537.

[8] Dobrinas, S., Birghila, S., Coatu, V., Assessment of polycyclic aromatic hydrocarbons in honey and propolis produced from various flowering trees and plants in Romania. *Journal of Food Composition and Analysis*, 21, (2008), 71–77.

[9] Mǎrghitas L. Al., Dezmirean D., Moise A., Bobis O., Laslo L., Bogdanov S., Physico-chemical and bioactive properties of different floral origin honeys from Romania. *Food Chemistry*, 112, (2009), 863–867.

[10] Moise A., Mǎrghitas Al. L., Dezmirean D., Bobis O., Nutraceutical properties of Romanian heather honey, *Nutrition&Food Science*, 43, (2013), 218-227.

[11] Isopescu R. D., Josceanu A. M., Minca I., Colta T., Postelnicescu P., Mateescu C., Characterization of Romanian Honey Based on Physico-Chemical Properties and Multivariate Analysis, *Rev. Chim. (Bucharest)*, 65, (2014), 381-385.

[12] Yoo, B. Effect of temperature on dynamic rheology of Korean honeys. *Journal of Food Engineering*, 65, (2004). 459–463.

[13] Abu-Jdayil, B., Al-Majeed Ghzawi, A., Al-Malah, K.I.M., Zaitoun, S., Heat effect on rheology of light and dark-colored honey. *Journal of Food Engineering*, 51, (2002), 33–38.

[14] Dolz, M., Hernandez, M. J., Delegido, J., Alfaro, M. C., Muñoz. J., Influence of xanthan gum and locust bean gum upon flow and thixotropic behaviour of food emulsions containing modified starch. *Journal of Food Engineering*, 81, (2007), 179–186.

[15] Terrab, A., González, A. G., Díez, M. J., Heredia, F.J., Characterisation of Moroccan unifloral honeys using multivariate analysis. *European Food Research Technology*, 218, (2003) 88–95.

[16] Serrano, S, Villarejo, M., Espejo, R., Jodral, M., Chemical and physical parameters of Andalusian honey: classification of Citrus and Eucalyptus honeys by discriminant analysis. *Food Chemistry*, 87, (2004), 619–625.

[17] G. A. Nayik, V. Nanda Physico-Chemical, Enzymatic, Mineral and Colour Characterization of Three Different, Varieties of Honeys from Kashmir Valley of India with a Multivariate Approach, *Polish Journal of Food and Nutrition Science*, 65, (2015), 101–108

[18] Kaspar, R.. *Authentication of the botanical origin of honey*. Dissertation, (2006), ETH Zurich.

CATIONIC SURFACTANT SOLUTIONS: RHEOLOGY AND CHARACTERIZATION OF THE CIRCULAR FLOW THROUGH RING-SHAPED SECTIONS

Andra TĂMAŞ[1]*, Mirabela PĂDURE[1], Martin VINCZE[2]

[1]University Politehnica of Timişoara, Faculty of Industrial Chemistry and Environmental Engineering, Bld. Vasile Pârvan 6, 300223, Timişoara

[2]Mopeka Impex SRL, Timişoara

Abstract
The paper presents the rheological behavior study of some cationic surfactant-based aqueous solutions with organic/inorganic salt content that can be used as fracturing fluids. The influence of salt type and concentration was determined, as well as the temperature, on the rheological behavior. It was also characterized the solutions flow through the ring-shaped space of a rotating viscometer Rheotest-2 and it was appreciated the hydrodynamic regime from the values of the Taylor-Reynolds number.

Key words: Apparent viscosity, circular motion, dynamic pressure, Taylor-Reynolds number

1. Introduction

Hydraulic fracturing is a well stimulation process used to maximize the extraction of underground resources. It refers to the procedure of creating fractures in rocks and rock formations by injecting a fracturing fluid into the cracks to force underground to open further. The main functions of a fracturing fluid are to open the fracture and to transport propping agent along the length of the fracture [1, 2].

A fracturing gel should provide sufficient viscosity to suspend and transport the proppant (sand, bauxite or ceramic) into the fracture, and should break into a low-viscosity fluid after the fracturing is completed [3]. Viscoelastic surfactant (VES) fluid has been used as a clean fluid for frac-packing and conventional hydraulic fracturing. Surfactant-based fracturing gels are considered as clean gels due to the absence of insoluble residues in their composition and can be broken when exposed to hydrocarbons or formation water. Therefore,

---

*Corresponding author; Email address: andra.tamas@upt.ro (Andra Tămaş)

conventional breakers are not required, and the oil or gas produced can act as breakers for surfactant-based gels [4].

The unique rheological properties of viscoelastic wormlike micelle solutions have led to their broad use as rheological modifiers in consumer products (paints, detergents, lubricants, emulsifiers), in turbulent drag reduction and to enhance oil recovery and improve drilling.

In solution, at low concentrations, surfactant molecules self-assemble to form aggregates that are generally globular micelles. These micelles can grow upon an increase of surfactant concentration and/or upon addition of salts, alcohols, etc. The size, shape and aggregation geometry of these aggregates can be modified by external influences such temperature, pressure and flow. Most solutions of wormlike micelles display rheological properties in which the response to mechanical perturbation involves both elastic deformation and viscous flow [5-12].

The temperature increase leads to microdrops mobility intensification which influences the activation energy (E_a) of the system, phenomenon that can be explained by an Arrhenius type equation applied in relation to shear stress [13]:

$$\tau = A^{'} \cdot e^{\frac{E_a}{R \cdot T}}$$

(1)

The characterization of liquids flow in ring-shaped spaces and the establishing of the hydrodynamic regime type can be expressed using Taylor-Ta (ec.2) and Taylor-Reynolds-Ta_{Re} (ec.3) numbers which depend on the geometry of the annulus of the drum viscometer (the radii of the outer r_o and inner r_i cylinder, their difference δ), by the inner cylinder revolution (n) or angular velocity (Ω) and the fluid properties (density ρ, dynamic η or kinematic υ viscosity):

$$Ta = \mathrm{Re}^2 \cdot \frac{\delta}{r} = \frac{\Omega^2 \cdot r_i \cdot \delta^3}{\nu^2} = \frac{4 \cdot \pi^2 \cdot n^2 \cdot r_i \cdot \delta^3 \cdot \rho^2}{\eta^2}$$

(2)

$$Ta_{\mathrm{Re}} = \frac{\Omega \cdot r_i \cdot (r_o - r_i)}{\nu} = \frac{2 \cdot \pi \cdot n \cdot r_i \cdot \delta \cdot \rho}{\eta}$$

(3)

The submitted relations are specific to Taylor-Couette flow, including the movement of fluid through the ring-shaped space of the viscometer used. The critical regime for Taylor number is considered $Ta_{cr}=1700$, and for Taylor-Reynolds number $Ta_{Re,cr}=60$. By overcoming the critical regime, in liquid are formed toroidal or spiral vortices which increase with the increasing of turbulence, phenomenon called "instability of Taylor-Couette flow"[14,15]. The formation of these vortices is explained by the increase of the dynamic pressure of the fluid (P_{dyn}) which can be much higher than the shear stress of the layers (τ), moment when micelles breaking occur.

2. Experimental

Reagents

The cationic surfactant used for the solutions preparation contains hexadecyltrimethylammonium chloride $(C_{16}H_{33}N^+(CH_3)_3]Cl^-)$ (properties presented in Table 1) with an active substance content of 30%. The organic salts are sodium or potassium salicylate (NaSal/KSal) and the inorganic salts are NaCl or KCl.

Methods

The samples preparation was done at room temperature (25°C), by dispersing the cationic surfactant in the aqueous solution containing organic and/or inorganic salts. The compositions of the tested samples are presented in Table 2. It was used a stirrer with diameter 45 mm which provides an intense stirring (Re=5×10^4) corresponding to a peripheral velocity of 3.5 m s^{-1}.

Table 1

The properties of cationic surfactant

Property	Conditions of admissibility/Value
Molecular weight, g mol^{-1}	319.5
Critical micellar concentration CMC (20°C), mmol L^{-1}	0.185
pH of aq. sol. 1%	$6.5 \div 8$
Solubility in water	Completely soluble
Density (25°C), kg m^{-3}	1000
Dynamic viscosity (25°C), mPa s	10.1

Table 2

The composition of the samples

Sample	Composition, wt.%					
	Surfactant	NaSal	KSal	NaCl	KCl	Water
B$_2$		2	-	-	-	93
B$_3$		3	-	-	-	92
B$_4$		4	-	-	-	91
B$_5$		5	-	-	-	90
C$_3$		-	3	-	-	92
C$_4$		-	4	-	-	91
C$_5$	5	-	5	-	-	90
B$_{51}$		1	-	4	-	90
B$_{52}$		2	-	3	-	90
B$_{54}$		4	-	1	-	90
C$_{51}$		-	1	-	4	90
C$_{52}$		-	2	-	3	90
C$_{54}$		-	4	-	1	90

The rheological characterization of the samples was carried out under thermostatic conditions (temperature range 25÷45ºC), using a rotational

viscometer Rheotest-2 with the system vat-drum S/S_1. The device allows the measurement of the torsion moment appeared thanks to the ring-shaped substance layer placed between a fixed cylinder and a rotating one with known revolution. The torsion moment is correlated with the shear stress τ. The revolution and the ring-shaped layer thickness determine the shear rate $\dot{\gamma}$. Shear rate values were changed in the range $9 \div 729$ s^{-1}. For the system vat-drum S/S_1 the geometrical dimensions are r_o=20.1 mm and r_i=19.6 mm. The samples were analysed after one day of preparation.

3. Results and discussions

The influence of temperature on the rheological behaviour was determined for all the samples. In Fig. 1 dependence $\tau = f(\dot{\gamma})$ is shown, at three temperature values, for solution B_5 (5% NaSal) and C_5 (5% KSal).
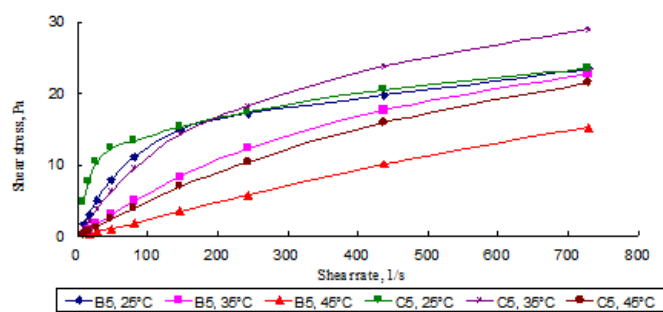

Fig. 1. Shear stress *vs.* shear rate for samples B_5 and C_5

The obtained curves $\tau = f(\dot{\gamma})$ are nonlinear indicating a non-Newtonian behaviour, except the sample B_5 at 45°C whose behaviour is Newtonian. The aqueous surfactant solution presents Newtonian behaviour, too. It is also noted that there is a point of inflection of $\tau = f(\dot{\gamma})$ curves, the more noticeable the lower the temperature is. For this reason, the rheological equations have been established on different ranges of shear rate, thus determining the shear rate value at which the inflection takes place (the value of transition $\dot{\gamma}_{ch}$) and are presented in Table 3.

It is noted that the shear stress values, at the same shear rate, are higher for the samples with potassium salicylate content.

From the graphical representation of apparent viscosity (calculated as the ratio between the shear stress and the shear rate) evolution as a function of shear rate for samples B_2 and B_4 (Fig. 2), with some of the results detailed in Table 4 for several samples, it is observed that: (1) apparent viscosity decreases with the increasing of the concentration of sodium salicylate; (2) the same decreasing

effect also appears when the shear rate increases above a certain value ($\log \dot\gamma > 1.91$, $\dot\gamma > 81 \, s^{-1}$); (3) apparent viscosity increases with increasing the concentration of sodium chloride; (4) the change of apparent viscosity is more noticeable at lower temperatures, remaining almost constant at 45°C.

Rheological equations for samples B$_5$ and C$_5$

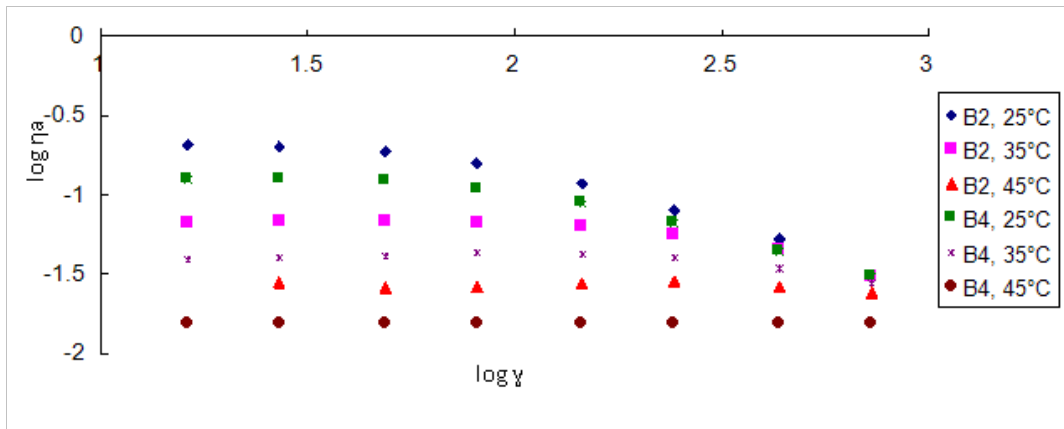| Sample	Temp., °C	Eq. $\tau = K \cdot \dot\gamma^n$	R^{2*}	$\dot\gamma_{ch}$, s^{-1}
B$_5$	25	$\tau = 0.534 \cdot \dot\gamma^{0.675}$, $\dot\gamma \in (9 \div 145.8) s^{-1}$	0.9849	119.6
		$\tau = 3.38 \cdot \dot\gamma^{0.289}$, $\dot\gamma \in (81 \div 729) s^{-1}$	0.9756	
	35	$\tau = 0.049 \cdot \dot\gamma^{1.042}$, $\dot\gamma \in (16.2 \div 145.8) s^{-1}$	0.9921	108.5
		$\tau = 0.25 \cdot \dot\gamma^{0.696}$, $\dot\gamma \in (81 \div 729) s^{-1}$	0.9788	
	45	$\tau = 0.0214 \cdot \dot\gamma$, $\dot\gamma \in (16.2 \div 729) s^{-1}$	0.9955	-
C$_5$	25	$\tau = 2.35 \cdot \dot\gamma^{0.4}$, $\dot\gamma \in (9 \div 145.8) s^{-1}$	0.8863	65.9
		$\tau = 4.22 \cdot \dot\gamma^{0.26}$, $\dot\gamma \in (81 \div 729) s^{-1}$	0.9987	
	35	$\tau = 0.2 \cdot \dot\gamma^{0.868}$, $\dot\gamma \in (16.2 \div 145.8) s^{-1}$	0.9852	104.3
		$\tau = 1.12 \cdot \dot\gamma^{0.5}$, $\dot\gamma \in (81 \div 729) s^{-1}$	0.9867	
	45	$\tau = 0.029 \cdot \dot\gamma^{1.11}$, $\dot\gamma \in (16.2 \div 145.8) s^{-1}$	0.989	104.0
		$\tau = 0.14 \cdot \dot\gamma^{0.774}$, $\dot\gamma \in (81 \div 729) s^{-1}$	0.9859	

*the correlation coefficient

Fig.2. $\log \eta_a$ *vs.* $\log \dot\gamma$ for samples B$_2$ and B$_4$

Apparent viscosity of certain samples

Sample	Apparent viscosity, mPa.s	
	25°C	35°C
B3	116	60
B5	114	55.6
C5	130	107
B52	144	79
B54	123	58

The apparent viscosity of the samples containing potassium salicylate is higher than of the samples with sodium salicylate content and also decreases more at values $\dot{\gamma} > 81 s^{-1}$ (Fig. 3).

In addition, it is observed that the apparent viscosity of these solutions increases with the increasing percentage of the potassium salt, in accordance with the equations presented in Table 5, ($\dot{\gamma} \in (27 \div 729)$ s^{-1}).
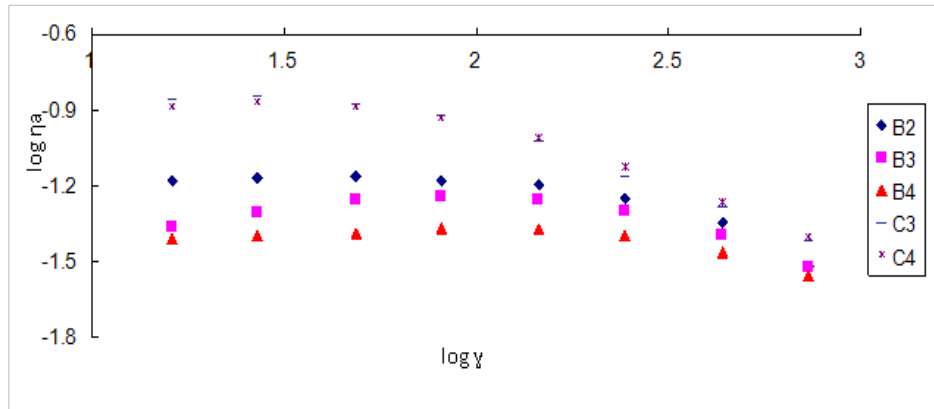
Fig.3. $\log \eta_a$ *vs.* $\log \dot{\gamma}$ for samples B$_2$, B$_3$, B$_4$, C$_3$ and C$_4$ at 35°C

Rheological equations for samples B$_2$, B$_3$, B$_4$, C$_3$, C$_4$ and C5 at 35°C

Sample	Eq. $\tau = K \cdot \dot{\gamma}^n$	R^2
B$_2$	$\tau = 0.307 \cdot \dot{\gamma}^{0.674}$	0.9867
B$_3$	$\tau = 0.251 \cdot \dot{\gamma}^{0.686}$	0.9829
B$_4$	$\tau = 0.135 \cdot \dot{\gamma}^{0.765}$	0.9921
C$_3$	$\tau = 1.395 \cdot \dot{\gamma}^{0.39}$	0.9625
C$_4$	$\tau = 0.555 \cdot \dot{\gamma}^{0.625}$	0.9659
C$_5$	$\tau = 0.454 \cdot \dot{\gamma}^{0.67}$	0.9595

The rheological behaviour of samples with potassium salicylate and potassium chloride content is still non-Newtonian even at 45°C, similar with the samples without potassium chloride. With the increasing of the concentration of potassium chloride it is also more highlighted the inflection point of $\tau = f(\dot{\gamma})$ curves, Fig. 4. The apparent viscosity of the solutions increases with the increasing of potassium chloride percentage in the composition. In comparison, at the same temperature, the samples containing sodium salicylate and sodium chloride present Newtonian behaviour, and the dynamic viscosity increases with the increase of the percentage of NaCl (Fig. 5).

The study of the influence of temperature on the flow activation energy of the system was done for the samples with different sodium salicylate concentrations (B_3, B_5).

Dependence $\ln \tau = f(1/T)$ was graphically represented, as obtained from the logarithmic form of equation (1), for shear stress values corresponding to the three chosen values of the shear rate. Particular expressions of eq. (1) for these solutions and the values of E_a and Ta_{Re} number are presented in Table 6.
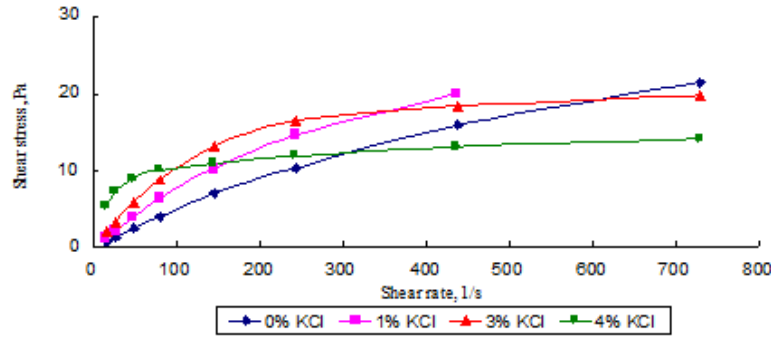

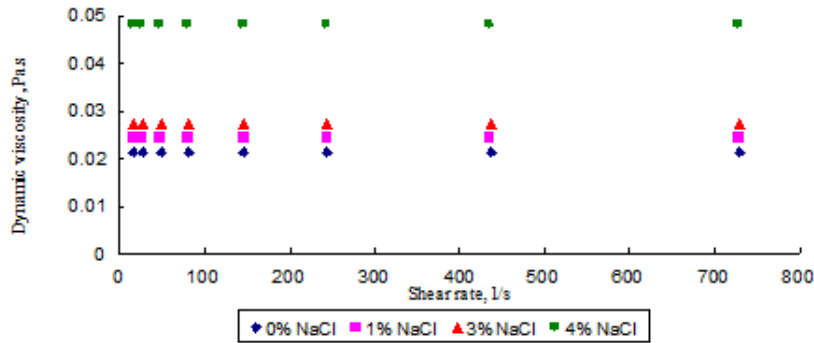**Fig. 4**. Shear stress *vs.* shear rate for samples C_5, C_{51}, C_{52}, and C_{54}

Fig. 5. Dynamic viscosity *vs.* shear rate for samples B_5, B_{51}, B_{52} and B_{54}

Table 6

Particular expressions of eq.(1) for samples B$_3$, B$_5$

$\dot{\gamma}$ / s^{-1}	Eq. $\tau = A^{'} \cdot \exp(E_a / R \cdot T)$		Ta$_{Re}$	
	3% NaSal	5% NaSal	3% NaSal	5% NaSal
27	$\tau = 2.4 \cdot 10^{-13} \cdot \exp(9100/T)$ 75.6 kJ/mol	$\tau = 1.3 \cdot 10^{-13} \cdot \exp(9300/T)$ 77.4 kJ/mol	0.028	0.031
81	$\tau = 7.3 \cdot 10^{-12} \cdot \exp(8400/T)$ 69.5 kJ/mol	$\tau = 2.6 \cdot 10^{-12} \cdot \exp(8700/T)$ 72.1 kJ/mol	0.12	0.135
243	$\tau = 4 \cdot 10^{-7} \cdot \exp(5200/T)$ 43.5 kJ/mol	$\tau = 1.1 \cdot 10^{-7} \cdot \exp(5700/T)$ 47.0 kJ/mol	0.67	0.68
729	$\tau = 2.7 \cdot 10^{-2} \cdot \exp(2020/T)$ 16.8 kJ/mol	$\tau = 6.6 \cdot 10^{-3} \cdot \exp(2460/T)$ 20.4 kJ/mol	4.1	4.3

It is noted that the values of the activation energy of viscous flow increase slightly lower with sodium salicylate content and decrease more pronounced with shear rate increasing.

The study of fluids flow through ring-shaped space was performed for solutions with different apparent viscosities, at 25°C when they present non-Newtonian behaviour, at the transition value of the shear rate analytically determined for each curve $\tau = f(\dot{\gamma})$ (some values are given in Table 3). Using the revolution of the inner cylinder it was calculated the dynamic pressure of the liquid, considering the average speed of layers ($w_{med} = 0.5 \cdot w_{max}$), according to relation (4):

$$P_{dyn} = \frac{\rho \cdot w_{med}^2}{2} \tag{4}$$

The ratio of shear stress and dynamic pressure τ_f / P_{dyn} [16, 17] is a direct measure of the increase of centrifugal or inertial forces in correlation with the viscous friction force, depending on the Taylor-Reynolds number Ta$_{Re}$.

$$\tau / P_{dyn} = f(Ta_{Re}) \tag{5a}$$

$$\ln(\tau / P_{dyn}) = a \cdot \ln Ta_{Re} + b \tag{5b}$$

$$\ln(\tau / P_{dyn}) = b^{*} - \ln Ta_{Re} \tag{5c}$$

In the graphical representation of relation (5a) the dependence is parabolic and the logarithmic representation of relation (5b) is a right line whose slope tends to the unitary value, the dependence being inverse proportional (Fig. 6).
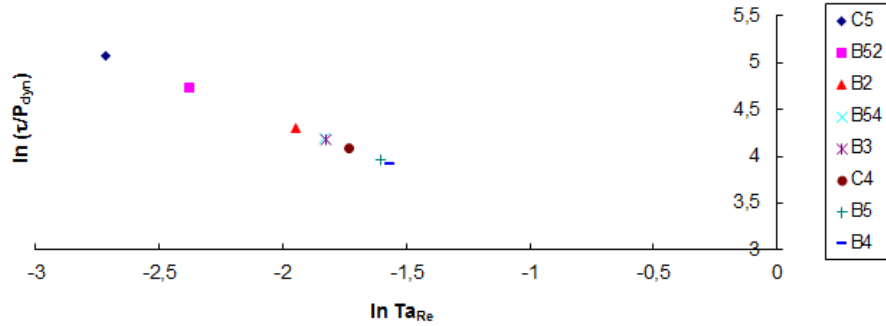
Fig. 6. Dependence $\ln(\tau / p_{dyn}) = f(\ln Ta_{Re})$ for the analyzed samples

Taking into account the condition of equality between shear stress and dynamic pressure ($\tau / P_{din} = 1$ or $\ln(\tau / P_{din}) = 0$) the equilibrium value of Taylor-Reynolds number was determined as $Ta^*_{Re} = 10.54$. This ratio, that can be also deduced through calculation, is smaller than the critical value $Ta_{Re,cr}$ established, based on the observations related to the vortices appearance. In Table 7 were exemplified these calculations for the flow of B_5 solution into the ring-shaped space of a rotational viscometer Rheotest-2.

Table 7

The representative values for the flow of B_5 solution at 25°C

n (s⁻¹)	τ (Pa)	P_{dyn} (Pa)	τ / P_{dyn}	$\ln \tau / P_{dyn}$	Ta_{Re}	$\ln Ta_{Re}$
0.05	3.0	0.0047	638.3	6.459	0.0168	-4.084
0.083	4.9	0.0131	374.0	5.924	0.0280	-3.577
0.15	7.9	0.0426	185.4	5.223	0.0565	-2.874
0.25	11.1	0.1184	93.75	4.540	0.1124	-2.186
0.45	14.9	0.3835	38.80	3.660	0.2700	-1.308
0.75	17.2	1.0653	16.10	2.782	0.6520	-0.428
1.35	19.7	3.45	5.71	1.742	1.846	0.613
2.25	23.4	9.6	2.40	0.891	4.500	1.503

For solutions B_5, C_5, B_{52} and C_{52}, at 25°C, in Table 8 is presented the variation range of the main parameters taken into account, as well as the obtained values for Ta^*_{Re} number.

Table 8

The variation range of measures and the parameters of rel. (5b,c)

Sample	n (s⁻¹)	τ (Pa)	P_{dyn} (Pa)	Ta_{Re}	Rel.5b		Rel.5c	Ta^*_{Re}
					a	b	b*	
B_5	0.05÷2.25	3÷23.4	0.0047÷9.6	0.0168÷4.5	-0.9952	2.367	**2.378**	**10.79**
C_5	0.05÷2.25	7.6÷23.6	0.0047÷9.6	0.0065÷4.3	-1.0003	2.3534	**2.3527**	**10.51**
B_{52}	0.05÷1.35	5÷28.1	0.0047÷3.45	0.0099÷1.3	-1.000	2.3542	**2.3542**	**10.53**
C_{52}	0.009÷0.45	3.8÷12.3	0.00016÷0.38	0.00044÷0.33	-0.9997	2.3551	**2.3558**	**10.55**

It is noted that the equilibrium values Ta_{Re}^{*} obtained for the four samples are in accordance with the value 10.54 graphically determined (Fig. 6).

4. Conclusions

The analyzed samples, regardless of the nature and concentration of added salts, present non-Newtonian behaviour with flow behaviour index smaller than 1 (Table 3) to the entire temperature range studied.

At low temperatures the rheological curves have a point of inflection that characterizes the transition value of the shear rate. For some samples (B_2-B_5, B_{52}, B_{54}) temperature increase leads to the disappearance of the inflection. This phenomenon can be explained by the fact that increasing temperature ensures intensification of the Brownian motion, micelles size decreases and the aggregation number decreases.

On increasing shear rate, the wormlike micelles are linearized and the flow becomes Newtonian. After the stress stopping the solution regains its non-Newtonian behaviour, illustrated by checking the rheological behaviour after certain time intervals. The obtained Ta_{Re}^{*} value indicates that the performed measurements occurred under laminar regime so the change of rheological behaviour type, at values of Ta_{Re} number below the equilibrium value.

REFERENCES

[1] Gulbis J., Hodge R.M., Fracturing Fluid Chemistry and Proppants in Economides M.J., Nolte K.G., Reservoir Stimulation Handbook, John Wiley&Sons, Chicester, 2000.
[2] Bohloli B., de Pater C.J., Experimental study on hydraulic fracturing of soft rocks: Influence of fluid rheology and confining stress, *J.Pet.Sci.Eng.*, 53, (2006), 1-12.
[3] Castro Dantas T.N., Santanna V.C., Dantas Neto A.A., Curbelo F.D.S., Garnica A.I.C., Methodology to break test for surfactant-based fracturing gel, *J. Pet. Sci. Eng.*, 50, (2006), 293-298.
[4] Schramm L.L., Surfactants: Fundamentals and Applications in the Petroleum Industry, 1st ed., Cambridge University Press, 2000.
[5] Rothstein J.P., Strong flows of viscoelastic wormlike micelle solutions, *Rheology Reviews*, (2008), 1-46.
[6] Yesilata B., Clasen C., McKinley G.H., Nonlinear shear and extensional flow dynamics of wormlike surfactant solutions, *J. Non-Newtonian Fluid Mech.*, 133, (2006), 73-90.
[7] Hao L-S., Hu P., Nan Y-Q., Salt effect on the rheological properties of the aqueous mixed cationic and anionic surfactant systems, *Colloids and Surfaces A: Physicochem. Eng. Aspects*, 361(1-3), (2010), 187-195.
[8] Nan Y-Q., He S-Q., Liu M-N., He H-Y., Hao L-S., The influence of inorganic salts on the rheological properties of 1,3-propanediyl bis(dodecyl dimethylammonium bromide) and sodium dodecylsulfonate aqueous mixed system, *Colloids and Surfaces A: Physicochem. Eng. Aspects*, 436, (2013), 158-169.

[9] *Al-Sadat W., Nasser M.S., Chang F., Nasr-El-Din H.A., Hussein I.A.,* Rheology of a viscoelastic zwitterionic surfactant used in acid stimulation: Effects of surfactant and electrolyte concentration, J.Pet.Sci.Eng., 124, (2014), 341-349.

[10] *Oelschlaeger C., Willenbacher N.,* Mixed wormlike micelles of cationic surfactants: Effect of the cosurfactant chain length on the bending elasticity and rheological properties, Colloids and Surfaces A: Physicochem. Eng. Aspects, 406, (2012), 31-37.

[11] *Li H., Chen R., Lu X., Hou W.,* Rheological properties of aqueous solution containing xanthan gum and cationic cellulose JR400, Carbohydr. Polym., 90, (2012), 1330-1336.

[12] *Rojas M.R., Muller A.J., Saez A.E.,* Effect of ionic environment on the rheology of wormlike micelle solutions of mixtures of surfactants with opposite charge, J.Colloid Interface Sci., 342, 1, (2010), 103-109.

[13] *Boran S., Tămaş A.,* Rheological behaviour of some oils additivated with mixed pyromellitic esters, Studia UBB Chemia, LVIII(1), (2013), 21-30.

[14] *Batten W.M.J., Bressloff N.W., Turnock S.R.,* Transition from vortex to wall driven turbulence production in the Taylor-Couette system with a rotating cylinder, Int. J. Numer. Methods Fluids, 38, 3, (2002), 207-226.

[15] *Dou H.S., Khoo B.C., Yeo K.S.,* Instability of Taylor-Couette flow between concentric rotating cylinders, Inter. J. of Therm. Sci., 47, (2008), 1422-1435.

[16] *Borş N., Tămaş A., Minea R.,* Contributions to Rheological Fluids Flow in Modified Couette Device, Revista de Chimie, 61(2), (2010), 218-222.

[17] *Gropşian Z., Tămaş A., Minea R., Borş N.,* Characterization of the circular flow of viscous liquids through ring-shaped spaces, Bulletin of the Romanian Chemical Engineering Society, 1, (2014), 91-98.

ELECTROCHEMICAL TECHNIQUES AS A USEFUL AID FOR DEPOSITION AND CHARACTERISATION OF SILANE COATINGS

Ioana-Alina CIOBOTARU, Danut-Ionel VAIREANU[*], Ioana MAIOR, Anca COJOCARU, Simona CAPRARESCU

University Politehnica of Bucharest, Faculty of Applied Chemistry and Materials Science, Department of Inorganic Chemistry, Physical Chemistry and Electrochemistry, 1-7, Polizu street, Bucharest, 011061, Romania

Abstract
The electrochemical techniques are regarded nowadays as powerful techniques for coatings substrate preparations and also for the characterisation of the deposed layers and may be employed where classical techniques may not be suitable for these purposes. The goal of using electrochemical substrate preparation is related to the enhancement of the corrosion protection performances, particularly of silane coatings. Once deposed, these silane layers may also be characterised using open circuit potential (OCP), electrochemical impedance spectroscopy (EIS), potentiodynamic polarization (PDP). The results are further processed in order to obtain important characteristic parameters, such as coating stability and durability, dielectric properties and corrosion rate.

Key words: silane coatings, corrosion protection, electrochemical impedance spectroscopy

1. Introduction

Silanes have been used recently as adhesion promoters between organic compounds and some metallic substrates due to their effective barrier and adhesion properties [1-4] or as an environmental friendly alternative for the chromate coatings due to corrosion protection properties [1, 3, 5].
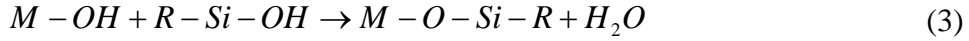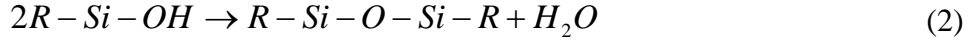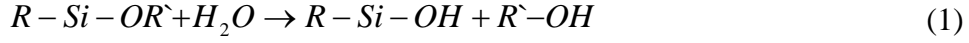
Silane films deposed on metallic substrates confer a physical barrier against a corrosion attack by forming a siloxane network at the surface [4].

Hydrolysis and condensation are the main reactions that occur in the silane solution during preparation and deposition on a metallic substrate [6]. These reactions can occur simultaneously with different reaction rates [6] depending on a series of factors such as pH, silane solution concentration, nature of the organo-functional groups or solution ageing [7].

---

[*] Corresponding author; Email address: di_vaireanu@yahoo.co.uk (D.I. Vaireanu)

The reactions of silanes hydrolysis (1), condensation (2) and deposition on a metallic substrate (3) may be generally described as follows [8, 9]:

$$R - Si - OR` + H_2O \rightarrow R - Si - OH + R`-OH \tag{1}$$

$$2R - Si - OH \rightarrow R - Si - O - Si - R + H_2O \tag{2}$$

$$M - OH + R - Si - OH \rightarrow M - O - Si - R + H_2O \tag{3}$$

Deposition on a metallic substrate must be performed after hydrolysis of the silane solution, when sufficient Si-OH groups are generated in order to react with the metallic substrate [7]. Depending on the operating conditions, once the hydrolysis of the silane begins, a certain fraction of them will condense with each other [10], leading to the formation of a Si-O-Si network [7]:

$$Si - OH + HO - Si \rightarrow Si - O - Si + H_2O \tag{4}$$
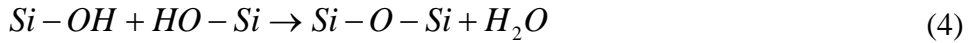
After the deposition of the silane from a diluted silane solution, the film should be subjected to a curing treatment in order to achieve a stable coating and hence an improved corrosion protection [11]. The curing consists usually in a controlled heating treatment leading to crosslinking of the silane molecules and condensation of the silanol groups that have not reacted with the metallic substrate [7, 11].

Electrochemical techniques have been used recently for characterizing some non-conventional protective coatings deposed on metallic substrates [12] and for investigating their behaviour in various corrosive media [1, 7].

Electrochemical impedance spectroscopy (EIS)

One of the most employed techniques for evaluating the performance of the protective coatings is the electrochemical impedance spectroscopy, a non-destructive technique that offers information about the ability of the protective layer to block the ionic conduction to the metallic surfaces and to quantify the corrosion behaviour of the layer by means of the polarization resistance.

Open circuit potential (OCP)

Open circuit potential is the monitoring in time of the sample electrode potential versus the reference electrode in the absence of any current in the electrochemical cell.

The potentiodynamic polarization (PDP)

The potentiodynamic polarization is one of the most employed techniques in corrosion evaluations. This technique helps to determine quantitatively a corrosion rate by measuring the corrosion current density (i_{cor}).

Conductometric (conductivity) and potentiometric (pH) methods

The behaviour of the silane solution during hydrolysis is estimated by monitoring the value of conductivity and pH in time. Conductivity and pH

measurements allow to monitor the evolution of the hydrolysis and condensation reactions as the number and type of the ionic charge carriers vary during this process, and hence, to determine the optimum deposition time [13, 14].

The aim of this study is to characterize some silane solutions used for metallic protective coatings and to investigate their corrosion behaviour using electrochemical techniques such as open circuit potential, electrochemical impedance spectroscopy and potentiodynamic polarization curves.

2. Experimental

Reagents

The silane used as a protective coating is bis-1,2-(triethoxysilyl)ethane (BTSE) purchased from Fluorochem Ltd, Hadfield, U.K . The tested solutions are 2% BTSE and 2% BTSE with the pH adjusted to 11 with a 2mole/L NaOH solution. The solutions were prepared by adding the silane in a 50:50 (v:v) mixture of ethanol and distilled water. The working electrode is a commercially aluminium can polished with emery paper for removing the protective layers, degreased with ethanol, rinsed with distilled water and dip-coated in the silane solution for 10 min.

The deposition of the silane solution on the metallic substrate has been made after the conductivity measurements were performed, in order to establish the optimum deposition time. The coated samples were subjected to different curing treatments consisting in drying them at $110\pm5^{o}C$ for 2 h versus drying at room temperature $(23\pm2^{o}C)$ for 12 h.

The electrolyte solution used for the determination of the corrosion current density was a 3.5% NaCl solution. The NaOH and NaCl solutions were prepared from analytical grade reagents and distilled water.

Apparatus and procedure

The conductivity and pH were monitored continuously for 36 h using a novel three in one closed system conductivity cell based on two parallel stainless steel electrodes, an industrial pH electrode inserted in the cell and a temperature probe for automatic temperature compensation. The data were recorded using a computer controlled data acquisition system, Phywe Cobra 3, at a sampling rate of 3 combined measurements per hour, starting from the preparation of the solution, considered the initial time up to a maximum period of 48 h.

OCP, EIS and PDP measurements were carried out in a 50 mL thermostated three electrode cell connected to a Voltalab 40 potentiostat. One has used a saturated Ag/AgCl electrode (Radiometer Analytical) as reference electrode, a Pt mesh electrode (5 cm^2 area, Radiometer Analytical) as counter-electrode and a working electrode consisting of an aluminium sheet of 1 cm^2 active area subjected to the silanization process.

The OCP was measured for 10 min. using an acquisition frequency of 10 measurements / min. The EIS measurements were conducted by applying a sinusoidal potential perturbation of 10 mV and scanning a frequency range between 100 kHz and 100 mHz carrying out 10 measurements per decade. The PDP was operated in a potential window between -1000mV and 1000mV, at a scan rate of 2 mV/s.

3. Results and discussions

Conductivity and pH
Fig. 1 shows the variation of the conductivity of a 2% BTSE solution in time. One may see an increase of the conductivity values in the first 300 min., a range of maximum values registered after 300-380 min., followed by a slow decrease. This is a confirmation that the hydrolysis of the silane actually occurs, the conductivity value increase with the increase number of charge carriers in solution, the maximum peak located at about 360 min. starting from the preparation of the solution corresponding to a maximum point of the hydrolysis of the silane solution, considered as the optimum time for initiating the deposition on the aluminium substrate. After this point, the value of the conductivity decreases due to the condensation process, the equilibrium being obtained after a period of 1200 min.
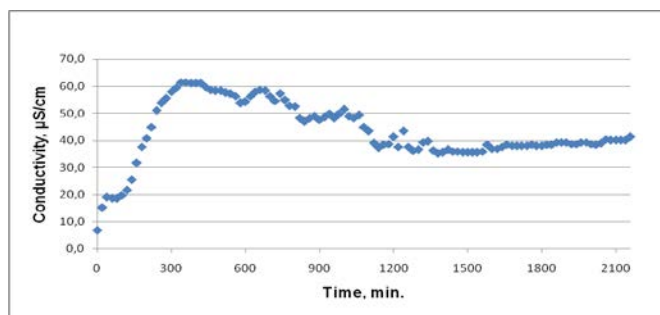
Fig. 1. The variation of the conductivity of 2 % BTSE solution in time

Fig. 2 highlights the variation of *p*H in time during hydrolysis process, an important factor to be considered. Should one desire to carry out the hydrolysis process a certain value or in a certain *p*H interval, than it is compulsory to use buffer systems in order to maintain the *p*H within the envisaged limits as *p*H is an important factor in establishing the deposition process, since the condensation reaction is favoured at basic values of *p*H and if the condensation of the silane solution is in an advanced stage, the resulted film will be a jellified one. Hence, the simultaneously monitoring of the conductivity and *p*H of the silane solution is of a paramount importance in establishing the optimum time for silane deposition.
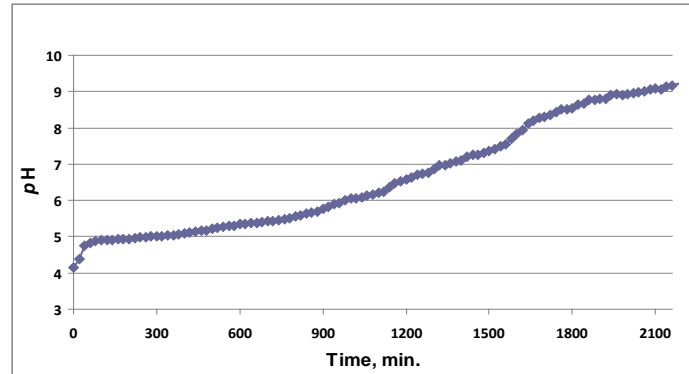
Fig. 2. The variation of the 2 % BTSE solutions pH in time

Open circuit potential

Fig. 3 depicts the variation of potential in time for the tested samples. One may see that for the coated samples from a silane solution with the pH adjusted to 11, the potential decreases in the first 3 min. and then stabilizes to a steady state value, while for the ones with the coating deposed from the silane solution prior to pH adjustment the potential varies in a relatively narrow range. A possible explanation, confirmed by the EIS data, is that in the case of cured samples, the coating cracks and some pores are generated in the coating, so that the bare metal is exposed, and hence the need for a multistage/multilayer coating procedure or a less drastic drying treatment is needed to eliminate the cracks and pores in the coating.
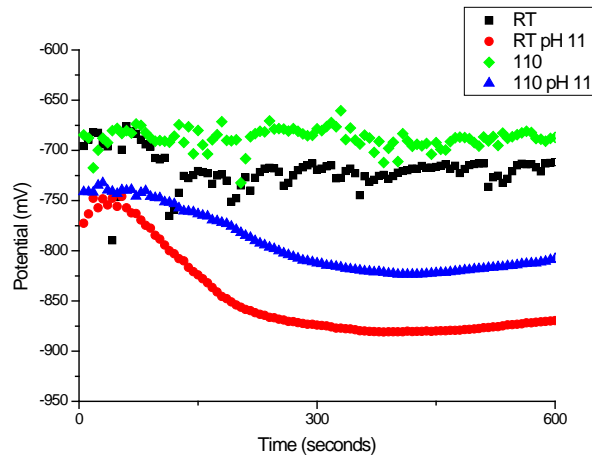
Fig. 3. The variation of potential in time for the 2% BTSE solution deposed on aluminium substrate in 3.5% NaCl electrolyte solution; where: RT –film cured at room temperature, RT pH 11 – film deposed from a solution with pH adjusted at 11 and cured at room temperature, 110 - film cured at 110°C, 110 pH 11 - film deposed from a solution with pH adjusted at 11 and cured at 110°C.

Electrochemical impedance spectroscopy

Fig. 4 depicts the Nyquist plots of EIS spectra for the 2% BTSE solution deposed on aluminium substrate in 3.5% NaCl electrolyte solution. Table 1 shows the values of the polarization resistance (R_p), capacitance (C), correlation coefficient (*r*), critical correlation coefficient (r_{critic}) and validation coefficient (k_{VD}). The validation coefficient was assessed using the procedure described in details in [15] this confirming that the circular regression model proposed for the EIS data holds and the resulting EIS data may be used with confidence.
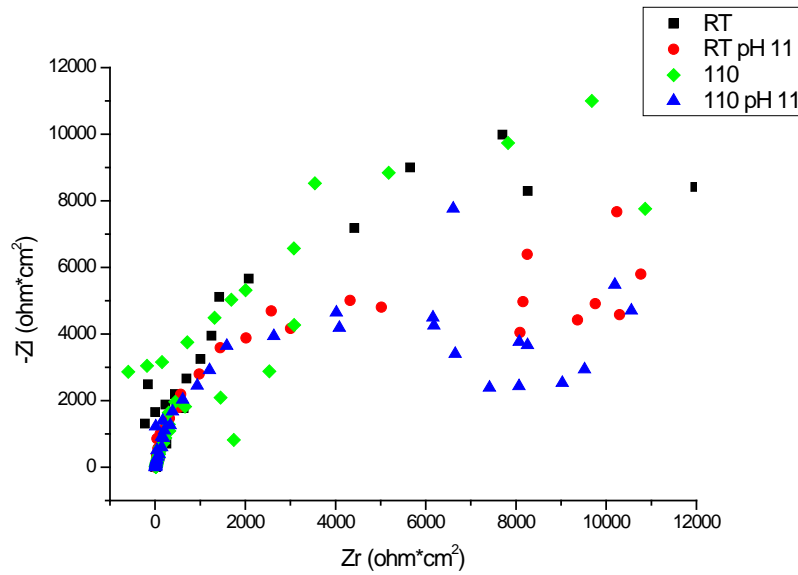
Fig. 4. The Nyquist plots registered for the 2% BTSE solution deposed on aluminium substrate in 3.5% NaCl electrolyte solution; where: RT –film cured at room temperature, RT *p*H 11 – film deposed from a solution with *p*H adjusted at 11 and cured at room temperature, 110 - film cured at 110°C, 110 *p*H 11 - film deposed from a solution with *p*H adjusted at 11 and cured at 110°C.

The EIS spectra of the silane film on aluminium substrate prior to pH adjustment and cured at 110°C show higher polarisation resistance than the one cured at room temperature, while the samples deposed from a solution with the pH adjusted to 11 registered a decrease in the polarization resistance in the case of a cure treatment at 110°C. The values of capacitance show that film for the sample deposed from a solution prior to pH adjustment and cured at room temperature is more compact than the one cured at room temperature indicating that, although the curing treatment should have a significant role in attaining a better barrier against corrosion, in this case, it led to a poorer quality coating.

Table 1

The values of R_1, R_2, C, r, r_{critic}, and k_{VD} for aluminium samples coated with BTSE 2%

Sample	R_1, ohm·cm²	R_2, kohm·cm²	C, µF·cm⁻²	No of points	r	r_{critic}	k_{VD}
Al BTSE 2%, RT	118.2	8.474	7.512	46	0.698	0.291	0.583
Al BTSE 2%, RT, pH 11	11.86	11.860	5.363	46	0.987	0.291	0.705
Al BTSE 2%, 110°C	67.46	26.63	0.149	46	0.824	0.291	0.646
Al BTSE 2%, 110°C, pH 11	22.74	8.492	7.496	46	0.974	0.291	0.701

Potentiodynamic polarization

The potentiodynamic polarization curves for the 2% BTSE solution deposed on aluminium substrate in 3.5% NaCl electrolyte solution are depicted in Fig. 5. As one may see from Table 2, the values of the i_{cor} are higher for the samples subjected to a curing process at 110°C.
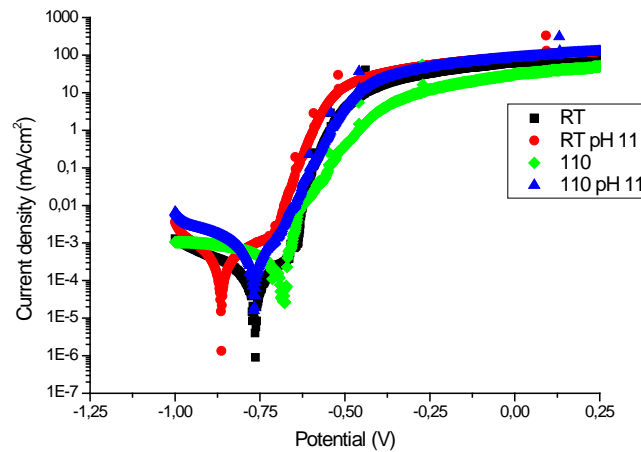
Fig. 5. The potentiodynamic polarization curves for the 2% BTSE solution deposed on aluminium substrate in 3.5% NaCl electrolyte solution; where: RT –film cured at room temperature, RT *p*H 11 – film deposed from a solution with *p*H adjusted at 11 and cured at room temperature, 110 - film cured at 110°C, 110 *p*H 11 - film deposed from a solution with *p*H adjusted at 11 and cured at 110°C.

Table 2

The values of i_{cor}, β_a, β_c for aluminium samples coated with BTSE 2%

Sample	i_{cor}, nA·cm⁻²	β_a , mV	β_c , mV
Al BTSE 2%, RT	31.63	56.9	-58.5
Al BTSE 2%, RT, pH 11	175.56	108.0	-90.2
Al BTSE 2%, 110°C	89.70	25.6	-82.0
Al BTSE 2%, 110°C, pH 11	201.77	68.9	-71.5

This, correlated with EIS data from Table 1 and with the OCP data from Fig. 3 may be explained, as suggested above, by the generation of cracks and pores in the silane layer during the curing process, leaving exposed certain patches of the bare metal, hence, a higher corrosion rate. However, as a whole, the values for i_{cor} are in the range of hundreds of $nA \cdot cm^{-2}$ and, accordingly to [16], the corrosion risk is moderate to low, therefore the corrosion is considerably slowed down by the protective layer. As this protective layer is not used on its own but as a substrate for further coatings (organic and inorganic additional layers) one may say that the silane coatings have proven successful in increasing the corrosion resistance and protection for the metallic substrate.

4. Conclusions

Electrochemical techniques offer a high versatility and supply valuable information during the characterization of some silane solutions and silane coatings deposed on aluminium substrates. The measurement of the silane solutions conductivity has been the defining step in establishing the optimum deposition time, namely in the case of the 2% BTSE solution the optimum zone being in the range of 300-380 min. with respect to the preparation time.

The corrosion behaviour of the silane coatings was investigated using electrochemical impedance spectroscopy and potentiodynamic polarization. The values of polarization resistance and capacitance determined by electrochemical impedance spectroscopy highlighted the influence of pH solution and curing treatment on the final silane film properties. The values of the polarization resistance of the film cured at 110°C show that the curing treatment of the silane coating generates cracks and therefore a multilayer deposition is necessary. The silane coatings ability to confer protection against corrosion was revealed by means of potentiodynamic polarization, a technique that has confirmed by the values of the corrosion current densities that silane coatings are an effective barrier against corrosion attack.

REFERENCES

[1] Liu, L., Hu, J.M., Zhang, J.Q., Cao, C.N., Improving the formation and protective properties of silane films by combined use of electrodeposition and nanoparticles incorporation, *Electrochimica Acta*, 52, (2006), 538-545.

[2] Hu, J.M., Liu, L., Ahang, J.Q., Cao, C.N., Effects of electrodeposition potential on the corrosion properties of bis-1,2-[triethoxysilyl]ethane films on aluminium alloy, *Electrochimica Acta*, 51, (2006), 3944-3949.

[3] Bajat, J.B., Miskovic-Stankovic, V.B., Kacarevic-Popovic, Z., Corrosion stability of epoxy coatings on aluminium pretreated by vinyltriethoxysilane, *Corrosion Science*, 50, (2008), 2078-2084.

[4] Palomino, L.M., Suegama, P.H., Aoki, V., Montemor, M.F., De Melo, H.G., Electrochemical study of modified cerium-silane bi-layer on Al alloy 2024-T3, *Corrosion Science*, 51, (2009), 1238-1250.

[5] Hu, J.M., Liu, L., Zhang, J.Q., Cao, C.N, Electrodeposition of silane films on aluminium alloys for corrosion protection, *Progress in Organic Coatings*, 58, (2007), 265-271.

[6] Altmann, S., Pjeiffer, J., The hydrolysis/condensation behaviour of methacryl-oxyalkylfunctional alkoxysilanes: structure-reactivity relations, *Monatshefte fur Chemie*, 134, (2003), 1081-1092.

[7] van Ooij, W.J., Zhu, D., Stacy, M., Seth A., Mugada, T., Gandhi, J., Puomi, P., Corrosion protection properties of organofunctional silanes. An overview, *Tsinghua Science and Technology*, 10(6), (2005), 639-664.

[8] Zaferani, S.H., Peikari, M., Zaarei, D., Danaee, I., Fakhraei, J.M., Mohammadi, M., Using silane films to produce an alternative for chromate conversion coatings, *Corrosion,* 69(4), (2012), 372-387.

[9] Pan, G., Schaefer, D.W., Morphology and water-barrier properties of silane films on aluminium and silicon, *Thin Solid Films*, 503, (2006), 259-267.

[10] Jenkins, M.L., Dauskardt, R.H., Bravman, J.C., Important factors for silane adhesion promoter efficacy: surface coverage, functionality and chain length, *Journal of Adhesion Science and Technology*, 18, 13, (2004), 1497-1516.

[11] De Graeve, I., Vereecken, J., Franquet, A., Van Schaftinghen, T., Terryn, H., Silane coating of metal substrates: complementary use of electrochemical, optical and thermal analysis for the evaluation of film properties, *Progress in Organic Coatings*, 59, (2007), 224-229.

[12] Deflorian, F., Rossi, S., Vadillo, M.d.C., Fedel, M., Electrochemical characterisation of protective organic coatings for food packaging, *Journal of Applied Electrochemistry*, 39, (2009), 2151-5157.

[13] Vaireanu D.I., Electrochemistry, Ed. AGIR, Bucharest, 2006.

[14] Vaireanu D.I., Handbook of Experimental Electrochemistry, Ed. Printech, Bucharest, 2008;

[15] Ciobotaru, I.A., Văireanu, D.I., Considerations regarding a novel coefficient for electrochemical impedance spectroscopy data validation, *Bulletin of Romanian Chemical Engineering Society*, 1(2), (2014), 123-134.

[16] Rodriguez, P., Ramirez, E, Gonzalez, J.A., Methods for studying corrosion in reinforced concrete, *Magazine of Concrete Research*, 46(167), (1994), 81–90.

FUNCTIONALIZED OLIGOTEREPHTHALATE STRUCTURES FROM PET WASTES, USEFUL AS ADDITIVES IN NANOCOMPOSITES

Monica DULDNER[1], Ana Mihaela FLOREA[1], Emeric BARTHA[2], Zina VULUGA[1], Simona NICA[2], Andrei SARBU[1], Cristian NICOLAE[1], Stela IANCU[1]*

[1]National Institute for Research & Development in Chemistry and Petrochemistry, 202 Splaiul Independentei, 060021, Bucharest, Romania
[2]Center of Organic Chemistry „C. D. Nenitzescu" of the Romanian Academy. 202B Splaiul Independentei, 060023, Bucharest, Romania

Abstract
Functionalized oligoterephthalate structures with balanced polar-nonpolar character, namely with nanofiller-phylic (ionic) functional groups and long chain fatty acids tails, useful as additives (alloying components) in polypropylene – SEBS rubber – montmorillonite nanocomposites, were developed using polyethylene terephthalate (PET) wastes as raw material. Two types of compounds have been prepared: i) oligoterephthalate ionomers with various ratios of polar/non-polar moieties (anionic surfactants) were obtained by concomitent glycolysis/transesterification reactions of PET waste with diethylene glycol (DEG) and 1,3-Dimethyl Isophthalate 5-Sodium Sulfonate (DMISNa) bisglycol esters obtained „in situ", optionally followed by esterification with long chain fatty acids; ii) quaternary ammonium salts of oligoterephthalates with hydrophobic tails (cationic surfactants) were obtained by aminoglycolysis of PET wastes with N-buthyl diethanolamine (NBuDEA), followed by esterification with long chain fatty acids and qaternization with Dimethyl sulfate (DMS).
The products were characterized by FT-IR, [1]NMR and TGA techniques. Measurement of surface tension and critical micelle concentration (CMC) revealed that the investigated oligoterephtalate ionomers exhibit a behavior quite similar to classical surfactants, depending mainly on the polar/nonpolar groups ratio within backbone. Interlayer distance of natural montmorillonite (Dellite HPS) treated with experimental functionalized oligoterephthalates were investigated by XRD. Nanocomposites polypropylene – SEBS rubber – montmorillonite modified with experimental functionalized oligoterephthalates were investigated in terms of mechanical properties. The nanocomposite materials obtained using montmorillonite organophilized with dimethyl dehydrogenated tallow ammonium salt (Dellite 67G) treated with one oligoterephthalate anionic ionomer structure resulted in a spectacular improvement of all physical-mechanical properties investigated, while the nanocomposite materials obtained using natural montmorillonite Dellite HPS modified with quaternary ammonium salts of oligoterephthalates exhibited fairly good results, quite similar to those of nanocomposites with Dellite 67G.

---

* Corresponding author, E-mail address:stela_iancu@yahoo.com (Stela Iancu)

Key words: PET wastes, glycolysis, esterification, oligoterephthalate ionomers, quaternary ammonium salts, nanocomposites

1. Introduction

In the contemporary context, it is becoming increasingly important to recycle plastics, for maintaining a clean environment, conservation of oil resources, reduction of greenhouse effect and energy preservation. PET polymer, which is used in volumes of millions of tones per year, mainly to package carbonated drinks, does not create a direct hazard to the environment but, due to its substantial fraction by volume in the waste stream and its high resistance to the atmospheric and biological agents, it is seen as a noxious material [1]. Therefore, the recycling of PET does not only serve as a partial solution to the solid waste problem, but also contribute to the conservation of raw petrochemical products and energy [2].

Today, PET bottles have become one of the most valuable and successfully recyclable materials. The chemical structure of PET is very well suited for chemical recycling, the most consistent recycling technique with the principles of sustainable development, since it can lead to the formation of the raw materials from which the polymer is made of, as well as other value-added products [3].

PET functional ester group can be cleaved by reagents such as water (hydrolysis), alcohols (alcoholysis), glycols (glycolysis), acids (acidolysis) and amines (aminolysis). Among these methods, alcoholysis or glycolysis by catalytic reactions [4-9] are the most attractive, some used on a commercial scale.
The glycolysis reaction is the molecular degradation of PET polymer by glycols, in the presence of trans-esterification catalysts, where ester linkages are broken and replaced with hydroxyl terminals. Glycolysis of PET is a versatile process, which allows the preparation of terephthalate oligoesters with tailored properties, given a wide range of depolymerisation reagents and various proportions of these reagents, as well as a great number of possible subsequent chemical reactions. The oligoesters obtained are used as precursors mainly for plastics [10], as well as in paint and lacquers production [11], such as: unsaturated and saturated polyesters and copolysters with special properties, i.e. biodegradable, water dispersible, etc [6,7, 12-20], polyurethanes [7, 21-25], epoxy resins [26-31], alkyd resins [15, 32], binder systems [27, 33], non-ionic surfactants [15, 34, 35], plasticizers [36, 37].

With the amount of work that is underway to blend materials, the interest in additives for nanocomposites is increasing all over the world. As it is well known, additives are indispensable in a range of established formulations, but recently their chemistry is moving beyond conventional applications, increasing the versatility and variety of these compounds.

Given it's low cost, polypropylene has traditionally been categorized as "commodity plastic" but it's properties continue to be expanded. In automotive industry, nanocomposite materials based on polypropylene tend to be the norm for exterior and interior parts, replacing metals and other plastics. These materials require better reinforcements for enhanced mechanical properties [38]. Numerous studies have been carried out in regard to PP-based nanocomposites using montmorillonite as a filler. By optimizing the organophillization treatment agent, used to cleave between montmorillonite layers, and by improving the dispersion of montmorillonite into the polymer matrix, PP based nanocomposites with dramatically improved mechanical properties can be obtained [39].

The present paper presents a study concerning the preparation of some functionalized oligoterephthalate structures (using waste PET as raw material), useful as alloying components in polypropylene – SEBS rubber –montmorillonite nanocomposites for the automotive industry. The objective of this study was to explore the possibility of obtaining, by this method, functionalized terephthalate oligomers with a balanced polar-nonpolar character, that would induce the intercalation and exfoliation of phyllosilicates, increase compatibilisation at interface, by decreasing the surface tension of the nanoclay and allowing better interactions between organophilic nanofiller and non-polar polymer matrix, thus enhancing dispersion of nanoparticles into the thermoplastic resins and, finally, improving the impact strength or toughness of nanocomposite materials. Our experiments were focused on **two directions**: 1. Obtaining oligoterephthalate anionic ionomers with various ratios of polar/non-polar moieties (anionic surfactants); 2. Obtaining quaternary ammonium salts of oligoterephthalates with hydrophobic tails (cationic surfactants).

2. Experimental

2.1 Synthesis of functionalized oligoterephthalate structures.

2.1.1 *Materials*
Post-consumer PET from bottles in flakes form (longitudinal dimension 6-8 mm), washed with clean water and dried at 100°C for 5 hours, intrinsic viscosity (according to ASTM D4603) 0.77 dL/g, were used for the degradation process. Diethylene Glycol (DEG), N-Buthyl Diethanolamine (NBuDEA), Dimethyl Sulfate (DMS) were purchased from E. Merck, and used without purification. 1,3-Dimethyl Isophthalate 5-Sodium Sulfonate (DMISNa) and Lauric Acid (LA) were obtained from Sigma-Aldrich, and used as received.
Catalysts: Titanium (IV) i-Propoxide (TIP) and Manganese Acetate Tetrahydrate (MATH) were purchased from E. Merck, and used as they were received.

2.1.2 *Synthesis methods*
The synthesis procedures mainly consisted in controlled solvolysis of PET wastes, followed by esterification with long chain fatty acids.

The synthesis method of the oligoterephthalates functionalized with anionic groups and possesing non-polar fatty acids tails is a simplified and efficient procedure, consisting in concomitent glycolysis/ transesterification reactions of PET waste with DEG and DMISNa bisglycole esters obtained „in situ", in order to yield terephthalate oligomers with nanofiller-phylic (polar) functional groups: hydroxyl and pendant ionic $SO_3^-Na^+$. Terminal OH groups were subsequently esterified with long chain fatty acids at various molar ratios, in order to accomplish a balanced polar - nonpolar character.

The synthesis procedure of the oligoterephthalates functionalized with cationic groups and possesing non-polar fatty acids tails consited in amino-glycolysis (glycolysis in the presence of tertiary amines) of PET with NBuDEA, followed by esterification with a long chain fatty acid (LA), and subsequent quaternization with DMS.

PET solvolysis, degradative transesterification and subsequent esterification reactions were conducted in a stainless steel polycondensation reactor of 1000 cm^3 capacity, fitted with a jacket with electrically heated agent, temperature controller, anchor stirrer with 60-70 rpm. stirring rate, nitrogen inlet, manometer, heated partial reflux condenser connected to a distillate collecting vessel, a vacuum system for the evacuation of the esterification by-products (if necessary).

Quaternization reactions were performed in a three neck glass flask, fitted wit a magnetic stirrer, thermometer, condenser and a dropping funnel. The flask was heated in an oil bath, placed on a heating magnetic plate.

2.1.2.1 *Degradative transesterification*
PET wastes were depolymerized in the presence of DEG and DMISNa diesters with DEG obtained in situ, at mole ratios glycol / PET between 0.8 -2.0 and DMISNa / PET in the range of 0.17-0.20, using 0.1 wt % TIP, based on the weight of PET, as transesterification catalyst. The reactions took place at atmospheric pressure under nitrogen atmosphere, at temperatures between 180 – 220 °C, during 4-5 hours.
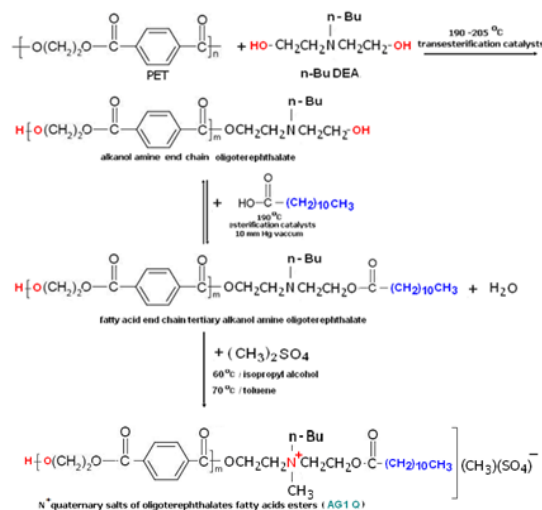
2.1.2.2 *Aminoglycolysis*
The chemical solvolysis of PET with N substituted ethanolamines is regarded as a glycolysis reaction catalyzed by a tertiary amine, therefore the term aminoglycolysis can be used to describe the process.

Amino ester derivatives of terephthalic acid are formed during the solvolysis with an excess of 0.3 – 1.0 mole % N-BuDEA/PET, using 0.5 wt % MATH, based on the weight of PET, as catalyst, at atmospheric pressure under nitrogen

atmosphere, at temperatures between 170 - 205°C, during 3-4 hours. Volatile products were distilled off during the process.

2.1.2.3 Esterification

The solvolysis products of PET (resulted from degradative transesterification and aminoglycolysis, described above) were subjected to esterification reactions with LA, at mol ratios OH groups / COOH groups of 1: 0.9 and 1: 0.6 respectively.

Esterificantion reactions were carried out at various mole ratios of OH groups / fatty acids, at atmospheric pressure and finally under medium vacuum, at temperatures between 140-190 °C, controlled by the evolution of the stoechiometric amount of water distillation.

2.1.2.4 Quaternization

Oligoterephthalate ammonium quaternary salts were obtained by quaternization of oligoterephthalate tertiary-alkanolamine fatty acid ester derivatives with DMS, for 4 hours, following two different procedures:

a) in isopropyl alcohol solvent, at 70°C.

b) in toluene solvent, at 60°C

Solvents were removed under vacuum, at low temperature.

2.1.3 Synthesis reactions

2.1.3.1 Oligoterephthalates with various ratios of polar/non-polar moieties (anionic surfactants) are described by the following reactions:

Oligoterephthalates with various ratios of polar/nonpolar moieties

2.1.3.2 Quaternary ammonium salts of oligoterephthalates with hydrophobic tails (cationic surfactants) are described by the following reactions:

2.1.4 *Analytical methods*

Final products and intermediates were analysed using various analytical techniques:

- melting temperature range Tm was estimated using a Boetius apparatus;
- acid, Hydroxyl and Amine numbers were determined by chemical titration;
- dynamic viscosity was evaluated on a „ Rheotest 2" rotating viscosimeter, at $25^{\circ}C$;
- relative viscosity of the oligoterephthalates was determined with an Ubbelohde viscometer with IIA capillary , using a solution of 0.5 g oligoterephthalates in 100 cm3 of phenol: tetrachloroethane 1:1 (w/w) blend, at $25^{\circ}C$;
- Fourier Transform Infrared (FTIR) spectra were recorded with a Bruker: Vertex-70 FTIR, in solid with ATR;
- ^{1}H-NMR spectra were recorded on a Varian Gemini spectrometer, operating at 300 MHz, with superconductive magnet, using $CDCl_3$ as solvent;
- thermal-induced weight loss of the samples were measured in dynamic heating by a SDT-MS hyphenated technique, using for simultaneous DSC-TGA a TA Instruments SDT Q600 coupled with a Pfeiffer Thermostar Mass Spectrometer;
- surface tension was evaluated using the ring method, on a Krüss EasyDyne device, with an error of $\pm 0.08\%$;
- contact angle was determined on a Krüss EasyDrop device, with a measurement error of ± 0.1.

2.2 Surface modification of montmorillonite clays with oligoester ionomers and quaternizated salts of oligoterephthalates fatty acid esters

2.2.1 *Materials*
Natural montmorillonite provided by Laviosa Chimica Mineraria, Italy (Dellite HPS)
Experimental functionalized oligoterephthalates.

2.2.2 *Preparation method*
Nanohybrids were obtained by surface modification of montmorillonite Dellite HPS with oligoester ionomers and quaternizated salts of oligoterephthalates fatty acid esters, using the solution intercallation method. In a 2% suspension of silicate in water, the functionalized oligoterephthalates were introduced, at layered silicate: functionalized oligoterephthalates rate of 1.0 : 0.3, under continuous stirring, at 80 ^{o}C., for 1 hour. The obtained mixture was centrifuged for 30 minutes at 500 rpm. The sediment was dried for 72 hours at 70 °C, and milled, yielding a powder with particle size < 60 μm.

2.2.3 *Analytical methods*
X-ray diffraction analysis was performed on a DRON diffract meter with horizontal goniometer; the CoKα radiation source (λ = 1.79021 Å) was used, filtered with Fe for removing Kβ component, in the Bragg–Brentano system (by reflection); the patterns were automatically recorded at small angles (2θ: 1.3÷12)

2.3 Preparation of polypropylene – SEBS rubber – modified montmorillonite nanocomposites

2.3.1 *Materials*
Polypropylene homopolymer Moplen HP 400R, with melt flow index 25 g/10 min (230°C, 2.16 Kg) and density of 0.900 g/cm^3(PP) was provided by Basel polyolefines, Italy. Linear, hydrogenated triblock copolymer Styrene Ethylbutylene Styrene, with 92 % styrene content, Mn 79100 and density of 0.91 g/cm^3 (SEBS) was provided by Kraton Polymers, USA. Natural montmorillonite provided by Laviosa Chimica Mineraria, Italy (Dellite HPS). Montmorillonite organiphilized with Dimethyl dehydrogenated tallow ammonium salt, with basal spacing d$_{001}$ 32.7 Å. (Dellite 67G) was provided by Laviosa Chimica Mineraria, Italy.

2.3.2 *Preparation method*
A standard nanocomposite material (D67) was obtained by homogenizing in the melt, using a DSE Brabender double screw extruder, at 180°C and 220 rpm., a mixture of 77,3 % PP, together with 12.4 % SEBS and 10.3 % Dellite 67G .
Experimental nanocomposite materials were prepared, using the same method, except for the mixture composition of 80 % PP, 13 % SEBS and 7 % Dellite HPS,

modified 1.0 : 0.3 with functionalized oligoterephthalates, and a mixture composition of 77.3 % PP, 12.4 % SEBS and 10,3 % Dellite 67G modified 1.0 : 0.3 with one of the functionalized oligoterephthalates (anionic surfactant).

2.3.3 *Analytical methods*

Mechanical properties of the nanocomposite materials were determined according to ISO 527, on molded test specimens ID type, using an Instron universal testing machine, in standard conditions of temperature and humidity (25 ^{o}C and 50% relative humidity).

3. Results and discussions

3.1 Physical-chemical properties of the functionalized oligoterephthalates are presented in Tables 1 and 2:

Table 1

Physical-chemical properties of oligoterephthalate fatty acid ester ionomers and oligoterephthalate tertiary-alkanolamine fatty acid ester derivatives (before quaternization)

Oligo-ester Code	Molar composition	Molar ratio OH/COOH fatty acid	Physical - chemical properties					
			Hydroxyl number, mg KOH/g		Acid number, mg KOH/g	Mn, g/mol calculated (Before esterif.)	Inh.visc. $[\eta]_{inh}$, dl/g	Dyn. Visc., η, cP	Soft. temp. ^{o}C
			after dist.	after esterif.					
N14	$EG_{0,59}DEG_{0,41}$ - $TA_{0,83}DMISna_{0,17}$	1 : 0.0	119	-	0.8	951	0.092	-	55
IN 9	$EG_{0,59}DEG_{0,41}$ $TA_{0,62}DMISNa_{0,13}LA_{0,25}$	1 : 0.6	110	38	1.9	1029	0.088	-	48
IN 8	$EG_{0,59}DEG_{0,41}$ $TA_{0,56}DMISNa_{0,11}LA_{0,33}$	1 : 0.9	114	10	2.9	993	0.075	-	46
AG2	$EG_{0,42}N\text{-}BuDEA_{0,58}$ $TA_{0,56}LA_{0,44}$	1 : 0.6	140	60	5.9	807	-	2800	-

Table 2

Amine number of oligoterephthalate tertiary-alkanolamine fatty acid ester derivatives

| Quaternized oligoterephthalate code	Solvent	Amine no., ml. 0.1 N $HClO_4$ /g	
		Before quaternization	After quaternization
AG2 Q1	Toluene	25.7	0
AG2 Q2	Isopropyl alcohol	25.7	2.3

3.2 ^{1}H NMR Spectra (CDCl$_3$) of the functionalized oligoterephthalates

Sample **N14** ^{1}H NMR spectrum, presented in Fig.1, exhibits two ranges at 8.1 ppm broad signal for aromatic protons from terephthalic oligomers, which displays a group of sharp signals (corresponding from left to right mainly to the following sequence: monomers, dimmers and trimers) and a broad signal centered at 8.3 ppm which is attributed to DMIS-protons. The signals in the range 3.4-4.7 ppm represents glycolic protons from EG and DEG, the most deshielded signal (at 4.64 ppm) correspond to EG interchain, then two large signals at 3.81 and 4.44 ppm correspond to DEG interchain protons and the rest of signals derived from DEG end chain. In this region appears also a broad singlet corresponding to OH , at 2.5 ppm.
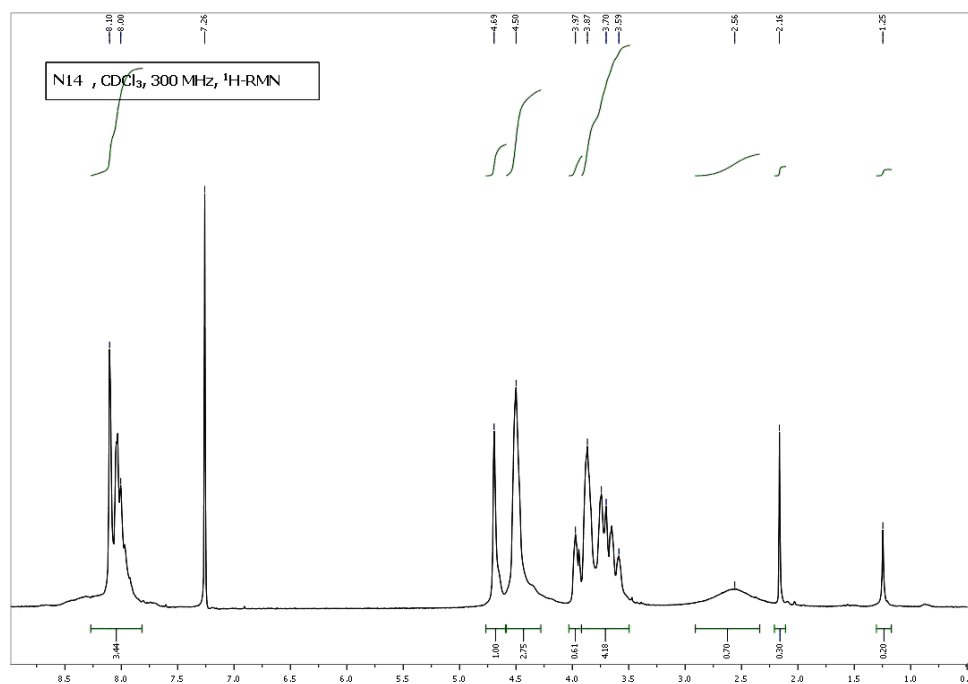
Fig. 1. ^{1}H NMR spectrum of N14 experimental oligoterephthalate ionomer

Sample **IN8** ^{1}H NMR spectrum, presemted in Fig. 2, exhibits three ranges. In the aliphatic acid protons regions, signals of: α methylene at 2.3 ppm, β at 1.65 ppm, (CH$_2$)$_8$ at 2.23 ppm and triplet for CH$_3$ at 0.87 ppm were used to assign the incorporation of lauric acid.
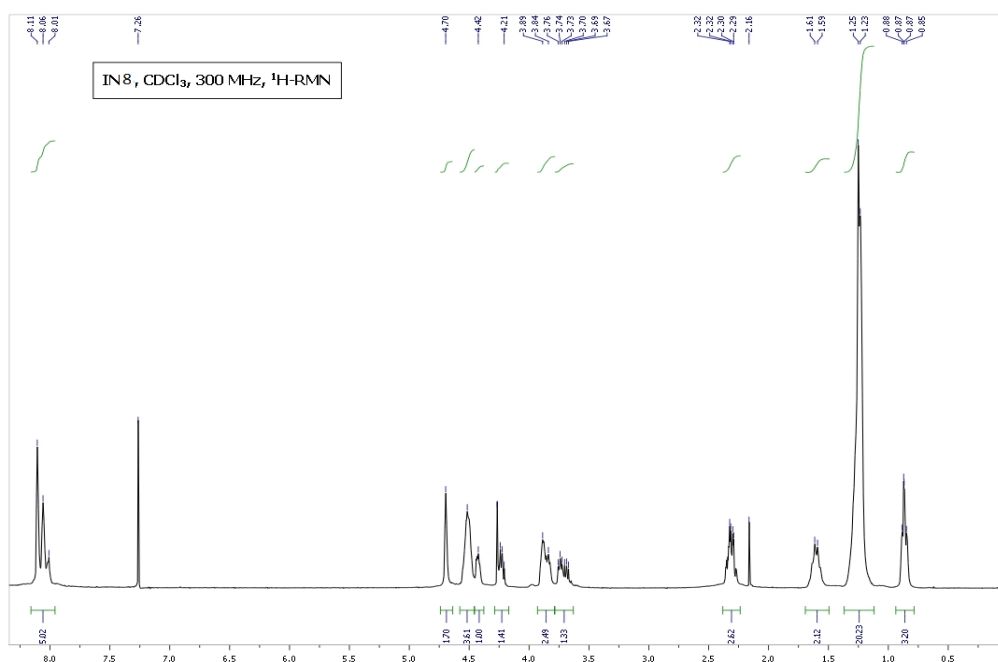
Fig. 2. ^{1}H NMR spectrum of IN8 experimental oligoterephthalate ionomer

Sample**s AG2 (a)** and **AG2Q1 (b)** (PET aminoglycolysate fatty acid ester, before and after quaternization) ^{1}H-NMR Spectra (Fig.3) exhibit three ranges, corresponding to aromatic protons, protons of methylene groups bonded to oxygen or nitrogen heteroatoms and hydroxyl protons (8.2-7.6 ppm, 4.2-4.8 ppm, and 3.3-2.4 ppm). It was notticed that whole region of protons linked on tertiary nitrogen shifted to the deschilded part of the spectrum, suggesting the quaternization PET/ nBuDEA product is a mixture of chemical compounds.

3.3 FT-IR Spectra of the functionalized oligoterephthalates

Sample **IN8** FT-IR spectrum, presented in Fig.4, shows that the most intense bands are at 1719 cm^{-1} (for C=O) and 2853-2923 cm^{-1} (C-H from aromatic and aliphatic acids).
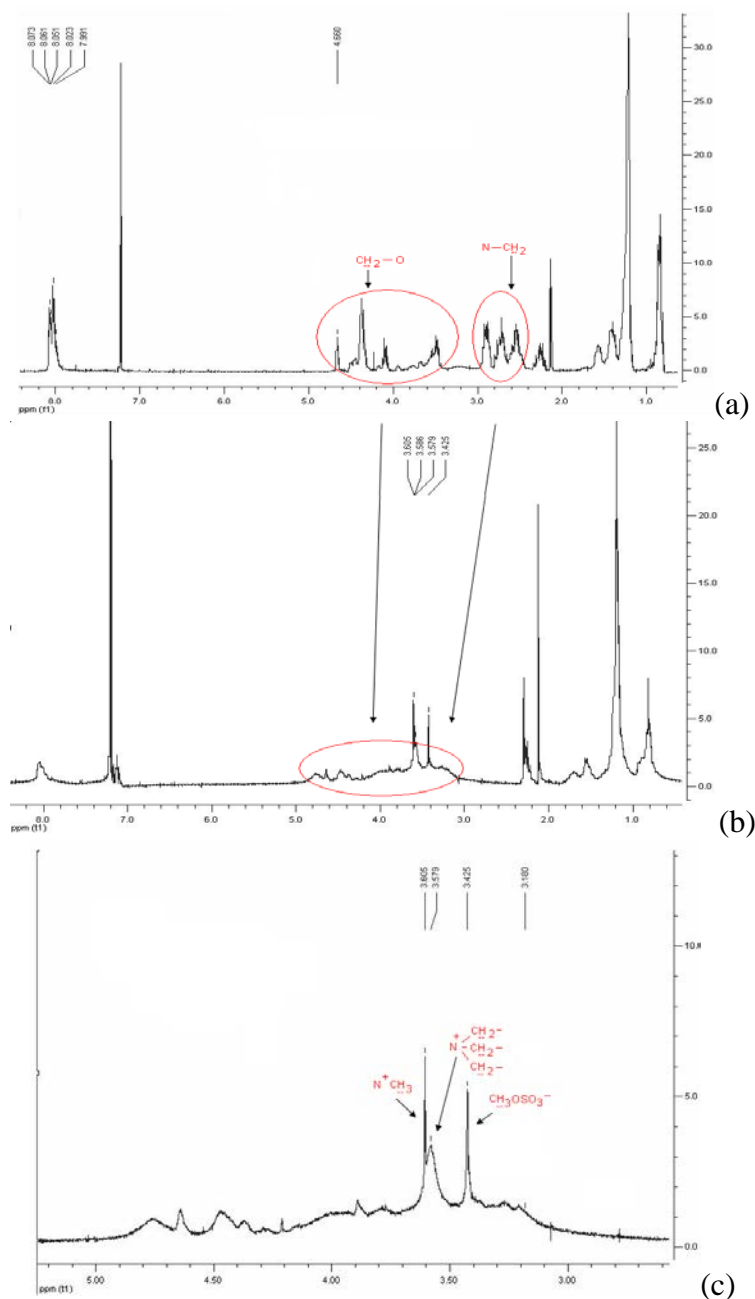
Fig. 3. ^{1}H-NMR spectra of experimental oligoterephthalate tertiary-alkanolamine fatty acid ester derivatives, (a) before quaternization (AG2), (b) after quaternization (AG2Q1), (c) detail of (b)
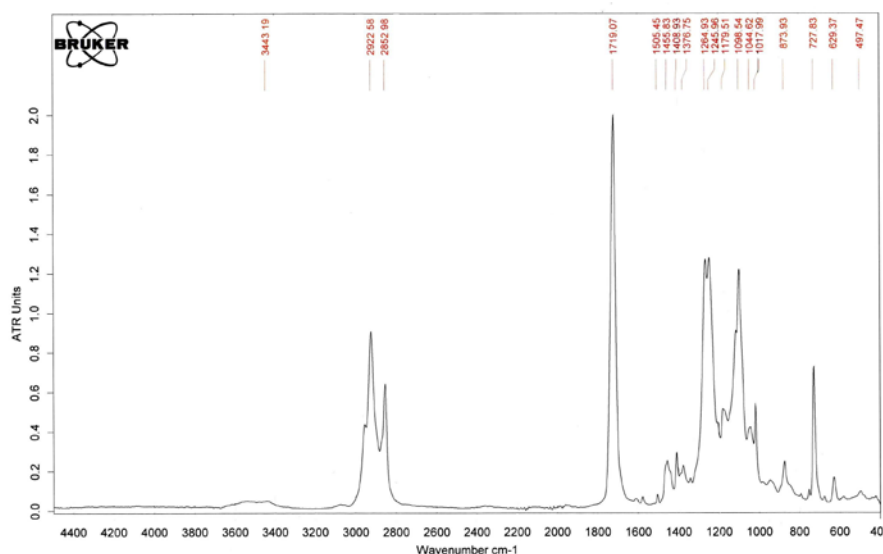
Fig. 4. FT-IR spectrum of IN8 experimental oligoester ionomer
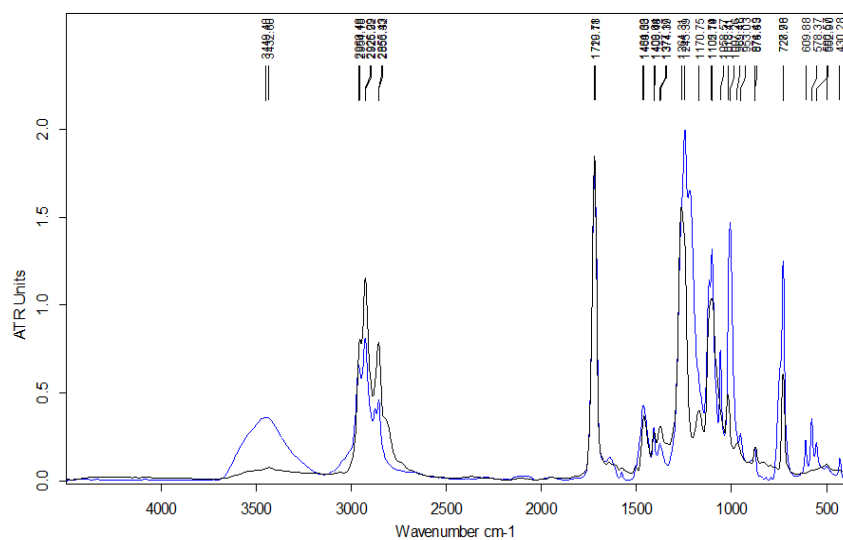
Fig. 5. FT-IR spectra of experimental oligoterephthalate tertiary-alkanolamine fatty acid ester derivatives before quaternization (AG2) and after quaternization (AG2Q1).

FTIR spectra (Fig.5) of the quaternized product **AG2Q1** (blue) indicate similar tipe of peaks as in the N-butyl diethanol amine ester products **AG2**, except for the peaks at: 2855-2856 cm^{-1} for tertiary nitrogen, 728-1008 cm^{-1} for methyl sulphate ion and 1466 cm^{-1} for quaternary ammonium ion.

3.4 DSC-TGA analysis of the functionalized oligoterephthalates
The results are presented in Fig.6.
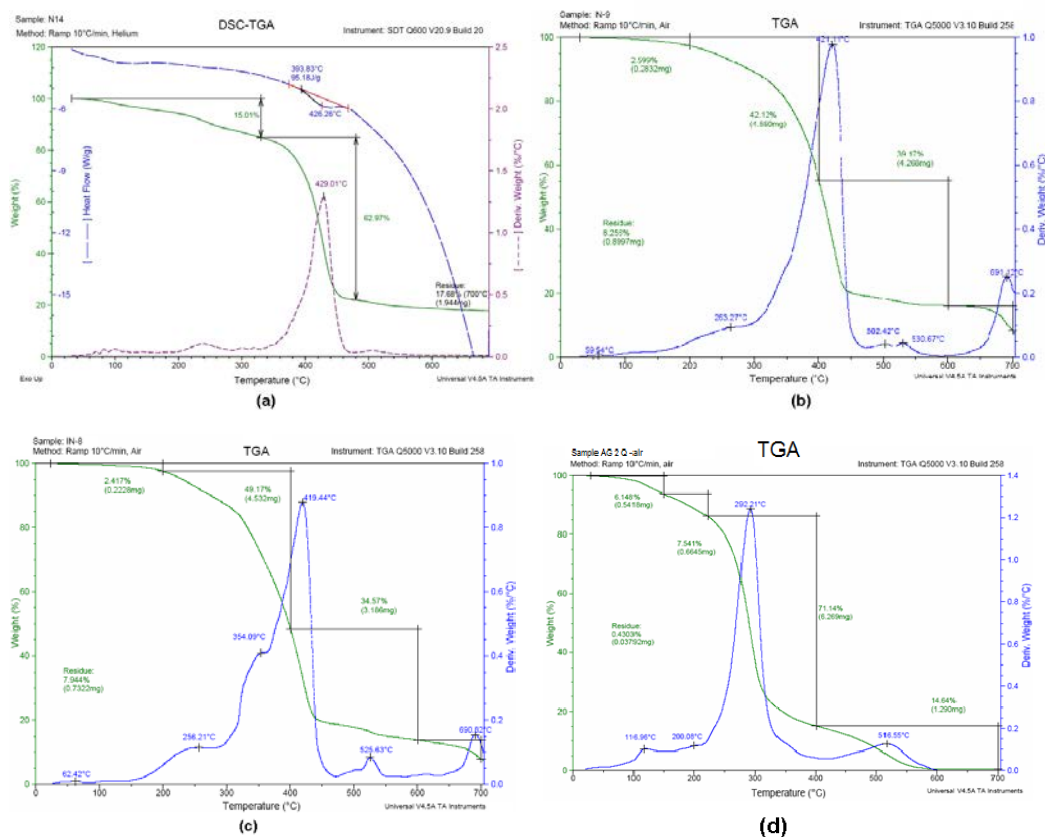
Fig. 6. TGA curves of experimental functionalized oligoterephthalates, (a) N14 oligoester ionomer, (b) IN8 oligoester ionomer, (c) IN9 oligoester ionomer, (d) AG2Q1 quaternized oligoterephthalate tertiary-alkanolamine fatty acid ester derivatives

One can see that up to 200-220°C N14 sample shows around 6-7 % loss and IN8, IN9 samples around 2-3 % due to low molecular compounds evaporation (e.g. free EG).

AG2Q sample shows a weight loss around 4 % bellow 100°C (accidental water content –in accordance with FT-IR), and an additional 1-2% weight loss below 200°C.

Between 220-270°C evaporation of compounds with higher molecular weights (DEG, N-BuDEA, unremoved by-products) or of their degradation products begins. Between 350-380°C evaporation of compounds with higher molecular weights or their degradation products continues and decomposition reactions of aliphatic end chains of the oligoesters (EG, DEG, N-BuDEA, LA) takes place. Mass fragments have been identified, corresponding to compounds such as: water,

formaldehyde, formic acid, CO_2, ethylene oxide, acetaldehyde, 1,4-dioxane, C_2-C_3 olefines etc. Since the molecular weights of these oligomers are relatively small, end chains are quite numerous and mass fragments of degradation products appear in a fairly large percentage. Temperature of maximum decomposition rate is around 300°C for AG2Q1 and above 400°C for the other samples.

3.5 Surface tension measurements for the functionalized oligoterephthalates

Surface tension measurements, presented in Table 3, show CMC (critical micelar concentration) values almost similar for all oligoester ionomers with anionic groups. The surface tensions at CMC decrease from sample N14 to sample IN9. The lowest value is recorded for sample IN9, being equal to 37.0 mN/m., denoting that this oligoester ionomer has a behavior quite similar to classical surfactants.

Table 3.
Surface tension and Contact angle measurements for the experimental oligoester ionomers

| Oligo-ester Code	CMC, (%)	Surface tension at CMC, (mN/m)	Contact angle, θ			
			θ°/Glass (hydrophilic)		θ°/Teflon (hydrophobic)	
			0.1%w.	1% w.	0.1% w.	1% w.
N14	4×10^{-1}	53.0	28.97	28.94	86.39	83.58
IN 9	4×10^{-1}	37.0	34.81	35.97	78.41	73.05
IN 8	2×10^{-1}	40.5	33.88	36.21	84.92	79.02

3.6 XRD analysis of the layered silicates modified with the experimental products

XRD spectra of nanohybrids obtained by surface modification of montmorillonite with oligoester ionomers and quaternizated salts of oligoterephthalates fatty acid esters, compared to unmodified natural montmorillonite (Dellite HPS – provided by Laviosa Chimica Mineraria).

For the anionic surfactants (Fig. 7) the XRD spectra show irregular lamellar intercalate structures with three types of intercalates. Both nanohybrids obtained by surface modification of montmorillonite with quaternizated salts of oligoterephthalates fatty acid esters (obtained in isopropylalcohol (AGQIP) and toluene (AGQT) show the peak characteristic for montmorillonite, but shifted to lower angles, proving the information regarding intercalated hybrids with ordered lamellar structure (Fig. 8). It can be seen that two types of intercalated structures

are formed: one with lamellar distance of about 14.5 A and the other with lamellar distance of about 35 A, similar to commercial alkyl quaternary ammonium organophilized montmorillonite.
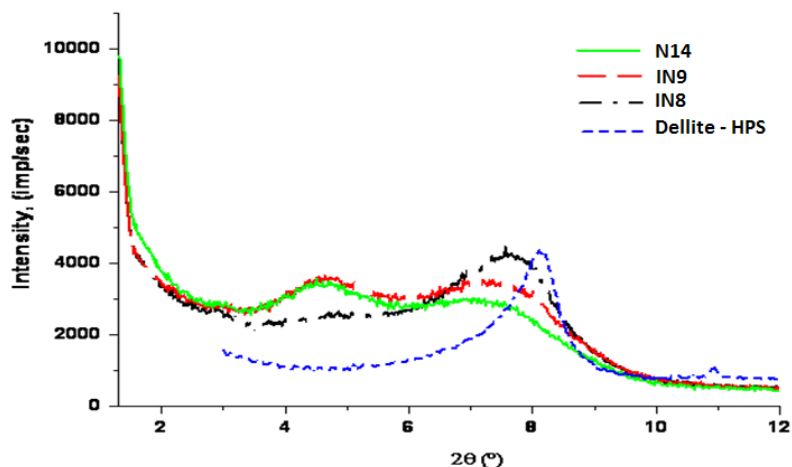
Fig. 7. XRD spectra of nanohybrids obtained by surface modification of montmorillonite with oligoester ionomers
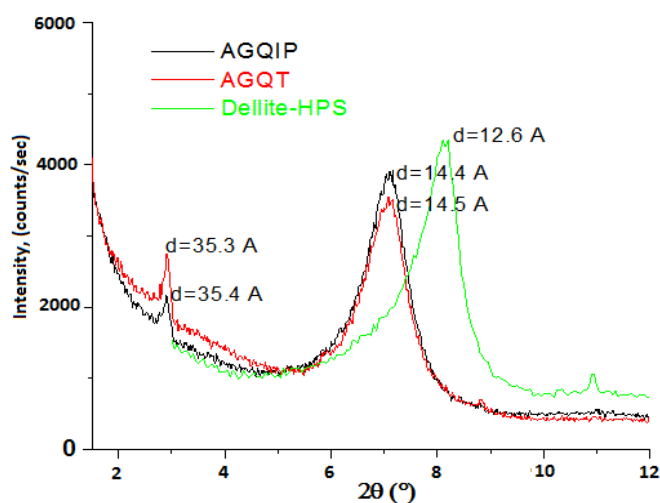

Fig. 8. XRD spectra of nanohybrids obtained by surface modification of montmorillonite with quaternizated salts of oligoterephthalates fatty acid esters

One can assume that this behaviour is due to organophilization of montmorillonite by two different mechanisms: one by cation exchange reaction and the other by ion-dipole interactions.

3.7 Mechanical properties of the nanocomposites

a) The mechanical properties of the nanocomposites based on PP, SEBS and layered silicate Dellite HPS modified with oligoester ionomers, compared to nanocomposite with layered silicate modified with Dimethyl dehydrogenated tallow ammonium salt Dellite 67G are presented below:
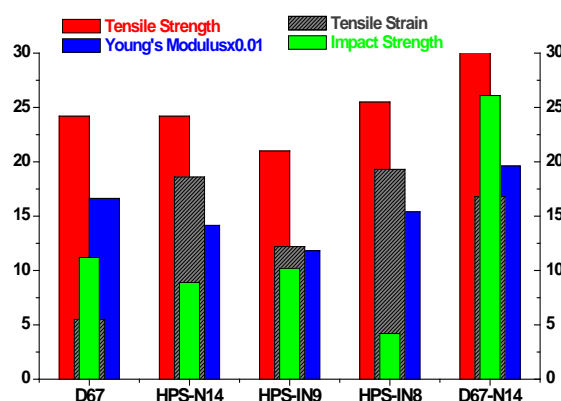
Fig. 9. Mechanical properties of experimental nanocomposites, based on Dellite HPS modified with oligoester ionomers, compared with standard nanocomposite (obtained with commercial organophilized montmorillonite Dellite 67G)

D67 – PP-SEBS nanocomposite based on Dellite 67G; **D67–N14** – PP-SEBS nanocomposite based on Dellite 67G modified with functionalized oligoterephthalate (anionic) N14; **HPS-N14** – PP-SEBS nanocomposite based on Dellite HPS modified with functionalized oligoterephthalate (anionic) N14; **HPS-IN9 –** PP-SEBS nanocomposite based on Dellite HPS modified with functionalized oligoterephthalate (anionic) IN9; **HPS-IN8 –** PP – SEBS nanocomposite based on Dellite HPS modified with functionalized oligoterephthalate (anionic) IN8.

While HPS phyllosilicates treatment with oligotereftalate ionomers induced a slight platelets intercalation and therefore did not lead to a significant improvement in of the PP/SBS nanocomposite physico-mechanical behavior, treatment of Dellite 67 with N14 oligoterephthalate ionomer resulted in a spectacular improvement of all physical-mechanical properties investigated.

b) The mechanical properties of PP-SEBS nanocomposites with montmorillonite organophilized with experimental quaternary ammonium salts were studied compared to PP-SEBS nanocomposite based on Dellite 67G .
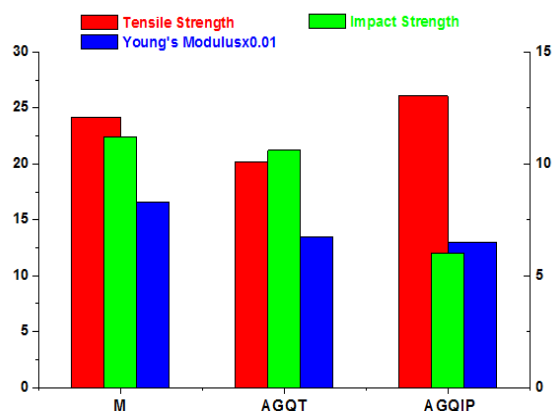
Fig. 10. Mechanical properties of experimental nanocomposites, based on Dellite HPC modified with quaternary ammonium salts of oligoterephthalates fatty acid esters compared with standard nanocomposite (obtained with commercial organophilized montmorillonite Dellite 67G

M – PP-SEBS nanocomposite based on Dellite 67G; **AGQT** – PP-SEBS nanocomposite based on Dellite HPS natural montmorillonite modified with quaternization product in toluene; **AGQIP** – PP-SEBS nanocomposite based Dellite HPS natural montmorillonite modified with quaternization product in isopropyl alcohol.

It can be noticed that the sample with montmorillonite modified with AGQT exhibits fairly good results, quite similar to those of polypropylene /Dellite 67G nanocomposite.

4. Conclusions

It may be concluded from the above work that it is possible to reuse PET wastes by chemical recycling, synthesizing new compounds with balanced polar-nonpolar character, namely:

• functionalized oligoterephthalate structures bearing anionic functional groups and long chain fatty acids tails, showing a behavior quite similar to classical surfactants, depending mainly on the polar/nonpolar groups ratio within backbone, which could be a promising choice for using as compatibilisers and dispersing agents in polypropylene- SEBS rubber- organophillized layered silicates nanocomposites;

• quaternary ammonium salts of oligoterephthalates with hydrophobic tails, which can be used as organophillization agents for natural montmorillonite, exhibiting quite similar rezults to commercial organophillized layered silicates when utilized in polypropylene- SEBS rubber- layered silicates nanocomposites.

REFERENCES

[1] Scheirs J., *Polymer recycling: Science, Technology and Applications*, John Wiley & Sons, Ltd., Chichester, West Sussex, England (*1998*).

[2] Sinha V., Patel M. R., Patel J. V., *J Polym Environ.*, 18, (2010), 8.

[3] Achilias D.S., Karayannidis G.P., *Proceedings of the international conference ''Protection and restoration of the environment VI''* Skiathos, 1–5 July 2002, 925–936.

[4] Hu L. C., Oku A., Yamada E., Tomari K., *Polym. J.*, 29, (1997), 708.

[5] Vaidya U. R., Nadkarni V. M., *J. Appl. Polym. Sci.*, 35, (1988), 775.

[6] Vaidya U. R., Nadkarni V. M., *J. Appl. Polym. Sci.*, 38, (1989), 1179.

[7] Baliga S., Wong, W. T., *J. Polum. Sci. Part A: Polym. Chem.*, 27, (1989), 2071.

[8] Colomines G., Robin J.J., Tersac G., *Polymer*, 46, (2005), 3230.

[9] Bartha E., Iancu S., Duldner M., Vuluga M. D., Draghici C., Teodorescu F., *Revista de Chimie* 62 (4), (2011), 401-408.

[10] Dupont L. A., Gupta V. P., *J. Vinyl Technol.*, 15, (1993), 100.

[11] Tosselli M., Impagnatiello M., Stramigioli C., Pilati F., Mazzoli G., Benezzi G., *Polym. Recycl.*, 2, (1996), 27.

[12] Tong S. N., Chen D. S., Chen C. C., Chung L. Z., *Polymer*, 24, (1983), 469.

[13] Pimpan V., Sirisook R., Chuavjuljit S., *J. Appl. Polym. Sci.*, 88(3), (2003), 788-792.

[14] Suh D.J., Park O.O., Yoon K.H., *Polymer,* 41(2), (2000), 461-466.

[15] Karayannidis G. P., Achilias D. S., Sideridou I.D., Bikiaris D. N., *European Polymer Journal* 41, (2005), 201–210.

[16] Abdel-Azim A.A., Mekewi M.A., Gouda S.R., *Polym. Recyl.*, 3 (3), (1997/1998), 173.

[17] Itoh et al. US Pat. 6,730,709/ 2004.

[18] Locquengh et al. US Pat 6,413,292/ 2002.

[19] Iancu, S; Duldner, M; Bartha, E; et al RO. 127648/ 2014.

[20] Ilie C., Iancu S., Duldner M., Anghel D. F., *Rev. Roumaine Chim.*, 56 (7), (2011), 725-734.

[21] Lee, S-C., Sze Y-M., Lin C-C., *J. Appl. Polym. Sci.*, 55, (1995), 1271.

[22] Tersac G., Hubert F., Durand G., Quilleron J., Riveiro J., Marechal J.C., *Cellular Polymers,* 14, (1995), 14-40.

[23] Patel M.R., Patel J.V., Sinha V.K., *Polymer Degradation and Stability,* 90, (2005), 111-115.

[24] Kacperski M., Spychaj T., *Polym. Adv. Technol.*, 10, (1999), 624.

[25] Duldner M., Iancu S., et al. EP2565226 A1 /2013.

[26] Atta A. M., *Prog. Rubber Plast. Recycl. Technol.*, 19 (1), (2003), 17.

[27] Farahat M.S., Nikles D.E., *Macromol Mater Eng,* (2001), 286- 695.

[28] Fabrycy E., Leistner A., Spychaj T., *Adhesion*, 44, (2000), 35.

[29] Spychaj T., Fabrycy E., Spychaj S., Kacperski M., *J. Mater. Cycles Waste Manag.*, 3, (2001), 24.

[30] Spychaj S., Spychaj T., *Polimery (Warsaw)*, 46 (2001), 60.

[31] Fabrycy E., Spychaj T., Pilawka R., *Polym. Recycl.*, 6, (2001), 49.

[32] Pilati F., Toselli M., Agostini A., Stramigioli C., Dinelli M., Ballotta S., *Polym. Recycl.*, 2 (1), (1996), 35.

[33] Farahat M.S., Nikles D.E., *Macromol Mater Eng,* (2002), 287-353.

[34] Abdel-Azim A. A., Mekewi M. A., Gouda S. R., *Int. J. Polym. Mater.*, 51(9), (2002), 813.

[35] Atta A. M., Abdel-Rauf M.E., Maysour N. E., Abdul-Rahiem A. M., Abdel-Azim A., *Journal of Polymer Research,* 13, (2006), 39 –52.

[36] Bathe, US Patent 5,068,395 / 1991.

[37] Duldner M., Iancu S., RO 128212 A2/ 2013.

[38] Tolinski M., Andrew W., *Additives for Polyolefins*, Applied Science Publishers, First edition 2009, Published by Elsevier Inc, Chapter 1, pp. 3-8.

[39] Oritomi S. M., Atanabe T. W., Anzaki S. K, " Polypropylene Compounds for Automotive Applications" *R&D Report, "SUMITOMO KAGAKU"*, vol. 2010-I.

REMOVAL OF ^{137}Cs IONS FROM AQUEOUS RADIOACTIVE WASTE USING NICKEL FERROCYANIDE, PRECIPITATED ON SILICA GEL

Laura Ruxandra ZICMAN[1*], Elena NEACSU[1], Laurentiu DONE[1,3], Liviu TUGULAN[1], Felicia DRAGOLICI[1], Bogdan Tudor OBREJA[1],Tanase DOBRE[2]

[1]Horia Hulubei National Institute for Nuclear Physics and Engineering, P.O.Box MG-6, RO-077125 Bucharest-Magurele, Romania
[2]University Politehnica of Bucharest, Department of Chemical and Biochemical Engineering, 1-7 Polizu street , Bucharest, Romania
[3]University of Bucharest, Doctoral School on Physics, POB MG-11, Magurele-Bucharest, 077125, Romania

Abstract
The waste waters from nuclear engineering containing corrosion and fission products fall in the category of medium or low level radioactive wastes. These waste waters must be treated in order to decontaminate prior to be released in rivers or lakes. Additionally these waste waters can contain some organic products, like surfactants from laundry. The ion exchange is the most efficient treatment technology for radionuclides removal from a variety of waste water streams with low and intermediate pollution level. Unfortunately this technology is not selective because all ions from polluted waters are fixed. In the last time the selective separation of radioactive ions from this water type is an important research subject. Sorption with or without chemical interaction in solid phase of radioactive species is a promising procedure.

A study regarding removal of ^{137}Cs from radioactive waters from spent nuclear fuel pools using a synthetic inorganic sorbent was performed. Nickel ferrocyanide, precipitated on silica gel, with size of granules 0.5 - 0.8 mm, was used as sorbent. The aqueous radioactive waste initial characteristics were^{137}Cs concentration 3000 Bq/L, pH 6.50, conductivity 6.44 μS/cm, chloride content < 0.01 ppm, and solid residue 3.90 mg/L. No fission or activation gamma emitter was identified. Batch experiments as a function of pH, contact time, sorbent/waste mass ratio were carried out. Isolated and synergic effects of process parameters were determined in order to establish acceptable limits for variability in performance.

Simple kinetic and thermodynamic models have been applied to the rate and isotherm sorption data and the relevant kinetic and thermodynamic parameters were obtained. The sorbent capacity was established using the Freundlich and Langmuir adsorption isotherm models. The decontamination factors in terms of separation yield were determined. The checked sorbent has a high separation capacity of Cs^+ from aqueous radioactive waste. Computation examples on the practical use of this sorbents are already presented.

Keywords: radioactive waste, cesium, ferrocyanide, kinetic, thermodynamic, sorption isotherm

---

[*] Corresponding author; Email: laura.zicman@nipne.ro (Laura Zicman)

1. Introduction

The increasing pressure to reduce the release of radioactive and other toxic substances into the environment requires constant improvement/upgrading of processes and technologies for treatment and conditioning of liquid radioactive waste. Treatment of liquid radioactive waste involves the application of different methods to meet the requirements both for the release of decontaminated effluents into the environment and the conditioning of waste concentrates for disposal.

At many of the nuclear power plant reactors, spent fuel from their operations is stored, pending decisions on its final disposition. Currently, most spent nuclear fuel is safely stored in specially designed pools at individual reactor sites around the world, but some problems associated with this spent fuel storage have emerged and caught the attention in the international nuclear community. Concerns principally focus on the ageing fuel storage facilities, their life extension, and the ultimate disposal of spent fuel assemblies [1].Spent nuclear fuel pools (SNFP) were established only for temporal spent fuel storage for at most 20 years. It has been assumed that it is sufficient period to which final disposal of spent nuclear fuel would be determined. However, nowadays it is more convenient in many nuclear power plants to enhance pool capacity and to store spent fuel during the whole nuclear power plant lifetime, which is about 40 years.´

As coolant and, at the same time, as a protection against radiation, deionized water is used in storage pools. In spent fuel storage pools fuel cladding could be damaged and the fuel's volatile fission products, including 30-year half-life ^{137}Cs, would be released. ^{137}Cs is an important radio-contaminant and represents a serious radiological hazard because as an alkaline element, it is easily assimilable by living organisms [2]. Different methods such as chemical precipitation, adsorption, and ion exchange are applied for radioactive wastes treatment [3–9]. Ion exchange technique in which various type of ion exchangers have been widely used is an attractive method because of its simplicity, selectivity, and efficiency [10–17].

The transition metal ferrocyanides were immobilized on different support materials and were used to remove cesium ions. The transition metal ferrocyanides immobilized on an anion exchange resin are simple and easy to prepare, and obtainable in any given conditions: they are non hygroscopic and granular, thus they can be in a dry state. Several applications of these resins to remove radioactive caesium ions have been reported [18 - 21].Composite sorbents based on potassium nickel ferrocyanide embedded in silica gel matrix were prepared and characterised by powdered X-ray diffraction analysis, IR spectra, Mössbauer spectra and electron microscopy [22].

Spent nuclear fuel generated in VVR-S Research Reactor at Magurele, Romania was stored in the Interim Spent Fuel Storage Facility, away from the reactor building. Two failed fuel elements allowed[137]Cs to be released in storage water from one pool. [137]Cs concentration is 3000Bq/L, pH 6.50, conductivity 6.44 µS/cm, chloride content< 0.01 ppm, and solid residue 3.90 mg/L. No fission or activation gamma emitter was identified.

Considering the above mentioned facts, the principal purpose of this study was to evaluate the removal of ^{137}Cs from radioactive waters from spent nuclear fuel pools using potassium nickel ferrocyanide, precipitated on silica gel (PNF-SG). Taking in consideration that one gram of ^{137}Cs has an activity of 3.215 terabecquerel [23], the Cs concentrations required were obtained using inactive CsCl, ^{137}Cs being used as tracer. The effect of different parameters such as pH, contact time, sorbent/waste mass ratio, temperature and initial concentration on the adsorption process was investigated. The adsorption process is evaluated from kinetic, isotherm, and thermodynamic point of view. Also, the decontamination factors in terms of separation yield were determined.

2. Experimental

2.1. Chemicals and reagents

All the reagents used in this work were of AR grade chemicals and were used without further purification. Cesium as cesium chloride was purchased from Sigma–Aldrich Co. Working solutions were prepared by dissolving CsCl in radioactive water from spent nuclear fuel pool.

PNF-SG, was supplied as granules, 0.5 - 0.8 mm size, from SIA "Radon" Moscow, Russia.

2.2. Instrumentation

Cesium concentration was determined by gamma spectrometry using a high resolution gamma-ray spectrometer, Canberra type, GENIE 2000 version 3.2 software and **L**aboratory **SO**urceless **C**alibration **S**oftware (LabSOCS), with 47.5% relative efficiency.

2.3. Batch sorption studies

Batch experiments were performed under kinetic and equilibrium conditions. To determine the pH range at which the maximum uptake of Cs^+ ions would take place on PNF-SG, a series of 250mL polypropylene Erlenmeyer flasks, each containing 1g, 3 g and 5 g of PNF-SG was filled with 250 mL of 1000 mg/L Cs^+ solution. The initial pH was adjusted to values ranging from 3.0 to 10.0 using dilute solution of hydrochloric acid or sodium hydroxide. The flasks were shaken for 2h to attain equilibrium. Preliminary investigations showed that the sorption process of each studied ion was completed after 2h. The suspension obtained was filtered to separate the solid from the liquid phase. The radioactivity

of clear liquid phases obtained was measured in order to obtain quantitative data of Cs$^+$ adsorption.

2.3.1. Kinetic experiments

Kinetic studies were performed at four different temperatures (298, 308, 318 and 328 K) using an initial ion concentration of 1000 mg/L. Also, to study the kinetic of the reaction, the adsorption capacity of the PNF-SG was measured at different time intervals (30 –120 min). For these investigations, adsorbent/waste mass ratio of 0.02 was used and the solution was kept under stirring in a thermostat shaker adjusted at the desired temperature. The amount of ion adsorbed at a time t, q_t (mg/g), and the distribution coefficient, k_d (mL/g) were calculated as follows:

$$q_t = (C_0 - C_t)\frac{V}{m} \tag{1}$$

$$k_d = \frac{(C_0 - C_t)}{C_t} \times \frac{V}{m} \tag{2}$$

where C_0 and C_t are the initial and equilibrium concentrations (mg/L) of Cs$^+$ in solution, V the solution volume (L) and m is the weight (g) of the PNF-SG.

2.3.2. Sorption equilibrium experiments

In the experiments of sorption isotherm measurements, 250 mL of the metal ion solution of different concentrations (100–1000 mg/L) were agitated with 5 g of PNF-SG at different temperatures (298, 308, 318 and 328 K) and at initial pH of 3.0. After the established contact time (2 h) was reached, the suspension obtained was filtered and the amount of the metal ion retained in the PNF-SG phase (mg/g) was estimated.

All batch experiments were carried out in duplicate and the mean values are presented.

3. Results and discussion

3.1. Effect of experimental condition on adsorption process

3.1.1. Dosage effect

The removal percentage of Cs$^+$ increases with increasing of solid to liquid ratio from 0.004 to 0.02 g/mL and the maximum uptake was achieved at 0.02 g/mL (Fig. 1). Therefore, the optimized solid to liquid ratio of 0.02 g/mL was selected for further experiments.
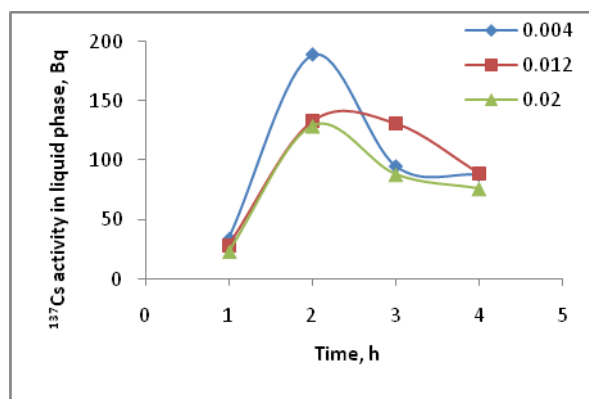
Fig. 1. Effect of solid/liquid ratio

3.2.2. Effect of contact time

The amount of adsorbed ions onto PNF-SG at different contact time is shown in Fig. 2. The uptake of ions increased with time and reached equilibrium after 90 min. The sorption process was initially very fast and between 80% and 90% of the maximal capacity was obtained within 30 min. This quite rapid removal was due to the porous structure of the composite, which allows the facile diffusion of the ions to the exchange sites. The adsorption of ions gradually decreased with time until saturation was attained. The two stage sorption mechanisms with the first rapid and quantitatively predominant and the second slower and quantitatively insignificant, has already been reported [24].
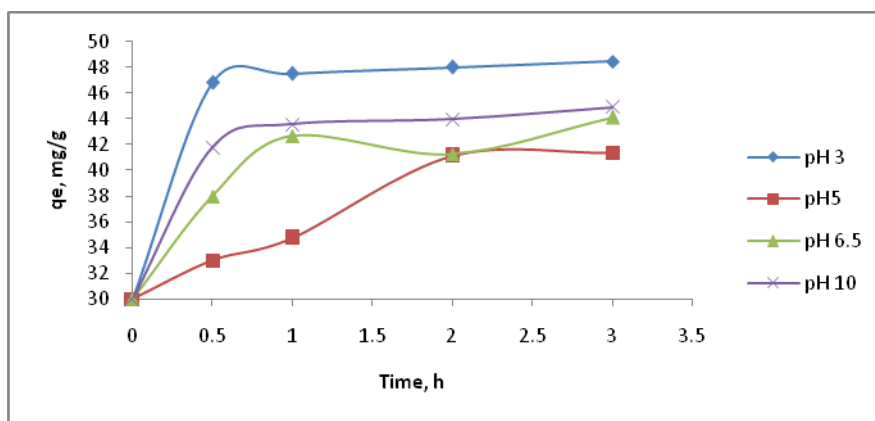
Fig. 2. Effect of contact time on Cs^+ adsorption

3.2.3. Effect of pH

Metal sorption from aqueous solutions can be greatly affected by the pH of the solution, which affect not only the binding sites (e.g. degree of protonation) but also the metal chemistry (e.g. speciation and precipitation).

The amount of Cs^+ uptake as a function of initial pH is shown in Fig. 3. It was concluded that acidic and alkaline media are favourable for uptake process. This could be attributed to:

-in acidic media Cs is present completely as soluble Cs^+;

-in alkaline solutions formation of mixed precipitates of transition metal ferrocyanides and hydroxides occurs [25].
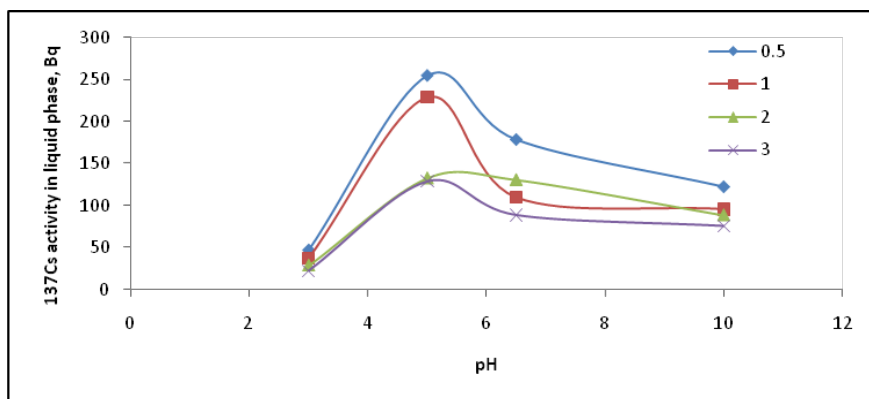
Fig. 3. Effect of initial pH on Cs^+ adsorption

The highest uptake was observed at pH 3 and pH 10. Since it has been reported dissolution of transition metal ferrocyanides at pH>10 [25], all future sorption experiments in this work were carried out at initial pH value of 3.

3.2.4. Effect of temperature

The adsorption removal of Cs^+ onto PNF-SG at four different temperatures 298, 308, 318, 328 K was examined (Fig. 4).The adsorption capacity increases with increasing the temperature, confirming that the adsorption process was endothermic. The data were used to estimate the thermodynamic parameters.
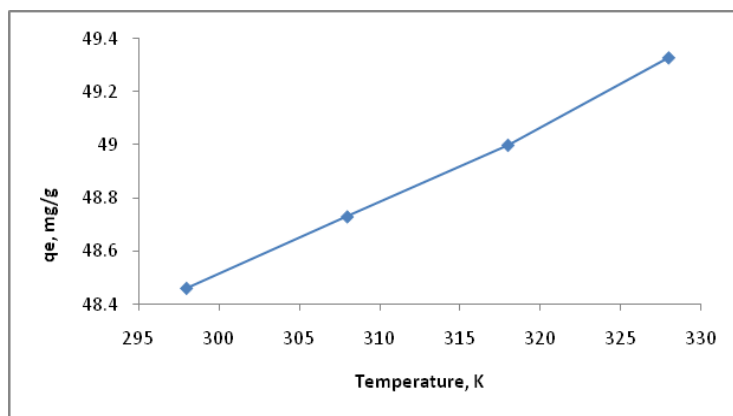

Fig. 4. Effect of temperature

3.3. Kinetic sorption modeling

Two kinetic models including pseudo-first-order and the pseudo-second-order were used to estimate the kinetic parameters. The integrated pseudo-first-order model expressed as follows [26]:

$$\ln(q_e - q_t) = \ln q_e - k_1 t \tag{3}$$

where q_e and q_t are respectively the amount of ions adsorbed per unit mass of PNF – SG at equilibrium and at any time t (mg/g); k_1 is the rate constant of pseudo-first-order sorption model (min^{-1}).

The slope and intercept of the plot of ln (q_e - q_t) against t is shown in Fig. 5 and they were used to calculate k_1 and q_e (Table 1).
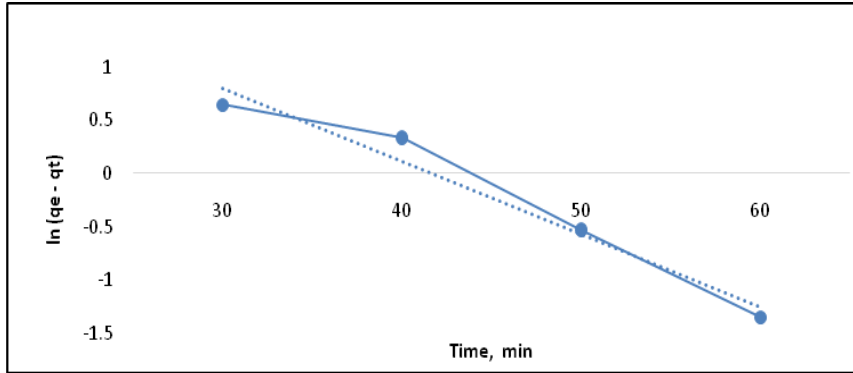
Fig. 5. Pseudo first-order kinetic plots for the sorption of Cs$^+$ onto PNF – SG at 298 K

The pseudo-second-order model and initial sorption rate (h) are written as [25]:

$$\frac{t}{q_t} = \frac{1}{k_2 q_e^2} + \frac{1}{q_e} t \tag{4}$$

$$h = k_2 q_e^2 \tag{5}$$

where k_2 is the rate constant of pseudo second-order equation (g/mg min) and $h = k_2 q_e^2$ is the initial sorption rate (mg/g min).

The values of t/q_t were linearly correlated with t as it can be seen in Fig. 6.

The important parameters including pseudo-second-order rate constant, k_2 (g/mg min), the equilibrium sorption capacity, q_e and the initial sorption rate, h (mg/g min) were determined from the slope and the intercept of the plot (Table 1).

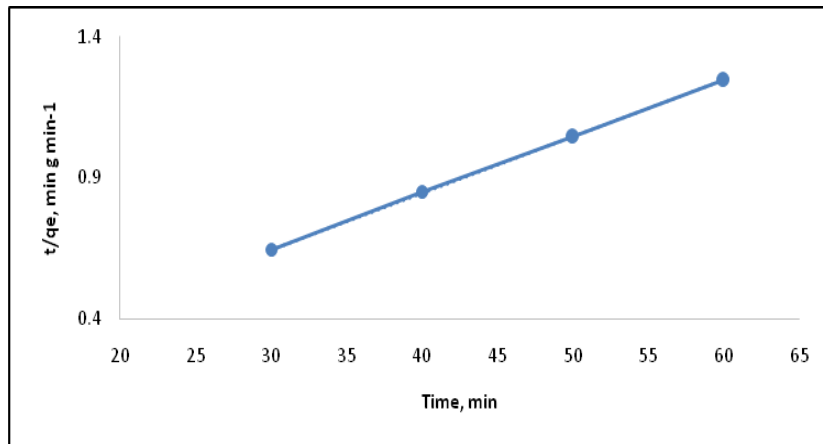**Fig. 6.** Pseudo second-order kinetic plots for the sorption of Cs$^+$ onto PNF – SG at 298 K

Table 1.

The calculated parameters of the pseudo first-order and pseudo second-order kinetic models for Cs$^+$ions sorbed onto PNF – SG at 298 K

First-order kinetic parameters			Second-order kinetic parameters				$q_{e, exp}$, (mg/g)
k_1 (min^{-1})	$q_{e, calc}$, mg/g	R^2	k_2 (g/mg min)	$q_{e, calc}$, mg/g	h (mg/g min)	R^2	
0.683	4.406	0.965	0.0087	50	21.74	0.999	48.46

The value of the correlation coefficients (R^2) and agreement of calculated q_e with experimental data revealed that sorption process can be described well by pseudo-second-order equation. The rate of ion exchange process is governed by film diffusion, particle diffusion, or chemical exchange (chemisorptions). It is reported that the rate of ion exchange is controlled by chemical exchange if experimental data are fitted to pseudo-second-order equation [27].

From Table 1, one could see that the values of the initial sorption rate (h) and rate constant (k_2) were increased with the increase in temperature. The correlation coefficient R^2 has an extremely high value (>0.99), and its calculated equilibrium sorption capacity (q_e) is consistent with the experimental data. Therefore, the overall rate constant of both sorption process appear to be controlled by the chemical sorption process.

To estimate the activation energy of the adsorption (E_a) the Arrhenius equation was used:

$$\ln k_2 = \ln A - \frac{E_a}{RT} \qquad (6)$$

where k_2 and A (g/mmol min) are respectively the rate constant and temperature independent factor, E_a is the activation energy of the adsorption (J/mol), R is the

gas constant (8.314 J/molK), and T is absolute temperature (K). The plot of ln k_2 against $1/T$ is shown in Fig. 7.
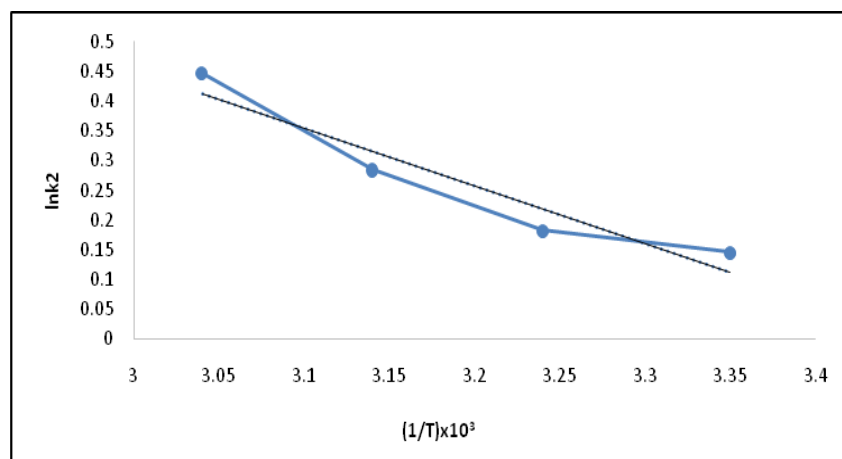
Fig. 7. Linear least square plots for obtaining E_a

Adsorption of Cs^+ was followed with low potential energy as show in Table 2 (E_a was less than 42.0 J/mol)[28].

3.4. Evaluation of thermodynamic parameters

The values of enthalpy change (ΔH^o) and entropy change (ΔS^o) were determined using linear plot of Van't Hoff equation:

$$\ln k_d = -(\Delta H^0 / RT) + (\Delta S^0 / R) \tag{7}$$

where k_d is the distribution coefficient, R is the gas constant, and T is the absolute temperature. A plot of ln k_d versus $1/T$ is shown in Fig. 8.
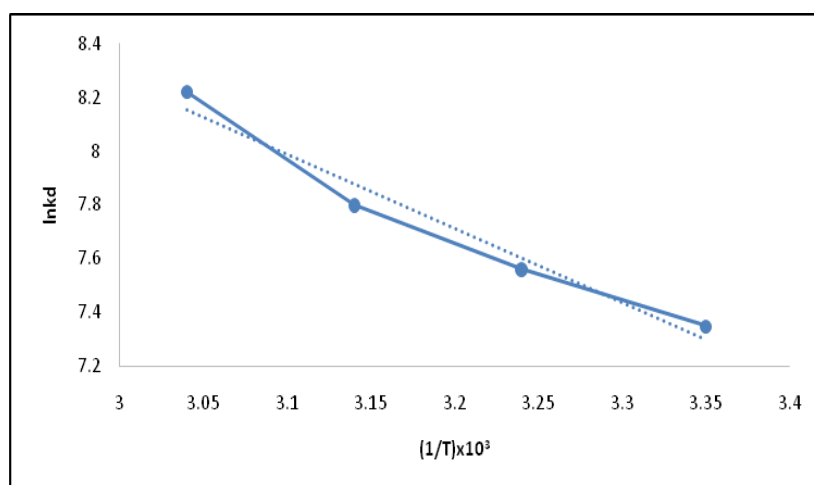The value of free energy change (ΔG^o) was calculated from:

$$\Delta G^o = \Delta H^o - T\Delta S^o \tag{8}$$

The calculated thermodynamic parameters are listed in Table 2.

Table 2.

Thermodynamic parameters of Cs^+ adsorption

| E_a (kJ/mol)	ΔH^o (kJ/mol)	ΔS^o (kJ/mol J)	ΔG^o (kJ/mol)			
			298 K	308 K	318 K	328 K
8.06	22.92	0.137	-17.91	-19.28	-20.65	-22.02

Fig. 8. Van't Hoff plot of Cs$^+$ adsorption

The positive values of ΔH^o revealed the endothermic nature of the adsorption process. The positive values of ΔS^o indicated that randomness of the system increased during the sorption process. The ΔH^o values were negative and decreased with increasing temperature, indicating adsorption of Cs$^+$ occurred spontaneously.

3.5. Sorption isotherms

The relationship between the amount of ions adsorbed by unit mass of the PNF – SG and the concentration of remaining ions in solution represented sorption isotherm [29] (Fig. 9).
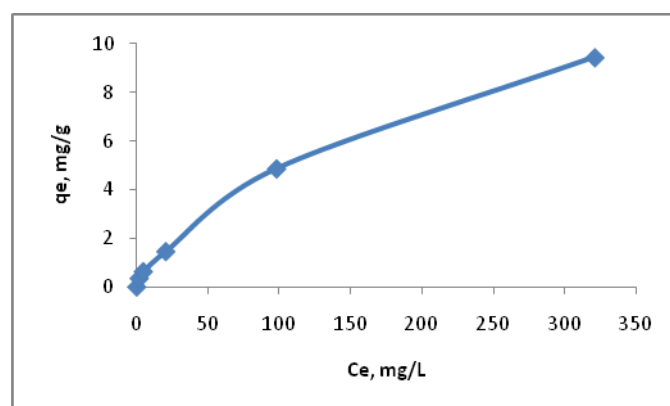
**Fig. 9.** Sorption isotherm of Cs$^+$at 298 K

The isotherm is regular, positive, and concave to the concentration axis.

Two isotherm models including Langmuir and Freundlich were used to describe the equilibrium experimental data.

The linearized form of the Langmuir equation is [28]:

$$\frac{C_e}{q_e} = \frac{1}{Q_o b} + \frac{C_e}{Q_o} \tag{9}$$

where Q_0 (mg/g), the saturation adsorption capacity and b the constant related to the free energy of adsorption were calculated from the slope and the intercept of plot of (C_e/q_e) against C_e (Fig. 10).
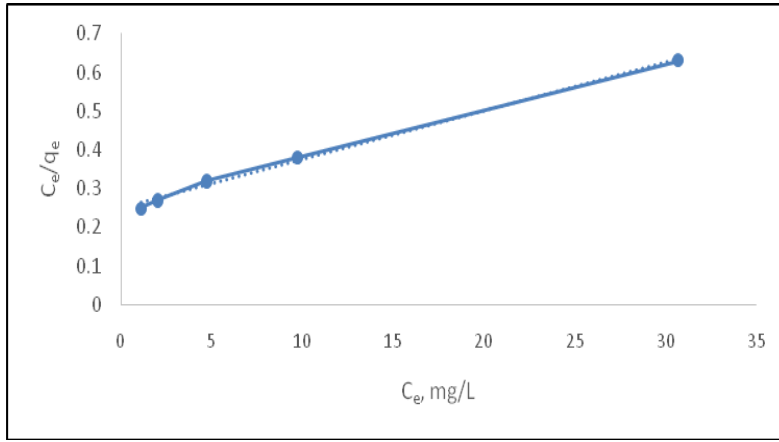
Fig. 10. Langmuir plots of Cs^+ adsorption

The most important parameter of Langmuir isotherm model, separation factor (R_L) can be defined as:

$$R_L = \frac{1}{1 + bC_0} \tag{10}$$

where C_0 (mg/L) is the highest initial ions concentration. The value of R_L indicated the type of Langmuir isotherm. The sorption process may be irreversible ($R_L = 0$), favourable ($0 < R_L < 1$), linear ($R_L = 1$), and unfavourable ($R_L > 1$) [31].
The calculated values of Q_0, b and R_L are listed in Table 3.

The linearized form of Freundlich model is written as follows [32]:

$$\log q_e = \log K_f + \frac{1}{n} \log C_e \tag{11}$$

where K_f is the Freundlich constant related to the adsorbent capacity and n is the constant indicative to the intensity of the adsorption process. The plot of $\log q_e$ versus $\log C_e$ is shown in Fig. 11. The values of the constant n and K_f were calculated from the slope and the intercepts of the plot and listed in Table 3.
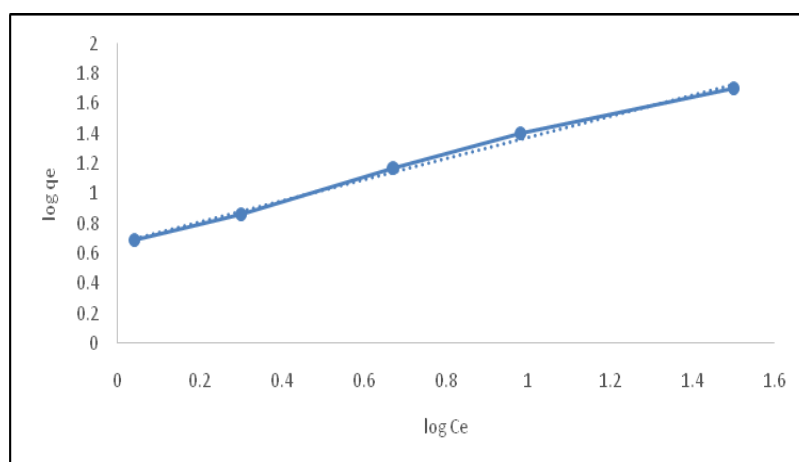
Fig. 11. Freundlich plots of Cs$^+$ adsorption
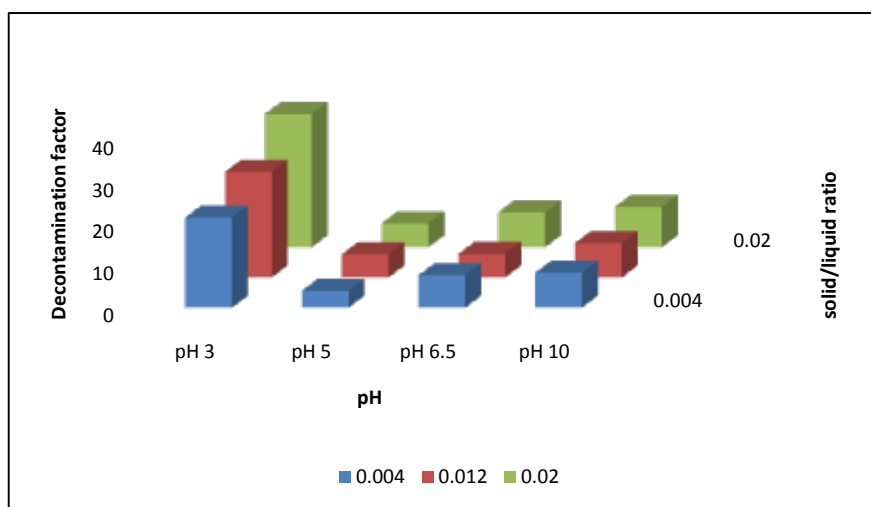
Table 3.

Adsorption isotherm parameters for Cs$^+$

Isotherm	Model parameter			
Langmuir	Q_0 (mg/g)	b (L/mg)	R_L	R^2
	80	0.05	0.019	0.9955
Freundlich	n	K_f (mg/g)	-	R^2
	1.4	4.7	-	0.9946

The adsorption data obey both Langmuir and Freundlich isotherms. The R_L values for Cs$^+$ is 0.019, indicating that the sorption process was favourable. The Freundlich intensity constant n is greater than unity indicating an increase tendency for sorption with the concentration increase.

Comparison with R^2 values determines which model best represents the adsorption behaviour of the adsorbent. In this case, Langmuir represents the best model, so the adsorption behaviour is homogeneous rather than heterogeneous.

3.6. Decontamination factor

Decontamination factor (DF) was calculated in terms of separation yield as the ratio of initial Cs$^+$ concentration to final concentration resulting from a separation process. In order to establish acceptable limits for variability in separation process performance, isolated and *synergic* effects of parameters were determined by calculating DFs (Figs. 12-14).

Laura Ruxandra Zicman, Elena Neacsu, Laurentiu Done, Liviu Tugulan, Felicia Dragolici,
Bogdan Tudor Obreja,Tanase Dobre

Fig. 12. Graph of calculated DF versus pH and solid/liquid ratio, contact time 2 h,
temperature=25 °C, initial Cs^+ concentration=1000 mg/L
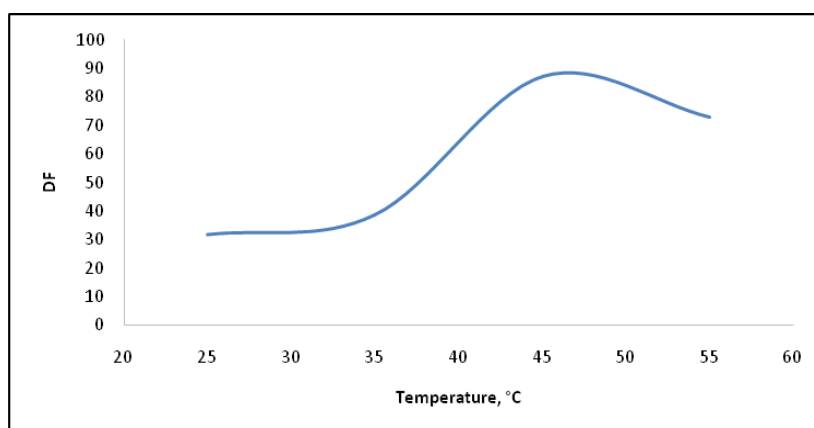
Fig. 13. Graph of calculated DF versus temperature, contact time 2 h, solid/liquid ratio=0.02,
pH=3, initial Cs^+ concentration=1000 mg/L

As it can be seen from these figures, DF is strongly affected by all process parameters. The parameter that has the most influence is temperature. By increasing the process temperature up to 50ºC, DFs could reach 100. Moreover, acidic medium promotes the achievement of values up to 40, and DFs increase with increasing initial Cs^+ concentration up to 800 mg/L. A further increase in initial Cs^+ concentration had a negligible effect on the DFs. That could be caused by the decrease of the ratio of number of vacant sites/number of Cs^+ ions on the sorbent surface. According to initial radioactive waste characteristics, the best combination of influencing parameter scan can be chosen and acceptable limits for variability in separation process can be established.
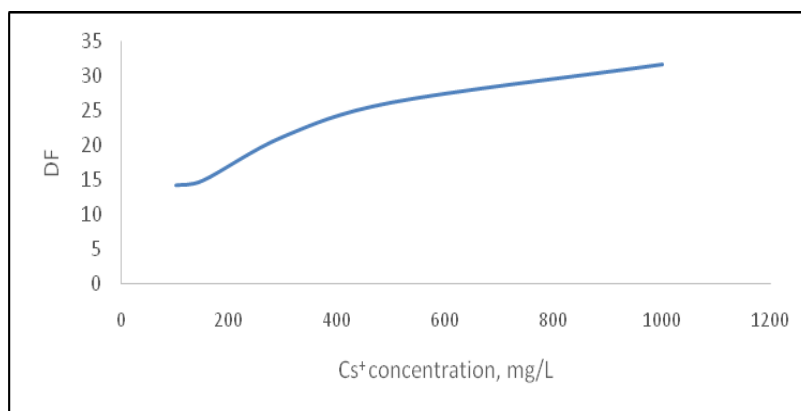
Fig. 14. Graph of calculated DF versus initial Cs^+ concentration, contact time of 2 h, solid/liquid ratio=0.02, pH=3, temperature=25 °C

4. Conclusion

Potassium nickel ferrocyanide, precipitated on silica gel beds, was tested as inorganic ion exchange material for the removal of cesium ions from aqueous solutions. The kinetic was experimentally studied and the obtained rate data were analyzed using simple kinetic models. Results reveal that the pseudo second-order sorption mechanism is predominant and the overall rate constant of sorption process appears to be controlled by chemical sorption process. Equilibrium isotherms have been determined and tested for different isotherm expressions and the sorption data were successfully modelled using Langmuir and Freundlich approaches. The values of thermodynamic parameters indicated endothermic and spontaneous nature of the adsorption process. Analysis of the kinetic data showed that the pseudo-second-order model fitted well with the experimental data confirming that the chemical sorption was the determining step.

Decontamination factors were calculated in order to identify all influencing parameters and acceptable limits for variability in the separation process.

REFERENCES

[1] Ritchie I.G., Growing dimensions. Spent fuel management at research reactors, *IAEA Bull.,* 40, (1998), 29–31.
[2] Coughtrey P. J., Thorne M. C., Radionuclide Distribution and Transport in Terrestrial and Aquatic Ecosystems, A. A. Balkema, Rotterdam, 1983.
[3] Shakir K., Sohsah M., Soliman M., Removal of cesium from aqueous solutions and radioactive waste simulants by coprecipitate flotation, *Sep. Purif. Technol.,* 54, (2007), 373–381.
[4] Bascetin E., Atun G., Adsorptive removal of strontium by binary mineral mixtures of montmorillonite and zeolite, *J. Chem. Eng. Data*, 55, (2010), 783–788.

[5] Balarama Krishna M.V., Rao S.V., Arunachalam J., Murali M.S., Kumar S., Manchanda V.K., Removal of ^{137}Cs and ^{90}Sr from actual low level radioactive waste solutions using moss as a phyto-sorbent, *Sep. Purif. Technol.,* 38**,** (2004),149–161.

[6] Cheng Z., Gao Z., Ma W., Sun Q., Wang B., Wang X., Preparation of magnetic Fe_3O_4 particles modified sawdust as adsorbent to remove strontium ions, *Chem. Eng., J.* 209**,** (2012), 451–457.

[7] Zhang C., Gu P., Zhao J., Zhang D., Deng Y., Research on the treatment of liquid waste containing cesium by an adsorption–microfiltration process with potassium zinc hexacyanoferrate, *J. Hazard. Mater.,* 167, (2009), 1057–1062.

[8] Lujaniene G., Meleshevych S., Kanibolotskyy V., Sapolait J., Strelko V., Remeikis V., Oleksienko O., Ribokaite K., Sciglo T., Application of inorganic sorbents for removal of Cs, Sr, Pu and Am from contaminated solutions, *J. Radioanal. Nucl. Chem.,* 282, (2009), 787–791.

[9] Duff M.C., Hunter D.B., Hobbs D.T., Fink S.D., Dai Z., Bradley J.P., Mechanisms of strontium and uranium removal from high-level radioactive waste simulant solutions by the sorbent monosodium titanate, *Environ. Sci. Technol.,* 38, (2004), 5201–5207.

[10] Walker G.M., Hanna J.-A., Allen S.J., Treatment of hazardous shipyard wastewater using dolomitic sorbents, *Water Res.,*39, (2005), 2422–2428.

[11] Puziy A.M., Cesium and strontium exchange by the framework potassium titanium silicate $K_3Ti_4O_4(SiO_4)3\cdot4H_2O$, *J. Radioanal. Nucl. Chem.,* 237, (1998), 73–80.

[12] Shabana E.I., El-Dessouky M.I., Sorption of cesium and strontium ions on hydrous titanium dioxide from chloride medium, *J. Radioanal. Nucl. Chem.,* 253, (2002), 281–284.

[13] Todd T.A., Brewer K.N., Wood D.J., Tullock P.A., Mann N.R., Olson L.G., Evaluation and testing of inorganic ion exchange sorbents for the removal of cesium-137 from Idaho chemical processing plant acidic tank waste, *Sep. Sci. Technol.,* 36, (2001), 999–1016.

[14] El-Kamash A.M., Evaluation of zeolite A for the sorptive removal of Cs^+ and Sr^{2+} ions from aqueous solutions using batch and fixed bed column operations, *J. Hazard. Mater.,* 151, (2008), 432–445.

[15] Ghaemi A., Torab-Mostaedi M., Ghannadi-Maragheh M., Characterizations of strontium(II) and barium(II) adsorption from aqueous solutions using dolomite powder, *J. Hazard. Mater.,* 190, (2011), 916–921.

[16] Hass P. A., A Review of Information on Ferrocyanide Solids for Removal of Cesium from Solutions, *Separ. Sci. Technol.,* 28(17-18), (1993), 2479-2506.

[17] Lin Y., Fryxell G. E., Wu H., Engelhard M., Selective sorption of cesium using self-assembled monolayers on mesoporous supports, *Environ. Sci. Technol.,* 35(19), (2001), 3962-3968.

[18] Won H.-J., Moon J.-K., Y.Chung C.-H., Evaluation of ferrocyanide anion exchange resins regarding the uptake of Cs^+ ions and their regeneration, *Nuclear Engineering and Technology*, 40(6), (2008), 489-496.

[19] Watari K., Imai K., Ohmomo Y., Muramatsu Y., Nishimura Y., Izawa M., Baciles L. R., Simultaneous adsorption of Cs-137 and I-131 from water and milk on metal ferrocyanide-anion exchange resin, *J. Nucl. Sci. Techn.,* 25(5), (1988), 495–499.

[20] Folsom T. R., Hansen N., Tatum T. J., Hodge V. F., Recent developments in method for concentrating and analyzing radiocesium in sea water, *J. Radiation. Res.,* 16**,** (1975), 19–27.

[21] Mann D. R., Casso S. A., In situ chemisorption of radiocesium from sea water, *Marine Chem.,* 14(4), (1984), 307-328.

[22] Orechovská J., Rajec P., Sorption of cesium on composite sorbents based on nickel ferrocyanide*, J. Radioanal. Nucl. Chem.,* 242(2), (1999), 387-390.

[23] "NIST *Nuclide Half-Life Measurements*". NIST. Retrieved 13 March, 2011.

[24] Abd El-Latif M.M., Elkady M.F., Kinetics study and thermodynamic behaviour for removing cesium, cobalt and nickel ions from aqueous solution using nano-zirconium vanadate ion exchange, *Desalination*, 271, (2011), 41–54.

[25] Milyutin V.V., Mikheev S.V., Gelis V.M., Kononenko O.A.*, Coprecipitation of microamounts of cesium with precipitates of transition metal ferrocyanides in alkaline solutions, Radiokhimiya*, 51(3), (2009), 258–260.

[26] Lagergren S., About the theory of so-called adsorption of soluble substances, *K. Sven. Vetenskapsakad. Handl.* 24, (1898), 1–39.

[27] Ho Y.S., McKay G., Pseudo second-order model for sorption processes, *Process. Biochem.* 34, (1999), 451–465.

[28] Scheckel K. G., Sparks D. L., Temperature effects on nickel sorption kinetics at mineral water interface, *Soil. Sci. Soc. Am. J.*, 65**,** (2001), 719–728.

[29] Peric J., Trgo M., Medvidovic N.V., Removal of zinc, copper and lead by natural zeolite-a comparison of adsorption isotherms, Water Res., 38, (2004), 1839–1899.

[30] Langmuir I., The adsorption of gases on plane surfaces of glass, mica and platinum, *J. Am. Chem. Soc.*, 40**,** (1918), 1361–1403.

[31] Mohan D., Chander S., Single, binary and multicomponent sorption of iron and manganese on lignite, *J. Colloid Interface Sci.*, 299, (2006), 57–76.

[32] Freundlich H., Adsorption in solution, *Phys. Chem.*, **57,** (1906), 384–401.